Observation of domains in antiferromagnetic fluorides by x-ray topography

Isfahani, Mehdi Safa

OBSERVATION OF DOMAINS IN ANTIFERROMAGNETIC FLUORIDES BY X-RAY TOPOGRAPHY

by

Mehdi Safa (Isfahani), M.Sc.

A thesis submitted to the University of Durham for the Degree of Doctor of Philosophy

April 1977

Department of Physics
Science Laboratories
Durham University
Durham City

PREFACE

This thesis contains an account of work which was performed while I was a research student in the Department of Physics at the University of Durham during the period February, 1974 - March, 1977. Some of the work was performed at the Science Research Council's Daresbury Laboratory. The work reported here is my own original research and has not been submitted to any other University. Where the thesis reviews the work of others or work performed in collaboration, due acknowledgement is made in the text.

I have been assisted by several people, and I am particularly grateful to -

Dr. B. K. Tanner, who, as my supervisor, lent unstinting support, guidance, encouragement and assistance throughout my research.

Dr. W. D. Corner, the leader of the Solid State Group at Durham and my supervisor, whose advice was often instructive and useful.

Professor A. W. Wolfendale, Head of the Department of Physics at the University of Durham, for making available the facilities of the department.

Mrs. B. M. Wanklyn and Dr. B. J. Garrard, from the Clarendon Laboratory, Oxford, who provided very high quality crystal specimens.

Mr. D. Midgley, my fellow research student, who often assisted me during experimental runs.

Mr. K. G. Moulson, Research Technician, for his excellent technical assistance.

Mr. J. Scott, for the construction of glass cryostats.

Mr. W. Leslie (Chief Technician) and his staff in the workshop.

Dr. H. Klapper, of the Rhein-Westphalia Technische Hochschule, Aachen, who computed the dislocation directions in $KNiF_3$ and $KCoF_3$.

Dr. D. Reed, of Leeds University, for susceptibility measurements on single crystals of $KNiF_3$.

The author would like to thank the Reza Pahlavi Cultural Foundation (Iran) for the award of a Research Scholarship and the Science Research Council for use of the Synchrotron Radiation Facility on NINA at Daresbury Laboratory.

I would like to thank Mrs. M. Wilson for typing the thesis. My friends Mr. G. Clark and Mr. F. Warnock patiently proof-read the thesis, and I am grateful for their assistance.

Parts of this thesis have been or will shortly be published,

From Chapter 3 - B. K. Tanner, D. Midgley, and M. Safa (1977) J.Appl.Cryst. (In Press).

From Chapter 4 - M. Safa, B. K. Tanner, B. M. Wanklyn, and B. J. Garrard, (1977) J. Crystal Growth, (In Press).

M. Safa, B. K. Tanner, H. Klapper, and B. M. Wanklyn (1977) Phil.Mag. (In Press).

From Chapter 5 - B. K. Tanner, M. Safa, D. Midgley, J. Bordas, (1976) J.Magnetism and Magnetic Materials, 1, 337.

B. K. Tanner, M. Safa, and D. Midgley (1977) J.Appl.Cryst. (In Press).

From Chapter 6 - M. Safa, D. Midgley, and B. K. Tanner, (1975) Phys.Stat.Sol.(a), 28, K89.

From Chapter 8 - M. Safa and B. K. Tanner, Proc. Internat.Conf.Magnetism, (Amsterdam 1976), Physica (1977) 86-88B, 1347.

CONTENTS

ABSTRACT

CHAPTER ONE

Page No.

ANTIFERROMAGNETISM

1.1 Introduction 1

1.2 Exchange Interaction 1

1.3 Theory of Susceptibility 3

1.3.1 $\underline{\Delta}$ parallel to $\underline{H}$ 5

1.3.2 $\underline{\Delta}$ perpendicular to $\underline{H}$ 6

1.4 Anisotropy of Susceptibility 8

1.5 Spin flop 10

1.6 The Crystallographic and Magnetic Structure of $KNiF_3$ and $KCoF_3$ 12

1.7 Torque Magnetometry 18

1.8 Domain Walls 19

1.9 Experimental Techniques for Antiferromagnetic Domain Observation 20

1.10 Review of the Antiferromagnetic Domain Wall Studies 21

1.11 Spin Configuration in Antiferromagnetic Domain Wall 24

1.12 Domain Walls in Perovskite KMF_3 (M=Co,Ni) 25

1.13 Domain Wall Motion in Cubic Antiferromagnetic Crystals 26

CHAPTER TWO

X-RAY DIFFRACTION TOPOGRAPHY

2.1 Introduction 28

2.2 Orientation Contrast 29

2.3 Extinction Contrast 30

2.4 The Schulz Method 30

		Page No.
2.5	Berg-Barrett Topography	31
2.6	Lang's Method	32
	2.6.1 Section Topographs	32
	2.6.2 Projection Topographs	33
2.7	Topographic Resolution	34
2.8	The Double-Crystal Topography	36
2.9	X-Ray Diffraction Theories	37
	2.9.1 The Kinematical Theory	37
	2.9.2 The Dynamical Theory	38
2.10	Contrast of Dislocations	42
	2.10.1 Direct Image	42
	2.10.2 Dynamical Images	44
	2.10.3 Intermediary Image	45
2.11	Domain Wall Observations	45

CHAPTER THREE

X-RAY SYNCHROTRON TOPOGRAPHY

3.1	Synchrotron Radiation	49
3.2	Synchrotron Topography	49
3.3	Intensity and Image Formation	50
3.4	Resolution	51
3.5	Experimental Arrangement	53
3.6	Contrast in Synchrotron Topographs	55

CHAPTER FOUR

PERFECTION STUDIES OF KMF_3 (M=Ni,Co,Fe) CRYSTALS GROWN FROM THE FLUX

4.1	Crystal Growth	59
4.2	Preparation of Specimens for X-ray Topography	60

		Page No.
4.3	Choice of the Geometry of the Diffracting Planes	62
4.4	X-Ray Topographic Observations of $KNiF_3$	62
4.5	X-Ray Topographic Observations of $KCoF_3$	67
4.6	X-Ray Topographic Observations of $KFeF_3$	69
4.7	The Direction of Dislocations in Flux-Grown Crystals	70

CHAPTER FIVE

CRYOGENIC X-RAY TOPOGRAPHY

5.1	Review of the Low Temperature X-ray Topographic Experiments	75
5.2	Glass Cryostat with Cold Finger Tail	76
5.3	Stainless Steel Cryostat with a Gas-Cooled Tail	79
5.4	Glass Cryostat with no X-ray Window	81
5.5	Polystyrene Immersion Cryostat	83

CHAPTER SIX

STATIC DOMAIN STUDIES IN $KNiF_3$ and $KCoF_3$ BY X-RAY TOPOGRAPHY

6.1	Predicted Domain Studies	86
6.2	Observation of Domain Walls in $KNiF_3$	86
6.3	Observation of Domain Walls in $KCoF_3$	90

CHAPTER SEVEN

MAGNETOCRYSTALLINE ANISOTROPY AND THE THEORY OF DOMAIN WALL MOVEMENTS IN CUBIC ANTIFERROMAGNETS

7.1	The Origin of the 4θ-Term in the Torque Curves of $KNiF_3$ Crystal	94
	7.1.1 Intrinsic Effect	94
	7.1.2 Movement of Domain Walls	97
7.2	Further remarks on Domain Wall Movements	100

CHAPTER EIGHT — Page No.

EXPERIMENTAL OBSERVATIONS OF DOMAIN WALL MOVEMENTS

8.1 The Apparatus 104

8.2 Domain Wall Movement in $KNiF_3$ 104

8.3 Domain Wall Movements in $KCoF_3$ 107

8.4 The Reversibility of the Domain Wall Movements in $KCoF_3$ 108

8.5 Susceptibility Measurements on Single Crystal of $KNiF_3$ 109

8.6 Effective Anisotropy of $KNiF_3$ and $KCoF_3$ crystals 112

8.7 Discussion ------ 116

SUGGESTIONS FOR FURTHER EXPERIMENTS 119

APPENDIX

REFERENCES

ABSTRACT

A brief introduction to the theory of susceptibility in antiferromagnets is given and the experimental studies on antiferromagnetic domains are reviewed.

X-ray topographic techniques are discussed. Low temperature domain studies in moderate fields have not been performed previously by X-ray topography due to the geometrical constraints. A new topographic technique using synchrotron radiation has been developed for domain wall motion studies in magnetic fields up to 14 KOe at temperatures down to 4.2K. Details of four successful cryostat designs are presented.

The perfection of crystals $KNiF_3$, $KCoF_3$ and $KFeF_3$ grown from the flux has been studied by X-ray topography. Very low dislocation densities and dynamical diffraction effects were observed. Dislocations directions in the flux grown crystals of $KNiF_3$ and $KCoF_3$ prefer to run in such directions as to minimise their elastic energy per unit growth length in a similar manner to dislocations in crystals grown from aqueous solution.

The topographic experiments on highly perfect crystals of $KNiF_3$ and $KCoF_3$ have revealed three types of domains with spin orientations parallel to each of the cube edges. Controlled domain wall motion in $KNiF_3$ and $KCoF_3$ has been studied using synchrotron radiation. Wall movement occurs to align spins perpendicular to the applied field and walls between domains already so oriented are

found not to move. The general behaviour of antiferromagnetic domains in $KNiF_3$ and $KCoF_3$ is in excellent agreement with the theoretical model proposed by Néel (1954). No catastrophic spin flop is observed, and some wall movements are reversible. Both direct observations of domain wall motion and the susceptibility measurements on single crystals of $KNiF_3$ show that the spin flop occurs via domain wall motion. The effective anisotropy is measured from the critical and threshold field data for both $KCoF_3$ and $KNiF_3$.

CHAPTER ONE

ANTIFERROMAGNETISM

1.1 Introduction

The concept of antiferromagnetism was first put forward by Néel (1932) in connection with his study of paramagnetic susceptibility of metals and alloys of transition elements. He found that metals such as Pt, Pd, Mn, Cr or alloys such as Pd-rich Pd-Ni show an almost temperature independent susceptibility which is too large to be explicable in terms of Pauli's free electron paramagnetism. Néel suggested that the atoms of these sublattices possess magnetic moments and a negative exchange coupling is operating among them. As a consequence, he originally envisaged an antiferromagnetic substance composed of two sublattices of paramagnetic ions, A and B which at low temperatures are magnetized in opposite directions by negative exchange interactions.

1.2 Exchange interaction

Dirac (1929) showed that the exchange interactions of the Heisenberg type are equivalent to an interatomic potential

$$V_{ij} = -\frac{1}{2}J(1+4\ \underline{S}_i \cdot \underline{S}_j) \qquad 1\text{-}1$$

where $\underline{S}_i$ and $\underline{S}_j$ are, respectively, the spin angular momentum vector of atoms i and j in units of $\hbar$ and J is the exchange integral. In the ferromagnetism J is positive and denotes the coefficient of direct exchange coupling between neighbouring atoms whose electron clouds overlap with each other to some extent, if the Heisenberg theory of ferromagnetism is assumed to be applicable. In the antiferromagnetic case Kramers (1934) first pointed out that it is possible to have an exchange spin-coupling through the agency of intermediate non-magnetic atoms.

Anderson (1950) developed the theory of superexchange for a crystal of $Mn^{++}O^{--}$ and showed that superexchange is the strongest between those atoms which are on opposite sides of the negative ion, since then one of the 2p- orbitals (2p in the case of O^{--}) contributes to it. His conclusion is interesting in view of the quoted experimental results of Shull et al (1951) on MnO, in which he finds a strong coupling of next nearest neighbouring Mn ions rather than of nearest neighbours. This indicates that the superexchange directly through O^{--} ion may be more powerful than that between locations making angles of 90^{o} with O^{--} ions.

It is assumed that J is the same for all the Z interacting neighbours, and one can replace the sum over them, $\sum_j \underline{S}_j$ by $Z\langle \underline{S}_j \rangle$, where $\langle \underline{S}_j \rangle$ means the statistical average of $\underline{S}_j$ over the sublattice to which j belongs. Then the potential energy of the atom i, apart from an additive constant will be given as follows:

$$V_i = \sum_j v_{ij} = 2\,JZ\,\langle \underline{S}_j \rangle\,\underline{S}_i \qquad 1\text{-}2$$

Assuming that the Lande g-factor is isotropic, that is, does not depend on the direction of spins with respect to the crystal orientation. The magnetic moment $\underline{\mu}$ of an individual atom is then $\underline{\mu} = -g\mu_B \underline{S}$, where μ_B is the Bohr magneton, and

$$V_i = -2JZg^{-2}\mu_B^{-2}\langle \underline{\mu}_j \rangle \mu_i = -\underline{H}_{ej}\,\mu_i \qquad 1\text{-}3$$

where

$$\underline{H}_{ej} = 2JZg^{-2}\mu_B^{-2}\langle \underline{\mu}_j \rangle \qquad (J<0) \qquad 1\text{-}4$$

Here $\underline{H}_{ej}$ is the exchange "magnetic field" acting on atom i with spins up which results from the sublattice j, with spins down, and also from other spins of the positive lattice, therefore, one may put,

$$\underline{H}_e^{+} = -\alpha \langle \underline{\mu}^{-} \rangle - \gamma \langle \underline{\mu}^{+} \rangle \qquad 1\text{-}5$$

and similarly,

$$\underline{H}_e^- = -\alpha\langle\underline{\mu}^+\rangle - \gamma\langle\underline{\mu}^-\rangle \qquad 1\text{-}6$$

where α and γ are constant. If N is the number of magnetic atoms per unit volume, and positive and negative lattices are called A and B, respectively, the magnetizations of the two sublattices are $\underline{M}_A = \frac{1}{2}N\langle\underline{\mu}^+\rangle$ and $\underline{M}_B = \frac{1}{2}N\langle\underline{\mu}^-\rangle$, so that equations 1-5 and 1-6 can be written as

$$\underline{H}_{eA} = -N_{AB}\underline{M}_B - N_{AA}\underline{M}_A \qquad 1\text{-}7$$

$$\underline{H}_{eB} = -N_{BA}\underline{M}_A - N_{BB}\underline{M}_B \qquad 1\text{-}8$$

Here $N_{AA} = \frac{2\alpha}{N}$, and $N_{BA} = \frac{2\gamma}{N}$, N_{AB} is a molecular field constant for the nearest neighbour interaction and since the same type of atoms occupy the A and B lattice sites $N_{AA} = N_{BB} = N_{ii}$ and $N_{AB} = N_{BA}$.

1.3 Theory of Susceptibility

The theory of susceptibility of antiferromagnetic materials based on the Weiss molecular field approximation was founded by Néel (1932,1936), Bitter (1937) and Van Vleck (1941). A brief introduction of this theory will be presented here.

On a molecular field approximation, each sublattice may be considered to be interacting with two molecular magnetic fields, $\underline{H}_e$ and $\underline{H}_a$, where the exchange magnetic field $\underline{H}_e$ is usually much greater than the magnetic anisotropy field $\underline{H}_a$. Therefore if we neglect the anisotropy field, the molecular magnetic field $\underline{H}_m$ will equal to $\underline{H}_e$ for each sublattice, and equations 1-7 and 1-8 can be written as

$$\underline{H}_{mA} = -N_{AB}\underline{M}_B - N_{AA}\underline{M}_A \qquad 1\text{-}9$$

$$\underline{H}_{mB} = -N_{BA}\underline{M}_A - N_{BB}\underline{M}_B \qquad 1\text{-}10$$

In the case where there is no external field, $\underline{M}_A$ and $\underline{M}_B$

are antiparallel to each other, so long as N_{AB} is positive and N_{ii} is not too large. The common direction of $\underline{M}_A$ and $\underline{M}_B$ can be denoted by $\underline{\Delta}$. If an external field $\underline{H}$ is applied, $\underline{M}_A$ and $\underline{M}_B$ will be tilted to each other and the direction of $\underline{\Delta}$ can be defined as $\frac{\underline{M}_A}{M_A} - \frac{\underline{M}_B}{M_B}$. This direction coincides with that of $\underline{M}_A - \underline{M}_B$ so long as the angle between $\underline{M}_A$ and $-\underline{M}_B$ is small or the lengths of these two vectors are about the same.

In general, the applied field may make an arbitrary angle with the easy axis. First, however, we can calculate the susceptibility of a single crystal when the magnetic field is applied parallel to the easy axis. Suppose the applied field $\underline{H}$ is parallel to $\underline{H}_A$ and antiparallel to $\underline{H}_B$. In this case, the magnitudes of the fields acting on the plus and minus spins are $|\underline{H} + \underline{H}_{mA}|$ and $|\underline{H} + \underline{H}_{mB}|$, respectively. The magnitudes of $\underline{M}_A$ and $\underline{M}_B$ are given by the standard theory of the molecular field approximation, and are

$$M_A = \frac{1}{2} Ng\mu_B S B_s \ (x_A) \qquad 1\text{-}11$$

$$M_B = \frac{1}{2} Ng\mu_B S B_s \ (x_B) \qquad 1\text{-}12$$

with

$$\begin{cases} x_A = |\underline{H} + \underline{H}_{mA}| \ Sg\mu_B/kT \\ x_B = |\underline{H} + \underline{H}_{mB}| \ Sg\mu_B/kT \ . \end{cases} \qquad 1\text{-}13$$

Here k is Boltzmann constant, and

$$B_s(x) = \frac{2S+1}{2S} \coth \frac{2S+1}{2S} x - \frac{1}{2S} \coth \frac{x}{2S} \qquad 1\text{-}14$$

is the Brillouin function, which reduces to tanh x for $S = \frac{1}{2}$ and to the Langevin function Coth x - $\frac{1}{x}$ for $S = \infty$. When there is no external field, if we substitute $\underline{H}_{mA}$ and $\underline{H}_{mB}$ from 1-9 and 1-10 into 1-11 and 1-12, the same magnitude of the saturation magnetization M_o for the two sublattices will be obtained,

$$M_o = \frac{1}{2}Ng\mu_B B_s(x_o) \text{ with } x_o = (N_{AB}-N_{ii})M_o Sg\mu_B/kT. \quad 1\text{-}15$$

M_o is a decreasing function of temperature as in the case of ferromagnetism and vanishes at the critical point, or the Néel point. The critical temperature can be found by approaching from the high temperature side $T > T_N$. In this case it is assumed x_o to be small and $SB_s(x_o)$ is replaced by $\frac{1}{3}(S+1)x_o$ and have from 1-15

$$M_o = \frac{C}{2T}(N_{AB}M_o - N_{ii}M_o) \quad 1\text{-}16$$

from which, at once it follows,

$$T_N = \frac{1}{2} C (N_{AB} - N_{ii}) \quad 1\text{-}17$$

where $C = Ng^2 \cdot \mu_B^2 \cdot S(S+1)/3k$. 1-18

Hence the Néel temperature is higher the stronger AB interaction and the weaker the AA or BB interactions.

At the temperatures above T_N, it is assumed that x_A and x_B are small. Therefore equation 1-11 will be of the form

$$M_A = \frac{C}{2T}(H - N_{AB} M_B - N_{ii} M_A), \text{ etc,} \quad 1\text{-}19$$

since $\underline{M}_A$ and $\underline{M}_B$ are both parallel to $\underline{H}$ in the paramagnetic region. Solving this equation, with $M_A = M_B$, and putting $M_A + M_B = XH$, the following equation is obtained

$$\chi = \frac{C}{T+\theta} \text{ with } \theta = \frac{1}{2}C (N_{AB} + N_{ii}) \quad 1\text{-}20$$

1.3.1 $\underline{\Delta}$ parallel to $\underline{H}$

The susceptibility below the Néel point can be calculated by expanding $SB_s(x_A)$ in powers of H and retaining the first order term. It is essential here to assume that the molecular fields of $\underline{H}_{mA}$ and $\underline{H}_{mB}$ are respectively parallel and antiparallel to the applied field $\underline{H}$ in order to obtain a consistent solution (Fig.1(a)); otherwise, except in the case where they are equal

in magnetization and make the same angle with $\underline{H}$, equations 1-11 and 1-12 can not be solved. Therefore for $M_A - M_o = M_o - M_B$ we have

$$\chi_{\parallel} = \frac{M_A - M_B}{H} = \frac{3SB'_S(x_o)}{(S+1)} \; C \Big/ \left[T + \frac{1}{2}(N_{AB}+N_{ii})\, C\frac{3SB'_S(x_o)}{S+1}\right] \qquad 1\text{-}21$$

where $B'_S(x_o)$ is the derivative of the Brillouin function with respect to its argument. At absolute zero, equation 1-21 predicts $\chi_{\parallel}=0$. The physical reason is that in the approximation of the molecular field theory all the atomic moments are either parallel or antiparallel to the applied field at $T = 0^{\circ}K$. As the temperature T increases, $\chi_{\parallel}$ also increases until at the Néel temperature, $\chi_{\parallel}(T_N)$ becomes equal to the susceptibility $\chi(T)$ given by equation 1-20. For $T > T_N$, 1-21 can be reduced to equation 1-20.

1.3.2 $\underline{\Delta}$ perpendicular to $\underline{H}$

In this case the magnetic field is applied perpendicular to the easy axis. The applied magnetic field produces a torque which tends to rotate the sublattice magnetizations $\underline{M}_A$ and $\underline{M}_B$ through a small angle ϕ, and incline them symmetrically to $\underline{H}$. Fig.(1.1(a) and (b)) show the magnetic moment arrangement for an antiferromagnet when the field is parallel and perpendicular to sublattice magnetization respectively. The rotation is opposed by the molecular field. At equilibrium the total torque on each sublattice magnetization must equal zero, that is, for M_A, the total torque is:

$$\underline{M}_A \wedge (\underline{H} + \underline{H}_{mA}) = 0 \qquad 1\text{-}22$$

By substituting $\underline{H}_{mA}$ from equation 1-9 into 1-22 we will have,

$$\underline{M}_A \wedge \underline{H} - N_{AB}\, \underline{M}_A \wedge \underline{M}_B = 0$$

or $$M_A H \cos\phi - N_{AB} M_A M_B \sin 2\phi = 0$$

therefore: $$2 M_B \sin\phi = \frac{H}{N_{AB}} \qquad 1\text{-}23$$

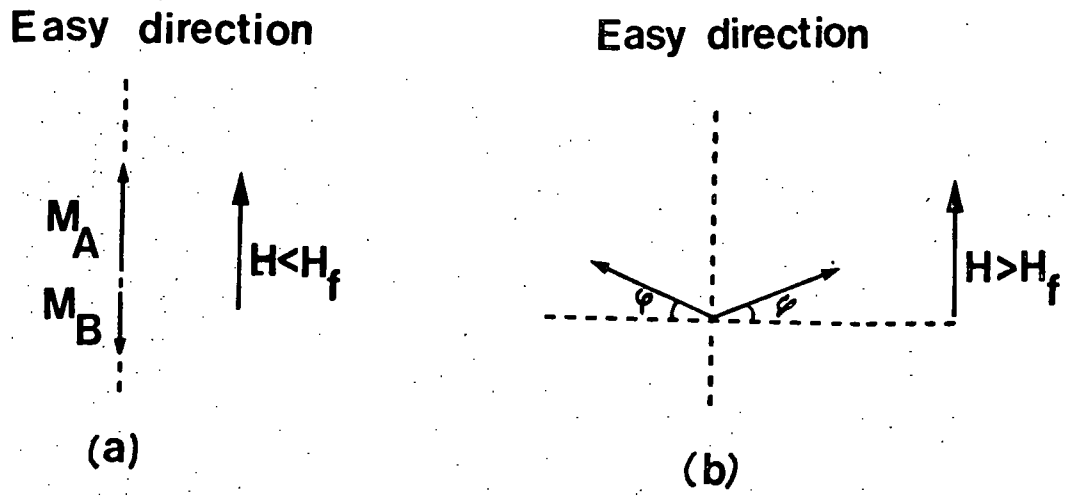

Fig.(1-1) The magnetic moment arrangement for an antiferromagnet when the field is parallel (a), and perpendicular (b) to sublattice magnetization.

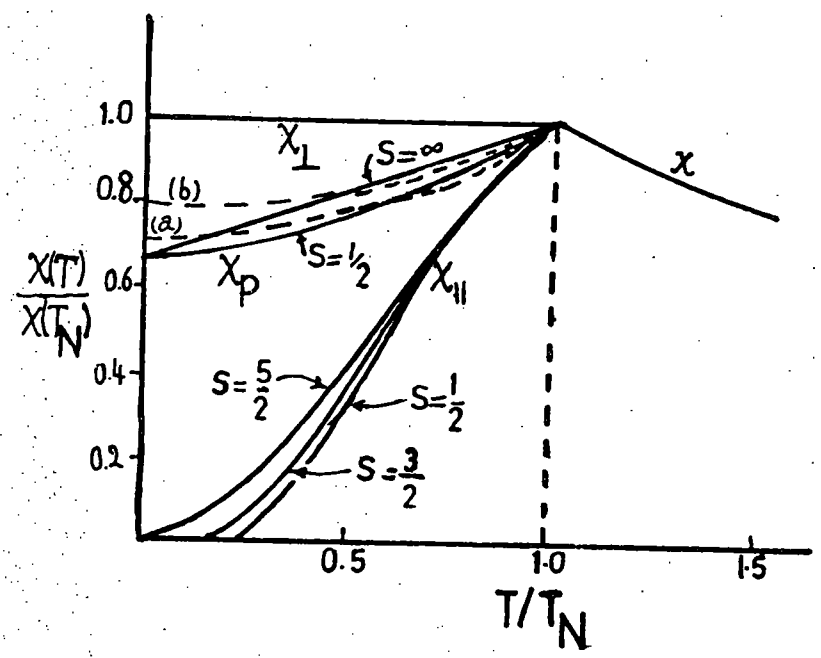

Fig.(1-2) The susceptibility of an antiferromagnetic material as a function of temperature in reduced units. $N_{ii}=0$. The solid curves are computed from the theoretical formulae (20), (21), (25), while the dashed lines give the experimental results of Bizzet et al.(1938) on MnO. (After Van Vleck 1941)

Since $M_A = M_B$, the net magnetization M along the field direction is just

$$M = (M_A + M_B)\text{Sin } \phi = 2\ M_B \text{ Sin } \phi \qquad 1\text{-}24$$

Therefore using 1-23 and 1-24, the susceptibility $\chi_\perp$ is given by

$$\chi_\perp = \frac{M}{H} = \frac{1}{N_{AB}} \qquad 1\text{-}25$$

This shows that $\chi_\perp$ is a constant and independent of N_{ii}, that is, AA or BB interactions. It should be noted that the paramagnetic susceptibility $\chi = \frac{C}{T+\theta}$ for $T \gg T_N$, also reduces to $\chi = \frac{1}{N_{AB}}$ at $T = T_N$. The susceptibilities predicted by the equations 1-20, 1-21, 1-25 are shown graphically in Fig.1-2. The general features of these susceptibilities agree well with experiments. However, many antiferromagnetic materials are studied experimentally as powders, and, Van Vleck (1941) introduced the idea of random orientation of the internal field. He showed that one can decompose the external field acting on each individual crystallite into components parallel and perpendicular to the corresponding preferred axis of magnetization. Averaging over all directions of spontaneous magnetization we find that the powder susceptibility is

$$\chi_p = \frac{2}{3}\chi_\perp + \frac{1}{3}\chi_{||} \qquad 1\text{-}26$$

Therefore the ratio $\chi_p(T=0)/\chi_p(T=T_N)$ is $\frac{2}{3}$, because $\chi_{||}$ vanishes at $T = 0$, $\chi_\perp$ is constant and $\chi_{||} = \chi_\perp$ at $T = T_N$. Experimental values for this ratio are in the neighbourhood of 2/3, but always greater. Bizzett, Squire and Tsai (1938) found that the ratio for MnO is 0.69 which is very near to the theoretical prediction. Experimental results of Bizzett et al. for MnO are shown with dashed lines in Fig(1-2).

Nagamiya et al. (1955) point out that this slight difference

of the experimental results from the theory may be attributed to the following points:

1. Incorrectness of the Weiss molecular field approximation for χ at $T = T_N$.
2. Existence of more than two sublattices.
3. Effect of anisotropy energy and also anisotropy of the g-factor.

1.4 Anisotropy of Susceptibility

As it was mentioned above Van Vleck (1941) assumed that there are parallel and perpendicular domains with a ratio 1/2 and gave the susceptibility formula $\chi = (\chi_{\parallel} + 2\chi_{\perp})/3$. As Nagamia (1951) points out, this assumption can not be justified, since the difference in the free energy per unit volume of the two types of domains, $\frac{1}{2}(\chi_{\perp} - \chi_{\parallel})H^2$ is positive so that only perpendicular domains must be realized under thermal equilibrium. This means that the perpendicular susceptibility is constant below the Néel temperature, contrary to observation. Nagamiya mentioned that in ferromagnets, the energy to the external field $-\underline{M} \cdot \underline{H}$ can be greater than the anisotropy energy, and the magnetization $\underline{M}$ can easily be turned to the direction of the external field. In antiferromagnets, however, the energy due to the external field $-\frac{1}{2}\chi H^2$ is so small that each spontaneous magnetization of the two sublattices can hardly deviate from the easy direction for an ordinary applied field.

Nagamiya (1951) gave a theory of the susceptibility of antiferromagnets based on a consideration which takes the anisotropy energy K into account. As the perpendicular susceptibility is greater than the susceptibility parallel to the field, therefore the minimum energy configuration is with the antiferromagnetic axis perpendicular to the applied field.

Consequently in a simple Heisenberg model we expect the moments to rotate until the perpendicular spin orientation is obtained. Nagamiya showed that such rotations are opposed by an anisotropy energy which keeps the moments aligned along a particular crystal axis. A formula for the dependence of the susceptibility upon external magnetic field was first published by Nagamiya(1951) and Yosida (1951) independently, and it shows that the field dependence part varies proportional to the square of the intensity of the magnetic field, and inversely proportional to the anisotropy constant.

$$\chi_p = \frac{1}{3}\chi_{||} + \frac{2}{3}\chi_{\perp} + \frac{2}{15K}(\chi_{\perp} - \chi_{||})^2 H^2 \qquad 1\text{-}27$$

The dependence of the susceptibility on the strength of the field has been investigated for a number of antiferromagnets, and from this, one can estimate the value of anisotropy energy K. For example, using the measurement of Bizzett et al. (1938), the anisotropy energy of MnO can be estimated to be $K = 5.7 \times 10^4$ ergs/Cm^3.

Néel (1953), interpreted the field-dependence of the susceptibility for cubic crystals as a domain effect. Although at that time nothing was known about the domain structure in antiferromagnets, he supposed a domain wall between two antiferromagnetic domains with different spin directions in a cubic crystal. By applying a magnetic field, since $\chi_{\perp} > \chi_{||}$, one of the domains whose spin axis is more perpendicular to the field will expand by pushing the wall to the side of the other domain. Néel proposed an elastic force of the type of $-Cx$, (C is a constant) which pulls back the wall to its original position. This mechanism also gives rise to a field dependence of the susceptibility proportional to $(\chi_{\perp} - \chi_{||})^2 H^2$ similar to 1-27.

1.5 Spin flop

If, on application of magnetic field H, the sublattice magnetizations remain collinear with the easy direction, the change in free energy per unit volume is $\Delta F_T = -\chi_{||}(H^2/2)$. Suppose, however, the sublattice magnetizations [actually, $(\underline{M}_A - \underline{M}_B)/M_0$] be perpendicular to the easy direction. If the anisotropy $K \approx 0$ this change in free energy is $\Delta F_T = -\chi_{\perp}(H^2/2)$. For an antiferromagnetic material $\chi_{\perp} > \chi_{||}$ at $T < T_N$. Therefore, under these conditions, the perpendicular orientation would be the ground state. For $K \neq 0$, $\Delta F = K - \chi_{\perp}(H^2/2)$ for the perpendicular orientation; the parallel orientation is the state of lowest energy provided H is not too large. At a certain critical field H_f, defined by the equation

$$-\frac{1}{2}\chi_{||} H_f^2 = K - \frac{1}{2}\chi_{\perp} H_f^2 \qquad 1\text{-}28$$

or $$H_f = \left[\frac{2K}{\chi_{\perp} - \chi_{||}}\right]^{\frac{1}{2}}$$

spin flop occurs.

When $\underline{H}$ is applied to the preferred direction of a uniaxial antiparallel spin system, a sudden change in the magnetization parallel to $\underline{H}$ is observed when H equals the critical field H_f. According to Foner and Hou (1962), the change in magnetization, ΔM, at $H = H_f$ is given by

$$\Delta M = \left[2K(1-\alpha)/H_f\right]^{\frac{1}{2}} \qquad 1\text{-}29$$

Here α is the ratio of the parallel susceptibility to the perpendicular one. The antiparallel magnetization (A.F. State) of the two sublattices turn from the direction of the easy axis to that perpendicular, and incline towards the field direction, and therefore a net magnetization $\underline{M} = \underline{M}_A + \underline{M}_B$ (S. F. State) appears. At temperatures well below the Néel point, the critical

field is approximately given by $H_f = (2H_e H_a)^{1/2}$, Jacobs (1961). The value of exchange field is estimated as the ratio of sublattice magnetization to perpendicular susceptibility, and the anisotropy field H_a is the ratio of anisotropy energy per unit volume to sublattice magnetization. Spin flopping can be seen easily if the Néel temperature is low. Here the exchange field H_e is low and hence according to the formula $H_f = (2H_e \cdot H_a)^{1/2}$, H_f is relatively small. The phenomenon was first observed in $CuCl_2 \cdot 2H_2O$ (T_N = 4.3 K) by Paulis et al, (1951). Spin flop has been studied in a considerable number of antiferromagnets. For example, King and Paquette (1973) observed an intermediate state between the antiferromagnetic and spin-flop states of MnF_2. This state consists of alternate thin-slab domains of antiferromagnetic and spin-flop state of MnF_2. They used NMR, Faraday rotation, optical-absorption spectroscopy in their experiments, and the intermediate field was between 92.5 to 93 KOe. Kohler et al, (1959), and Wilkinson et al. (1959), using neutron diffraction observed this phenomenon in iron group halide compounds with low anisotropy where decoupling is equivalent to domain rotation. Wilkinson and his Co-workers examined indirectly the behaviour of antiferromagnetic domains in these compounds and determined the specific orientation of the magnetic moments within the layers in iron group halides. For example, their single crystal measurements on $CoCl_2$ in zero magnetic field had suggested the existence of three types of antiferromagnetic domains in this compound. When the field was applied along the scattering vector of the 101 reflection, the intensity variation seemed to involve two processes. First, there was a domain transformation until only the two domains having antiferromagnetic axes most closely perpendicular to the direction of the field were present. However,

as the external field is exceeded, the moments flip from the preferred crystallographic direction to one perpendicular to the field. This process is completed by a field of 2KOe

Before studying the possibility of spin flop or domain wall motion in cubic antiferromagnets, we will review the structure and magnetic properties of cubic perovskite $KNiF_3$ and $KCoF_3$. Domain wall observations in these materials will be presented in this thesis.

1.6 The Crystallographic and Magnetic Structure of $KNiF_3$ and $KCoF_3$

X-ray diffraction studies of Okazaki & Suemune (1961) on single crystals KMF_3 (M = Co, Fe, Mn, Ni) revealed that at room temperature the structures of all these crystals are of the perovskite type and no distortion from cubic symmetry was observed. In the room temperature unit cell Fig.(1-3) each divalent metal M^{2+} is surrounded octahedrally by six F^- ions at face-centres, while at each cube corner there is a K^+ ion. Each F^- ion is collinear with its two nearest neighbour M^{2+} ions and powder susceptibility measurements of Hirakawa et al. (1960) showed that all KMF_3 crystals become antiferromagnetic below Néel temperatures (T_N) shown in Table 1-1.

TABLE 1-1

Temperatures of the susceptibility maxima of KMF_3 crystals

Crystals	$KMnF_3$	$KFeF_3$	$KCoF_3$	$KNiF_3$
T_N(K)	88	113	114	275

Okazaki et al. observed that below these temperatures, $KNiF_3$ retains its lattice symmetry, but $KMnF_3$ and $KFeF_3$ and $KCoF_3$ become monoclinic, rhombohedral($\alpha < 90^\circ$) and tetragonal ($a > c$) respectively. Fig.(1-4) shows the powder susceptibility of

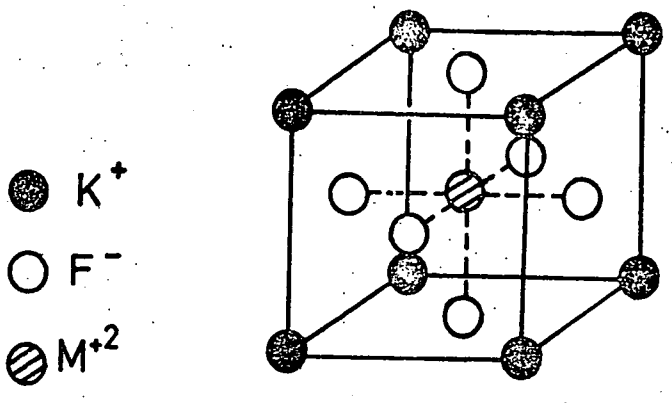

Fig.(1-3) The crystal structure of KMF_3.

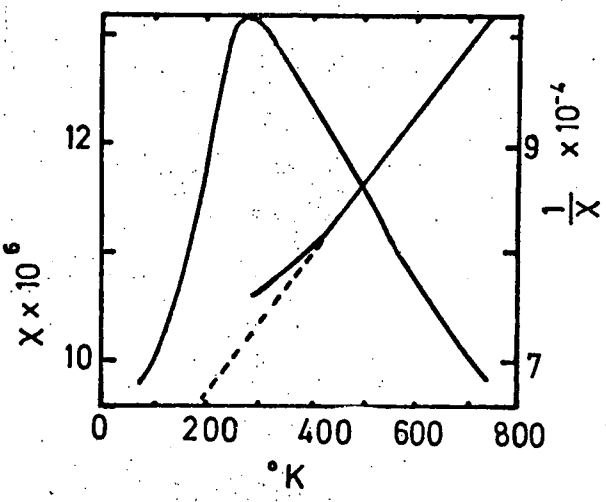

Fig.(1-4)

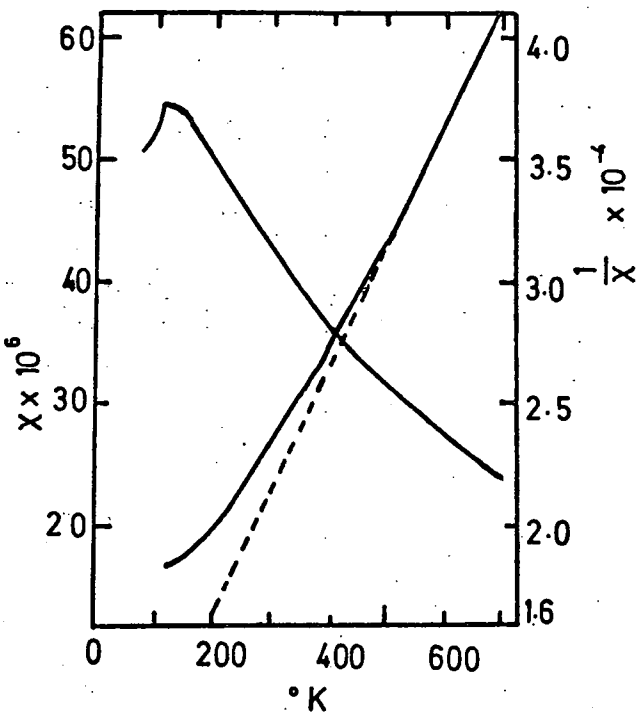

Fig.(1-5)

Fig.(1-4) Gram susceptibility versus temperature for $KNiF_3$.

Fig.(1-5) Gram susceptibility as a function of temperature. for $KCoF_3$ (After Hirakawa et al. 1960)

$KNiF_3$ with respect to temperature, measured by Hirakawa et al. For $KNiF_3$ a fairly broad maximum was found at 275 K, below which χ decreases in the usual manner and the ratio of $\chi_{T=0}/\chi_{max}$ is 0.68 which is very nearly the 2/3 predicted by Van Vleck's molecular field theory. Hirakawa et al.(1960) found a sharp anomaly in their specific heat data for $KNiF_3$ at 253 K. Sykes and Fisher (1962) and Fisher (1962) show that the susceptibility maximum occurs at a temperature somewhat higher than that for which a long-range order sets in and that the Néel temperature is more accurately given by specific heat or neutron diffraction measurements. Nouet et al. (1972) using ultrasonic resonance, stress-induced linear dichroism, and heat capacity measurements determined an accurate Néel temperature for $KNiF_3$ crystals grown from the melt or in a flux. All three techniques give a value of 246 ± 1 K for T_N. Nouet et al. (1972) mentioned that, when $KNiF_3$ powder obtained from an aqueous solution was used, the value of T_N is very different, which is the case for Hirakawa's specific heat measurements giving T_N=253 K. Therefore the discrepancy may be due to the nature of the sample used.

For $KCoF_3$ as Fig.(1-5) shows, below 114 K, χ decreases monotonically with temperature, thus 114 K is thought to be the Néel temperature. Hirakawa et al. (1960), using X-ray and calorimetric measurements confirmed T_N=114 K for $KCoF_3$. Julliard and Nouet (1975) found that the $KCoF_3$ unit cell undergoes a tetragonal distortion at 117 K. In Fig.(1-5), a considerable deviation of χ from the Curie-Weiss law is seen. Hirakawa et al. explain that this is because the lowest orbital triplet of Co^{+2} in the cubic field splits into three levels with $J = \frac{1}{2}$, 3/2 and 5/2 by the L-S coup-

ling. As these level separations are of the order of kT, corresponding to the temperatures of measurements, one may expect such deviation of χ from Curie-Weiss law. Okazaki and Suemune (1961) determined the lattice constant of the $KNiF_3$ cubic cell at 298 K to be 4.014 $\pm$ 0.001Å and at 78 K, 4.001 $\pm$ 0.002Å. Scatturin et al.(1961) found that the lattice constant at 4.2 K reduces to 3.993Å . Sintani et al.(1968) also give the variation of lattice constant for $KNiF_3$. Their results are generally lower than those of Okazaki et al.(1961). However, no distortion from a cubic perovskite structure was observed. Again Okazaki and Kawaminani (1973) using white X-rays and a double-crystal diffractometry technique could not detect any distortion from the cubic structure of $KNiF_3$ in the antiferromagnetic region. The variation of lattice constant of $KNiF_3$ with temperature is shown in Fig.(1-6).

Okazaki and Suemune (1961) determined the lattice constant of $KCoF_3$ at 298K to be $a = 4.069 \pm 0.001$Å. They showed that the structure of $KCoF_3$ distorts from cubic to tetragonal symmetry on cooling through T_N = 114 K. At 78 K they obtained $a = 4.057 \pm 0.002$ Å and $c = 4.049 \pm 0.002$Å, or $\frac{c-a}{a} = -2 \times 10^{-3}$. Julliard and Nouet (1975), using a liquid helium cryostat which was adapted for an X-ray goniometer, were able to measure the lattice constants of $KCoF_3$ from 4 to 300 K. They observed that below 117°K, the crystal undergoes a tetragonal distortion, and studied the temperature dependence of $\frac{c-a}{a}$. For example at 78 K $\frac{c-a}{a} \simeq -2.5 \times 10^{-3}$, and at 4.2 K, $\frac{c-a}{a} \simeq -3.5 \times 10^{-3}$, and they confirm that the distortion is of magnetostrictive character. Fig.(1-7a)

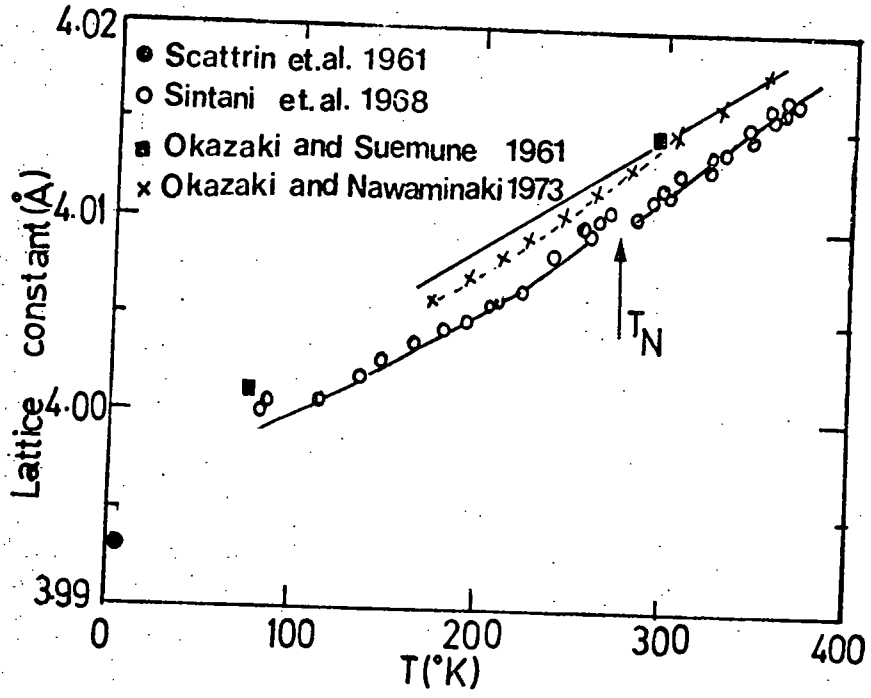

Fig.1-6) Temperature dependence of the lattice constant of $KNiF_3$

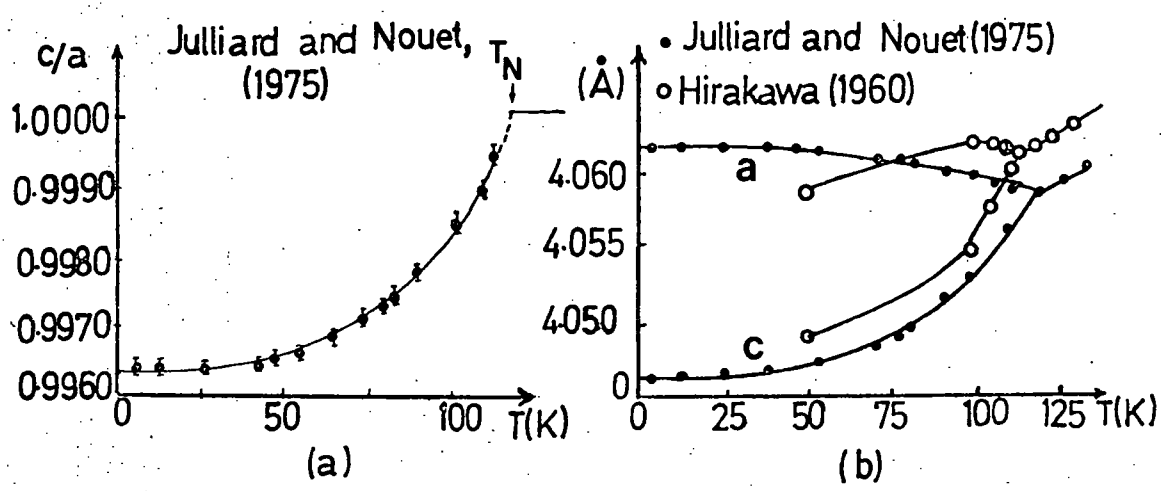

Fig.(1-7) (a) Temperature dependence of c/a for $KCoF_3$.

(b) Temperature dependence of dimensions of $KCoF_3$ unit cell.

shows the variation of lattice constants of $KCoF_3$ with temperature. Fig.(1-7b) shows the variation of c/a with temperature for $KCoF_3$. Scatturin et al.(1961), reviewed the properties of 3d divalent ions and the crystal structures of perovskite-like compounds. The 3d level of a free transition divalent ion is split by electric field due to negative charges or dipoles surrounding the cation in a crystal or complex. In a field of octahedral symmetry the splitting gives rise to two groups of levels: a lower triplet (t_{2g}) and an upper doublet (e_g). Table (1-2) shows the electron distribution for 3d divalent Co and Ni ions in $KCoF_3$ and $KNiF_3$.

TABLE 1-2

Electron distribution for Co and Ni ions in $KCoF_3$ and $KNiF_3$

ion	No. of 3d electrons	Configuration t_{2g}	Configuration e_g	No. of unpaired electrons t_{2g}	No. of unpaired electrons e_g	Total unpaired electrons	S
Co	7	↑↓ ↑↓ ↑	↑ ↑	1	2	3	3/2
Ni	8	↑↓ ↑↓ ↑↓	↑ ↑	0	2	2	1

The arrangement of moments in KMF_3 crystals is the expected one on the basis of an indirect exchange mechanism. The interactions are supposed to take place via the non-magnetic F^- anions, and the electronic configuration of the cations as well as the crystal structure, determines the particular type of ordering.

Scatturin et al.(1961) determined the magnetic structure of $KNiF_3$ and $KCoF_3$ by neutron diffraction techniques. At 4.2K magnetic superlattice lines were observed which indicate an antiferromagnetic spin arrangement for which all

(six) nearest neighbours of any spin are aligned in antiparallel fashion, that is, G-type structure. Fig.(1-8) shows the G-type magnetic structure, in which parallel and anti-parallel orientations of moments are shown by positive and negative spheres.

De Jongh and Block (1975), review the available experimental data on the exchange constants, $J/_k$, of the series of insulating antiferromagnetic compounds XMF_3 (X=K, Rb,Tl; M = Co, Ni, Mn) and show that:

(a) in all XMF_3 compounds the exchange path connecting equivalent nearest neighbours consist of single, collinear (180^o) M-F-M bonds;

(b) possible contributions of next-nearest magnetic neighbours to the total measured interaction are known to be about 1% of the nearest neighbour exchange only;

(c) dipolar contributions to the total interaction for KMF_3 compounds with cubic symmetry is effectively zero, where they cancel because of the cubic symmetry.

Lines (1967) has given an extensive discussion of $KNiF_3$. In the case of $KNiF_3$ there is no contribution from magnetic dipole-dipole interactions, as a consequence of the cubic symmetry of the magnetic lattice. He assumes that any anisotropy of the system must be extremely small and did not take the anisotropy into account, i.e. a model Heisenberg system. Lines has been able to obtain a fairly accurate estimate of exchange by analysing the measured powder susceptibility of Hirakawa (1960) in terms of the high temperature series expansions. From the fit of the paramagnetic susceptibility to this expansion he obtained $J/_k = 43 \pm 2$ K. The series

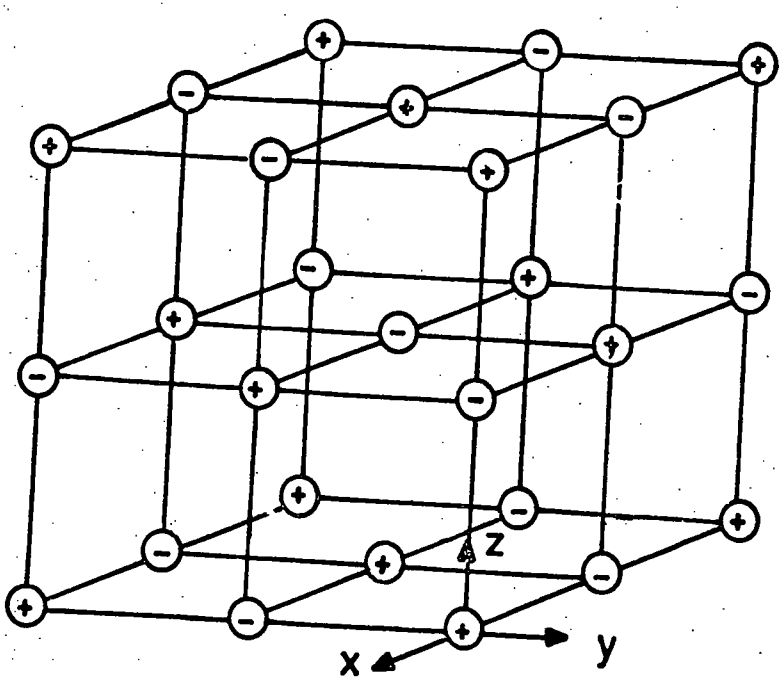

Fig.(1-8) The magnetic unit cell of $KNiF_3$ and $KCoF_3$. Parallel and antiparallel orientation of the moments are shown by positive and negative spheres. (After Scatturin et al. 1961)

expansion also indicated the position of the maximum in the susceptibility. Relating this to the experimentally observed $T(\chi_{max}) = 275K$, Lines finds $J/_k \simeq 45K$. Furthermore, using the expression of Rushbrook and Wood (1958, and 1963) for a three dimensional Heisenberg antiferromagnet

$$\frac{kT_N}{J} \cong \frac{5}{96} (Z-1)\left[11\ S\ (S+1) - 1\right] \qquad 1\text{-}29$$

where for $KNiF_3$, $S = 1$, $Z = 6$, $T_N = 246$ K, one can obtain $J/_k = 45$ K. Although Chinn et al.(1971) obtained $J/_k = -50.8$ K from the analysis of their two-magnon Raman scattering experiments, de Jongh and Block (1975) adhere to the value $J/_k = -44$ K, since also in the case of K_2NiF_4 the $J/_k$ determined by Chinn et al.(1971) was more than 10% higher than the other results.

In the case of $KCoF_3$ the orbital angular momentum of the Co^{2+} ion is not quenched by the octahedrally co-ordinated crystal field (Buyers et al.1971). This may give rise to the possibility of anisotropic magnetic interactions between the ions. However, the neutron diffraction experiments of Holden et al.(1971) show there is no evidence for the directional anisotropy which has been suggested for exchange interactions in $KCoF_3$.

In (Breed et al.(1969)) estimates of $J/_k$ were obtained from the experimental T_N values, with the aid of the prediction of Rushbrook and Wood (1958, 1963) for the $\frac{kT_N}{J}$ value of the simple cubic Heisenberg antiferromagnet with $S = \frac{1}{2}$. Breed et al. give the value $J/_k = 19.1$ K for $KCoF_3$ which agrees well with that of Buyers et al.(1971), $J/_k = 19.3$ K.

1.7 Torque magnetometry

The magnetic anisotropy of antiferromagnetic crystals can in principle be measured by using torque magnetometry. Nagamiya et al.(1960) did the pioneer work on a theoretical interpretation of the results of such a technique. The results of the torque measurements on MnO crystal at liquid air temperature not only contains a 2θ term, but a 4θ term as well. They interpreted their results in two alternative ways: either the torque component of period 90^{o} is due to the anisotropy energy within the plane of easy magnetization or it is due to the movements of walls which separate domains with different directions of sublattice magnetization. Their interpretation in terms of domain movement is based on Néel's (1953) ideas and they favour a domain wall movement mechanism.

Hirakawa et al.(1961) investigated the magnetic anisotropy of single crystals of $KCoF_3$ and $KNiF_3$ using a torque magnetometer in the temperature range of 78-300 K. They found that in the antiferromagnetic region, if the crystals were suspended along one of the cube edges, their torque curves can be expressed by the formula

$$T = C_1 H^2 \mathrm{Sin}\ (2\theta + \varepsilon_1) - C_2 H^4\ \mathrm{Sin}\ (4\theta + \varepsilon_2) \qquad 1\text{-}30$$

where θ is the angle of rotation of the field H relative to one of the cubic axis, and C's are constants.

In the case of $KCoF_3$, no 4θ term was observed and within the experimental error $\varepsilon_1 = 0$. For $KNiF_3$ at 78 K the torque curve contains both components. The phase constant ε's were found to be zero, and from this fact, it is concluded that the antiferromagnetic axis in both $KCoF_3$ and $KNiF_3$ is parallel to one of the cubic axes.

In $KNiF_3$, when no external stress is applied, the amplitude of the 2θ term is quite small compared with that of the 4θ term, but as the stress is increased, it grows and the 4θ term disappears. This suggests that the specimen becomes nearly a single domain crystal by applying the stress, in agreement with the results of Ferré et al.(1976), who measured the stress induced linear dichroism. Hirakawa and his coworkers also show that the origin of the 4θ term in $KNiF_3$ may be explained by the same mechanism proposed by Nagamiya for MnO. Their calculations based on domain wall movement are consistent with their torque curve results.

For $KCoF_3$, in which no 4θ term was found in the torque magnetometry investigation, by applying an external stress along one of the cubic axes the amplitude of the 2θ term increased rapidly. As Hirakawa et al.(1961) pointed out, it is because of the large distortion which $KCoF_3$ undergoes in the antiferromagnetic region, that, if an unidirectional stress is applied along one of the edges of the twinned crystal, it may become a single domain with its c-axis being parallel to the direction of the stress. In Chapter Six of this thesis, it will be demonstrated how the domain pattern in $KCoF_3$ is influenced by stress, and depending on the amount of stress which the cement introduces to crystal in low temperatures, one may get a single or multi-domain crystal.

1.8 Domain Walls

An antiferromagnetic domain wall is a transition layer which separates adjacent domains with different antiferromagnetic ordering in the crystal. Usually when the crystal is cooled through the Néel temperature T_N, the antiferromagnetic ordering nucleating in various regions of the crystal

will vary in direction. For example NiO is cubic, whereas below T_N the crystal becomes slightly distorted from this cubic structure to a rhombohedral one, and the amount of distortion increases as the temperature decreases. In NiO the magnetic moments are arranged in ferromagnetic sheets that lie in $\{111\}$ planes. On cooling below the Néel temperature a contraction occurs along the $\langle 111 \rangle$ directions. There are, however, four equivalent $\langle 111 \rangle$ -directions. The result is that different regions of the crystal have different contraction axes and the crystal becomes twinned. These twinning planes form antiferromagnetic domain walls which can be studied by usual crystallographic methods.

It should be pointed out that antiferromagnetic domains are not to be expected for the same reason as in ferromagnetic materials, that is, to reduce the magnetostatic energy. The presence of domains would, however, increase the entropy because of additional disorder, and hence lower the free energy, Morrish (1965). It seems this change in entropy is very small, and there should be some other reason for the existence of domain walls.

1.9 Experimental Techniques for Antiferromagnetic Domain Observation.

Most of the techniques for revealing ferromagnetic domains require a non-zero magnetization. In antiferromagnetic crystals there is no net magnetization, but as was mentioned above, the crystal undergoes a magnetostrictive distortion below T_N, which is useful for domain wall observation either by optical birefringence microscopy or X-ray topography. In the optical case, the twin walls are visible because each domain is an optically uniaxial crystal

with the optic axis coincident with the contraction axis. Twin walls in NiO were easily seen with transmitted polarized light in thin sections of crystal which were 100μm or less thick (Roth 1960).

X-ray Lang topography is a powerful technique with good resolving power which has been frequently used for domain studies, Polcarova & Lang (1962), Polcarova (1967 and 1969). By applying this technique one can study domains in the interior of bulk specimens which are opaque to visible or infra red light. The contrast of domains is only due to the difference in deformation on opposite sides of the wall which is produced by the magnetostriction. X-ray synchrotron topography and its application to observe and control the movement of domain walls in the presence of magnetic fields at low temperatures has been developed by the Durham group, (Tanner et al. 1976, 1977 a,b). A brief review of dynamical X-ray diffraction theory, techniques of X-ray topography and the contrast of the defects and domain walls in X-ray topographs will be given in Chapters Two and Three.

1.10 Review of the Antiferromagnetic Domain Wall Studies

Antiferromagnetic domains were first observed in NiO crystals by Slack (1960) and Roth (1960) indirectly with neutron diffraction and directly with polarized light. NiO is paramagnetic at temperatures above T_N=523^{o}K and its structure is cubic. Below T_N, the antiferromagnetic ordering results in a slight rhombohedral deformation of the crystal, which consists of a contraction of the original cubic unit cell along one of the $\langle 111 \rangle$ axes. This con-

traction is of the order of 10^{-3}. Because this contraction may occur along any of the four equivalent directions in the parent cubic crystal, crystallographic twinning (which is related to the antiferromagnetic ordering) may take place and four types of twin walls may exist.

The transition layer separating twinned domains is called a T wall. Another type of domain wall which arises from a rotation of moments within the ferromagnetic sheets of an antiferromagnet is called an S wall. S walls have also been observed in NiO by Roth (1960). Roth studied the movement of T walls in NiO by applying a magnetic field. He observed that when a magnetic field of 20-30 KOe was applied to well annealed crystals, the T walls were displaced or rotated to new positions. Roth mentioned that the response to H is highly erratic because T walls are easily pinned by imperfections in the crystal. Both T and S walls were observed in NiO, using double crystal X-ray topography, Yamada et al. (1966). They observed S-domains and deduced the magnitude of the magnetostriction. They found that:

1. The direction of easy magnetization is very close to one of the $\circlearrowleft[11\bar{2}]$
2. There exist two types of magnetic walls for S-domains, S walls parallel to $\circlearrowleft(1\bar{1}0)$ and S-walls parallel to $\circlearrowleft(\overline{2+\epsilon}\,11)$,
   (The expressions $\circlearrowleft[uvw]$ and $\circlearrowleft(uvw)$ are used to mean a group of three axes or planes obtained by permuting u, v and w respectively).

3. The spontaneous magnetostriction expressed as an orthorhombic deformation and a monoclinic deformation, is estimated as $|e_{x'x'} - e_{y'y'}| = (9 \pm 3) \times 10^{-5}$ and $|e_{z'x'}| = (1.6 \pm 1.0) \times 10^{-5}$. Here x', y', z' are axes of an orthogonal co-ordinate system taken along $[11\bar{2}]$, $[\bar{1}10]$ and $[111]$, respectively. Using similar X-ray topography techniques, Nakahigashi et al.(1975) studied antiferromagnetic domain walls in well annealed NiO crystals and determined the strain components of spontaneous magnetostriction in NiO. Their values are $e_{x'x'} - e_{y'y'} = -5.4 \times 10^{-4}$ and $e_{z'x'} = 0.9 \times 10^{-4}$. As seen these values are a few times larger than those found previously by Yamada et al.(1966).

Saito et al.(1966) observed two types of domains in CoO at 140 K by Berg-Barrett topography. CoO is an antiferromagnet with $T_N = 293$ K. Above T_N the crystal structure is of the Na Cl type, whereas below T_N, the lattic undergoes a tetragonal deformation along one of the cubic axis which increases gradually with decreasing temperature and is of the order of 10^{-2} at 77 K. Saito et al. also found a new rhombohedral deformation in CoO below T_N. They could observe two types of domains at 140 K by X-ray Berg-Barrett topography. Domains of one type are characterized by the direction of the tetragonal axis which were called T domains. Domains of the other type are subdomains present in each T-domain. They are formed as a result of the change in the direction of the trigonal axis of the antiferromagnetic

spin arrangement and, therefore, they are distinguished by the direction of the rhombohedral axis. This type of domains were called r domains and their walls r-walls, Saito et al.(1966).

Antiferromagnetic domains in Cr have been observed by X-ray double-crystal topography in the low temperature phase or lower than the spin flop temperature, 122 K where the crystal is in a state of longitudinal polarization (AF_2). The domain boundary due to slight tetragonality of the crystal lattice was observed by Hosoya and Ando (1971). Ando and Hosoya (1972) have used neutron topography to observe spin-density-wave domains in antiferromagnetic Cr and came to the conclusion that there was a discrepancy of several orders of magnitude between the observed and calculated domain sizes.

1.11 Spin Configuration in Antiferromagnetic Domain Wall

The transition in spin ordering occurs gradually over a number of atomic planes and gives rise to a meta-stable spin configuration in the crystal. Nagamiya (1958) suggested that the spins would be spatially varying in a gradual way so as to minimize the total energy which is the sum of the super-exchange energy among $\langle 100 \rangle$ neighbours, the exchange energy among $\langle 110 \rangle$ neighbours, the magnetic anisotropy energy, and the elastic energy. He also showed that the boundary region between both T and S domains in NiO is a kind of Bloch wall.

The Bloch wall in a ferromagnetic crystal is a transition layer which separates adjacent regions (domains) magnetized in different directions. The entire change in spin direction between domains does not occur in one discontinuous jump across

a single atomic plane (Fig.1-9). The total exchange energy is minimized when the change is distributed over many spins, but the anisotropy energy is minimized when the change is over few spins. The energy per unit area of wall is the sum of contributions from exchange and anisotropy energies: $\sigma_w = \sigma_{ex} + \sigma_{anis.}$ · Minimizing this energy one obtains the relations giving the magnitude of the wall thickness, and the total wall energy per unit area of wall. In iron $\sigma_w \approx 1$ erg/cm^2, and the thickness of the transition region is about 300 lattice constants.

The spin configuration in antiferromagnetic domain walls of Nio-type crystals has been studied theoretically by Yamada (1963, and 1966). He formulated Nagamiya's ideas and obtained solutions for three cases: 90°, 60° and 180° walls for NiO. A model of the spin configuration inside the wall which is similar to a Bloch wall (Fig.1-10) is given. The wall width and the stored energy in the wall are estimated to be about 80 Å and 4 erg/cm^2 for the {001} walls in NiO and 9Å and 20 erg/cm^2 for the {001} walls in MnO. This model shows that the antiferromagnetic domain walls in NiO and MnO are very much narrower than the ferromagnetic ones, but as it is the only work on domain wall spin configuration in NiO type crystals, the need for more theoretical work especially on the simple cubic systems like KMF_3 is strongly felt.

1.12 Domain Walls in Perovskite KMF_3 (M = Co, Ni)

Schlenker et al. (1974) observed antiferromagnetic domains in $KCoF_3$ by X-ray topography at 78 K. Although their crystal does not seem to be of good quality they observed a domain pattern mostly of (011) and (01$\bar{1}$) walls separating T domains with mean sublattice magnetization directions along $\pm$ [010] and $\pm$ [001].

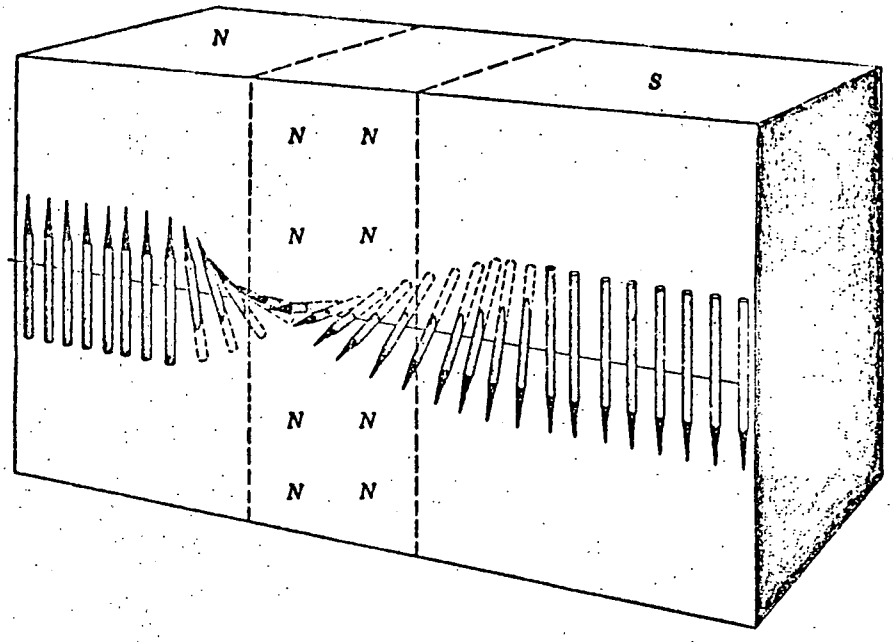

Fig.(1-9) The structure of the Bloch wall separating domains. In iron the thickness of the transition region is about 300 lattice constants. (After Kittel 1971).

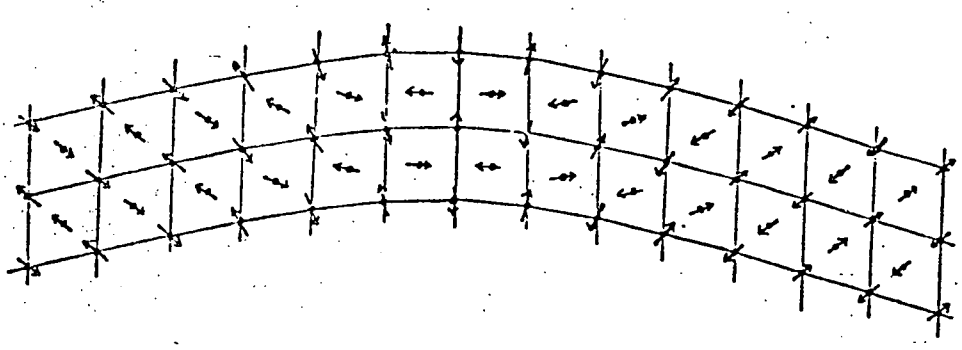

Fig.(1-10) Variations of spins S_i, and strain in the (100) plane in the case of an antiferromagnetic 90^{o} domain wall. This figure is somewhat exaggerated. (After Yamada 1963).

They also observed a substructure within the T-domains, which they believed to be small distortions on top of the large quadratic distortion of the T walls. They suggested this small distortion could be associated with S-domains. The author's observations of domain walls in different samples of good quality $KCoF_3$, show no substructure in the domain pattern of $KCoF_3$. The details of the experiments will be presented in Chapters Six and Eight.

Hirakawa et al.(1961), following their interpretation of torque curves and predicting domain wall motion in $KNiF_3$, tried to observe any symmetry change or domain walls in $KNiF_3$ through the polarized microscope at about 150K but they could not observe any transformation from the cubic symmetry. Although no distortion had previously been observed in the antiferromagnetic region, the author has observed antiferromagnetic domain walls in highly perfect $KNiF_3$ crystals at the temperature range 4.2 - 200K using X-ray topographic techniques, (Safa et al.1975, Safa and Tanner 1976). The experiments revealed three types of domains with spin orientations parallel to the cube axes and it is concluded that a small distortion of the order of 10^{-5} exists below T_N. Domain walls are of 90° type and lie on $\{110\}$ planes. The details of the results and the analysis of the domain pattern will be presented in Chapters Six and Eight.

1.13 Domain Wall Motion in Cubic Antiferromagnetic Crystals

In cubic antiferromagnets, Petit et al.(1975) have observed a large gradual change in the field dependence of the magneto-optical spectra of cubic $KNiF_3$ at a moderate magnetic field. They measured the magnetic circular dichroism (MCD) and, their apparatus was able to detect dichroism of 10^{-6} in

absorption. They gave evidence for the detection of AF and SF phases by MCD and they concluded that the observed MCD in low magnetic field arose from the difference in energy between the up-spin and down-spin sublattices. Petit et al.(1975) reported that when they increased the magnetic field along the fourfold z axis, contrary to the classical "spin flop" inside a single domain, a continuous and gradual transition occurred at fields less than 10 KOe . The same type of experiments on $KNiF_3$ were performed using external stress by Pisarev et al.(1972) and Ferré et al.(1976). They concluded both magnetic field and stress experiments gave consistent results. Their results suggest that the gradual transition in their magneto-optical spectra is not due to a microscopic "spin flop" phenomenon which usually occurs suddenly and involves H_e and H_a, but rather to a reversible movement of twin walls at low magnetic field. Using X-ray synchrotron topography, the movement of domain walls in $KNiF_3$ and $KCoF_3$ was studied in a series of field steps up to 14 KOe at temperatures upward from 4.2K. These experiments which will be presented in Chapter Eight of this thesis, confirm that the above mentioned transition in magneto-optical spectra does, in fact, occur by domain wall movement and the mechanism is markedly different from the "spin flop" in uniaxial antiferromagnets. The X-ray synchrotron topography experiments show that walls whose plane contained the field direction were immobile and from analysis of the contrast it is concluded that walls move such that in high fields the spins lie in a plane perpendicular to the field direction and confirm suggestions originally put forward by Néel (1953).

CHAPTER TWO

X-RAY DIFFRACTION TOPOGRAPHY

2.1 Introduction

X-ray diffraction topography contains several diffraction techniques by which a topographical display of the microscopical defects in a crystal can be obtained. Lang (1970) in his review article "recent applications of X-ray topography" reviewed a considerable number of experimental works over the years. Bonse, Hart and Newkirk (1967), Austermann and Newkirk (1967), Isherwood and Wallace (1974), and Armstrong and Wu (1975) gave briefer reviews. The first book about X-ray diffraction topography by Tanner (1976) provides the basic information for taking and interpreting X-ray topographs and includes a considerable number of references. As X-ray topography is so well documented here a very brief introduction to the most useful techniques is presented.

X-ray diffraction topography is concerned with point to point variations in the directions or the intensities of X-rays that have been diffracted by a crystal and therefore one can obtain a direct mapping of the lattice plane topography of a crystal and from these variations the defect structures of the crystal may be studied.

X-ray topography has many similarities with electron microscopy of crystals. The great difference between these two techniques is the much inferior resolution of the X-ray technique. In X-ray topographs the images of dislocations are several micrometers whereas electron microscope images are a few hundred Ångstroms in width. In order to reveal dislocation images by X-ray topographs, because of the wide images, very low dislocation density crystals are required.

In electron microscopy very thin areas of specimen are prepared and examined with high magnification. Therefore in electron microscopy one should use specimens with very high dislocation densities or the chance of finding a dislocation in the field of view will be very small. However, X-ray topography has two outstanding aspects. Firstly, the X-rays will penetrate a considerable thickness of the crystal and one can study the bulk of the sample. Secondly, the technique is non-destructive. Therefore it is possible to take repeated X-ray topographs of organic crystals which would quickly volatilise or decompose in the electron microscope.

The aim of all X-ray topography techniques is to provide a picture of the distribution of defects in a crystal. Images can be formed either by "orientation" contrast or "extinction" contrast, Lang (1970) and Tanner (1976).

2.2 Orientation Contrast

Suppose the crystal is set in an X-ray beam of divergence $\Delta\phi$ so that Bragg reflection from a particular set of lattice planes is obtained for one or more characteristic lines. If the crystal contains a region misoriented with respect to the otherwise perfect crystal, contrast between the misoriented region and the crystal matrix will be observed if the misorientation exceeds $\Delta\phi$, as no diffraction can be obtained in the misoriented region. The variation of the diffracted beam from point-to-point on the image, is called orientation contrast. This kind of contrast can provide a measure of lattice misorientation and can be interpreted by simple geometrical relations without using dynamical theory. For characteristic divergent beam or continuous spectrum, if the crystal contains misoriented regions, the directions of

the diffracted beams from these regions can also cause orientation contrast. If the film is placed a considerable distance from the specimen, spatial overlap or separation occurs leading to enhanced or reduced intensity corresponding to the boundaries of the misoriented regions.

2.3 Extinction Contrast

The contrast arising from point to point variations in lattice perfection is termed "extinction" contrast. There is a different scattered intensity from the vicinity of the imperfection. Proper choice of diffraction geometry, X-ray wavelength and specimen thickness can provide optimum extinction contrast for a given volume of crystal. The nature of the image in this case can only be interpreted by dynamical diffraction theory.

2.4 The Schulz Method

This is a reflection technique (Schulz, 1954) using continuous radiation. A bundle of white X-rays divergent from a point source is diffracted by the crystal and recorded on a film, Fig.(2-1). Schulz introduced microfocus X-ray tubes into X-ray topography, and using the distance source-to-specimen and specimen-to-film about equal, he could gain sensitivity to orientation contrast in addition to extinction contrast. The resolution depends on the size of the focal spot of the X-ray tube. Fig.(2-1) shows the schematic arrangement of Schulz technique using a 25μm fine-focus tube. Guinier and Tennevin (1949) used a similar technique in transmission with white X-rays diverging from a point source. Using this technique, it is often possible to obtain several images on one film, each image being a reflection from different grains

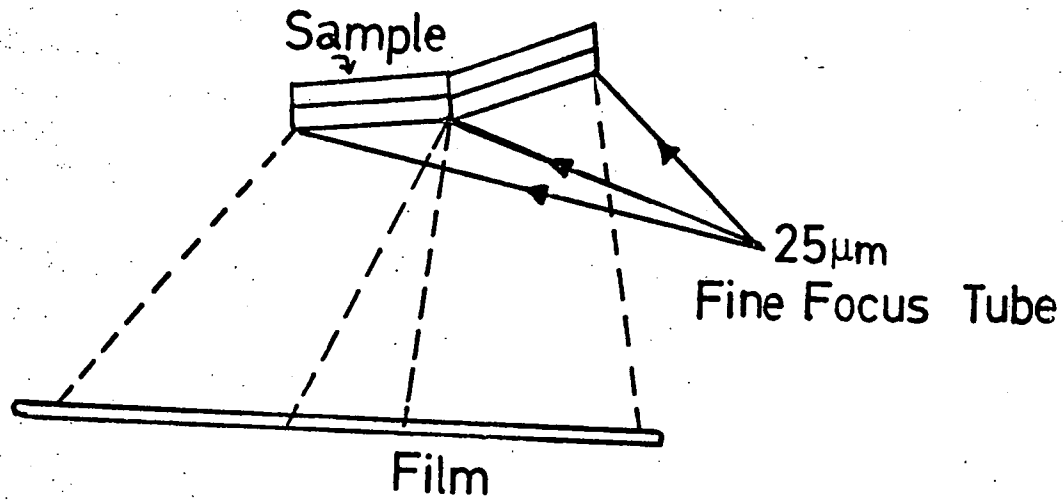

Fig.(2-1) Schematic arrangement for the Schulz technique.

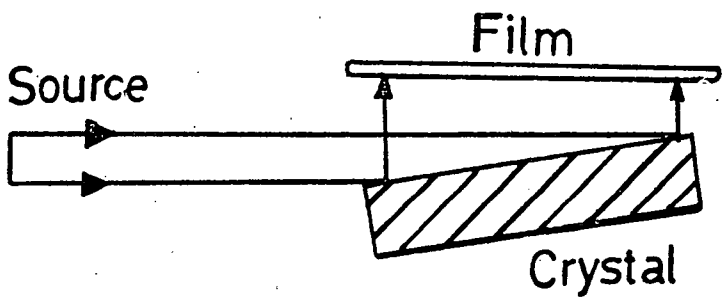

Fig.(2-2) Schematic arrangement of the Berg-Barrett technique.

or lattice planes. The reflections from a given family of crystal planes makes it possible to obtain photographs from which the scatter of the normals to these planes may be determined with an accuracy of 10 seconds of arc, even in a relatively large crystal. The resolution in this case is poor. Using synchrontron radiation with very small angular divergence of 10^{-4} radians, and enormous intensity Toumi et al. (1974), and recently Tanner, Safa, Midgley and Bordas (1976), Tanner, Safa, and Midgley (1977) and Tanner, Midgley and Safa (1977) have demonstrated that X-ray topographs in the Guinier-Tennevin mode with high resolution can be obtained with the exposure time of a few seconds. Hart (1975) using synchrotron radiation took topographs in reflection (Schulz mode) with geometrical resolution of the order of 1-2μm. Synchrotron topography has proved to be a very powerful and revolutionary technique, and as this technique has been used to observe domain wall movement with application of magnetic field up to 14 KOe in low temperatures, Chapter Three of this thesis is devoted to synchrotron topography.

2.5 Berg-Barrett Topography

This method originates from work by Berg (1931) and Barrett (1945). Fig.(2-2) shows the essential features of this method. The single crystal is set to Bragg - reflect the characteristic radiation from a chosen set of lattice planes, using an extended source. As the Kα line is in fact a closely spaced $K\alpha_1$ - $K\alpha_2$ doublet, this results in a doubling of the image of any defect due to the different angles of the two diffracted beams. When the recording plate is close to the specimen, the separation of double images due to the

$K\alpha_1$ - $K\alpha_2$ doublet is negligibly small. By putting a fine-grain plate extremely close to the specimen, resolution of about 1μm can be achieved. As this is a reflection technique and X-rays penetrate only a few micrometers into the crystal, effectively a very thin slice of the crystal is examined and therefore the technique can be used for much higher dislocation densities than in transmission techniques. In transmission the overlapping of images from dislocations at different depths in the crystal limits the useful dislocation density to less than about $10^4 cm^{-2}$ compared with about $10^6 cm^{-2}$ in reflection. Therefore for assessing crystal quality, surface reflection techniques should be employed first of all.

2.6 Lang's Method

This is a very widely used and powerful technique which is sensitive to both extinction and orientation contrast, where the orientation sensitivity is about 5×10^{-4}. In this method, a ribbon X-ray beam is collinated to a sufficiently small angular divergence that only one characteristic wavelength can be diffracted by a set of planes of the crystal. Therefore simultaneous diffraction of the $K\alpha_1$ and $K\alpha_2$ lines is avoided and only the $K\alpha_1$ will be used, because of its greater intensity. The typical angular divergence is 5×10^{-4} radians which is greater than the perfect crystal reflecting range of 10^{-5} radians.

2.6.1 Section Topographs (Lang 1958)

The diffraction geometry of the section topograph is simple Fig.(2-3). The crystal is set such that the characteristic X-ray is Bragg-reflected by planes parallel to those schematically indicated by the lines normal to the X-ray

entrance and exit surfaces. A diffracted beam issues from the rear surface of the specimen, passes through a slit and is recorded on the photographic emulsion. The slit is used to eliminate the direct beam. Section topographs provide very useful information from a small region of crystal when the beam is narrow compared with the base of Borrmann fan, i.e. $2t\sin\theta_B$ (t is crystal thickness, and θ_B is the Bragg angle). As the width of the beam practically can not be less than 10μm, application of section topography for thin crystals is not possible. The useful feature of the section topograph is that it can be used to locate the position of imperfections within the crystal and also determine the direction of energy flow in the crystal.

2.6.2 Projection Topographs (Lang 1959)

In the projection topography technique, the crystal and film are both mounted on an accurate linear traversing mechanism. During the exposure they move back and forth together, so that the whole area of interest in the specimen will be scanned by the ribbon incident beam. The direction of traverse is shown by arrows in Fig.(2-3). As the two-dimensional pattern on the film is a projection of the crystal slab and its imperfection content, Lang (1959) called it the "projection topograph". He showed that a projection topograph is equivalent to a superposition of many section topographs. Projection topography presents a useful survey of the overall distribution of imperfections. Stereo topographs are often taken as a pair in hkl and $\bar{h}\bar{k}\bar{l}$ reflections, and such stereos give a three dimensional picture of the defects within the volume of the crystal slab. Lang (1963) modified the pro-

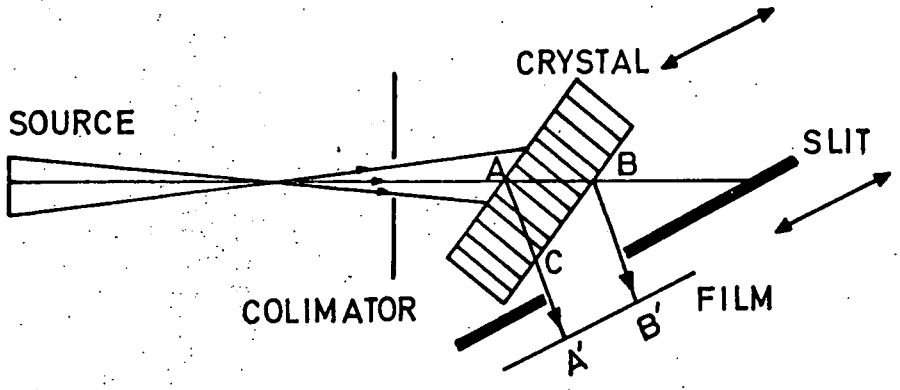

FIG.(2-3) Arrangements for Lang's transmission technique, projection topographs are obtained by scanning the crystal and film across the beam.

In the case of section topographs the crystal and the film are stationary and the beam is narrow.

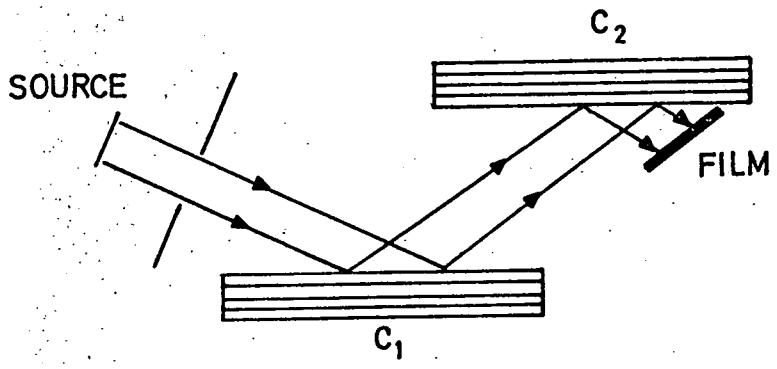

FIG. (2-5) The double crystal arrangement

jection method so that images are recorded only from imperfections which lie within a chosen range of depth in the crystal specimen. This technique of "limited projection topographs" allows easier study of internal imperfections by eliminating images of surface damage. In this technique the diffracted beam slits are set to cut into the beam and allow only part of the diffracted beam corresponding to an effective depth of the crystal to reach the film. Lang (1963) also performed "direct beam topography" with nearly perfect crystals. In this case he recorded the directly transmitted beam on the photographic plate. The dislocation diffraction contrast obtained in this way, when X-ray absorption is low, is complementary to that produced in the usual diffracted beam topograph.

2.7 Topographic Resolution

(a) Vertical resolution

Vertical resolution on X-ray topographs, that is, in the direction perpendicular to the plane of incident and diffracted rays, is of purely geometrical nature and the resolution δ is given by Fig.(2-4).

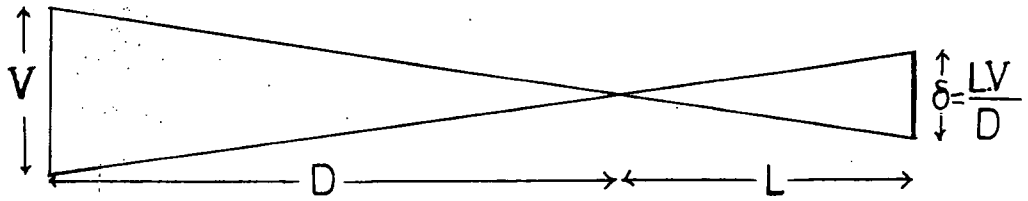

Fig. 2-4. Vertical resolution criteria

where L is the specimen to plate distance, D is the source to specimen distance, and V is the projected height of the source. When great care is taken to place the photographic plate within 1cm of the crystal, and

substituting typical values for V and D, a resolution in the order of a few microns is obtained. For high quality topographs a small specimen-plate distance should always be aimed for.

(b) Horizontal resolution

The topographic resolution in the plane of incident and diffracted rays, horizontal resolution, depends upon the wavelength spread of the X-rays and their dispersion by the specimen, the intrinsic angular range of reflection of specimen crystal and vibrations of specimen during the exposure.

The grain size of the nuclear emulsion plays an important part in obtaining high resolution topographs. The recommended recording medium for X-ray topographic images is Ilford L4 Nuclear Emulsion. It possesses a grain size well below the topographic resolution set by geometrical and other factors. Care should be taken to place the emulsion plates normal to the diffracted beam. To obtain a resolution of 1μm, the width of the projection of the ray in the emulsion must not exceed this and one can see that in a 100μm emulsion the ray must be within $\frac{1}{2}^{o}$ of the normal whereas with a 25μm emulsion a 2^{o} error can be tolerated. Emulsions thicker than 100μm are difficult to process and also suffer from loss of resolution if the beam does not pass normally through the emulsion. Compared with thick emulsions, thin emulsions give greater statistical fluctuations in the number of the developed grains per unit area and they do not have as high a usable photographic density range as thicker emulsions. Therefore a compromise between the efficiency and resolution should be reached. Details of

experimental procedure and processing of the nuclear emulsion plates can be found in Lang's (1970) article and Tanner's (1976) book.

2.8. The Double-Crystal Topography

This topographic technique was developed independently by Bond and Andrus (1952) and Bonse and Kappler (1958). In this method, Fig.(2-5), the reference crystal and specimen consist of the same kind of material so that exactly the same spacing of reflecting planes can be used in both crystals. In this high sensitivity ((+-) parallel arrangement X-rays are diffracted successively from two sets of lattice planes of equal spacing first in the hkl and $\bar{h}\bar{k}\bar{l}$. In this geometry, the double crystal technique is extremely sensitive to lattice distortion or misorientation, and the rocking curve obtained when one of the crystals is rotated is very narrow, typically a few seconds of arc. This makes the method very suitable for measuring small tilts. When the specimen is slightly offset from the exact parallel position, that is, on the flank of the rocking curve, strains of $|\Delta d/d| \lesssim 10^{-8}$-$10^{-9}$ can be detected, Bonse et al (1967). Deformations of this magnitude occur at distances of up to 50 or 100μm from the cores of single dislocations, depending upon the material examined. Using this topographic technique Aldred and Hart (1973) found that lattice parameter variations in silicon crystals claimed free from carbon were of only a few parts in 10^8. For identical lattice parameters in the two crystals the (+-) parallel setting is non-dispersive in the sense that at any angular setting all wavelengths are diffracted. If a slight difference is made in the lattice parameters, only a band of wave-

length diffracts at any one setting and the angular sensitivity drops. However, Okazaki and Kawaminami (1973) using very high Bragg angles and white radiation could measure the lattice parameter of $KNiF_3$ with quite a high precision to one part in 10^5 even when two different materials were used for the specimen and reference crystals.

2.9 X-Ray Diffraction Theories

As seen in the above sections, topographic techniques for studying defects in nearly perfect crystals have been developed and are being widely used. The principle of these techniques are based mainly on the difference in the intensities of X-rays diffracted by deformed and perfect regions of the crystal. There are two main diffraction theories for waves having very short wavelength, the approximate but widely used "Kinematical theory" and the more fundamental "dynamical theory". Batterman and Cole (1964) reviewed detailed mathematical expositions of the dynamical theory, Balchin and Whitehouse (1974) also give a brief review, and Authier (1970) and Tanner (1976) give the theoretical basis necessary for interpretation of the contrast of defects on X-ray topographs.

2.9.1 The Kinematical Theory

The main assumption of the Kinematical or geometrical theory is that the amplitudes of all X-rays incident upon the diffracting centres in the crystal have the same value. Thus the interactions between the incident and the refracted waves are neglected. The wavelength of X-rays is also assumed to be unchanged as it passes from vacuum into the crystal.

For thin crystals or crystals constituted of small regions reflecting the incident beam independently, that is, the ideally imperfect crystals, the geometrical theory may be employed satisfactorily to get information on the crystal structure. However, for large single crystals which are also highly perfect, the amplitude of a diffracted wave becomes comparable with that of the incident beam.

2.9.2 The Dynamical Theory

The theory of dynamical diffraction describes the interaction of electromagnetic waves with a three dimensional array of electrostatic dipoles Ewald (1916, 1917) and later as a three dimensional distribution of dielectric susceptibility, Laue (1931). Basically, the problem is to solve Maxwell's equations for a medium with periodic susceptibility. One finds that solutions of the form

$$\underline{D} = \exp i\omega t \sum_g \underline{D}_g \exp(-2\pi i \underline{K}_g \cdot \underline{r}) \qquad 2\text{-}1$$

satisfy, provided that the wavevectors $\underline{K}_g$ are related by the Laue equation

$$\underline{K}_g = \underline{K}_o + \underline{g} \qquad 2\text{-}2$$

where $\underline{K}_g$ is the wave vector of a diffracted wave, inside the crystal, and $\underline{K}_o$ is the vector of the field which is closest to that of the incident wave, and $\underline{g}$ is the reciprocal lattice vector. We see from the equation (2-1) that solutions $\underline{D}$ inside the crystal consist of a superposition of plane waves, the wave vectors of which are related by reciprocal lattice translations. The superposition is a "wave field". These plane waves have wave vectors $\underline{K}_g$ derived from a single primary

wave $\underline{K}_o$. Expression (2-2) shows that all the wave vectors of a given wave-field can also be deduced from one another by translations equal to reciprocal lattice vectors. If we draw these wave vectors from the various reciprocal lattice points, we find that they define a common point P, called "tie-point", which characterizes the wave-field geometrically, Fig. (2-6).

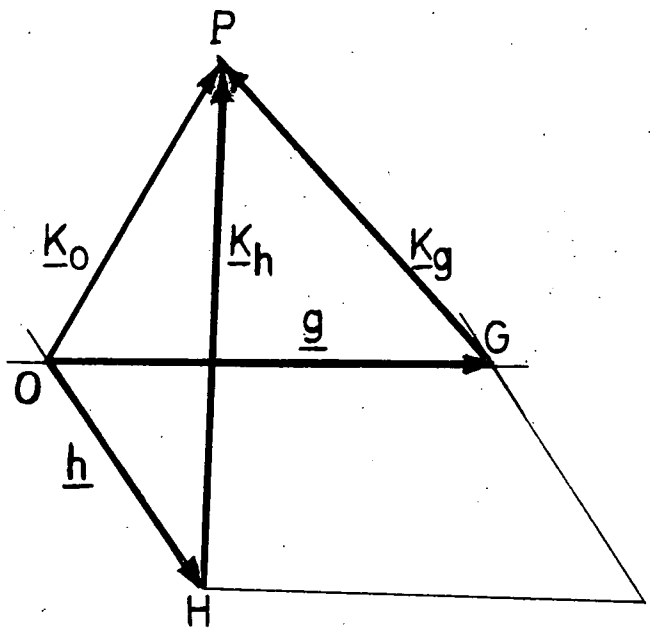

Fig. (2-6). Construction of the tie-point in reciprocal space.

Theoretically, a wave-field is constituted by an infinite number of waves. Usually in the case of X-ray diffraction only two waves have significant amplitude: the incident wave after refraction $\underline{K}_o$ and the Bragg reflected wave $\underline{K}_g$. Then (neglecting time dependence)

$$\underline{D} = \underline{D}_o \exp(-2\pi i\, \underline{K}_o \cdot \underline{r}) + \underline{D}_g \exp(-2\pi i\, \underline{K}_g \cdot \underline{r}) \qquad 2\text{-}3$$

Substitution of this equation into Maxwell's equations and solving for non-zero values of wave amplitudes, $\underline{D}_o$ and $\underline{D}_g$, gives a relationship between $\underline{K}_o$ and $\underline{K}_g$ in reciprocal space. This relation can be plotted graphically, and is known as the dispersion surface. The dispersion surface represents the locus of all primary wave vectors $\underline{K}_o$ which give rise to a diffracted beam $\underline{K}_g$ passing towards G under conditions which approximate to the Bragg condition. Therefore the dispersion surface is the locus of the tie-point P. The intersection of the dispersion surface with a plane passing through O and G is a hyperbola, Fig.(2-7), of which the asymptotes are the tangents to the circles centred in O and G respectively and with radii

$$|\underline{K}_o| = k(1 + \frac{\chi_o}{2}) = kn \qquad 2\text{-}4$$

where k is the vacuum wave vector, χ_o is the dielectric susceptibility and n the refractive index.

Far from a Bragg reflection there is only one wave excited in the crystal and the wave vectors lie on spheres centred on O and G of radii $k(1 + \frac{\chi_o}{2})$. Close to Bragg reflection, the crystal potential rises the degeneracy and the dispersion surface has two branches for each polarization, corresponding to D_g/D_o positive or negative (i.e. the component plane waves either in phase or phase shifted by π)

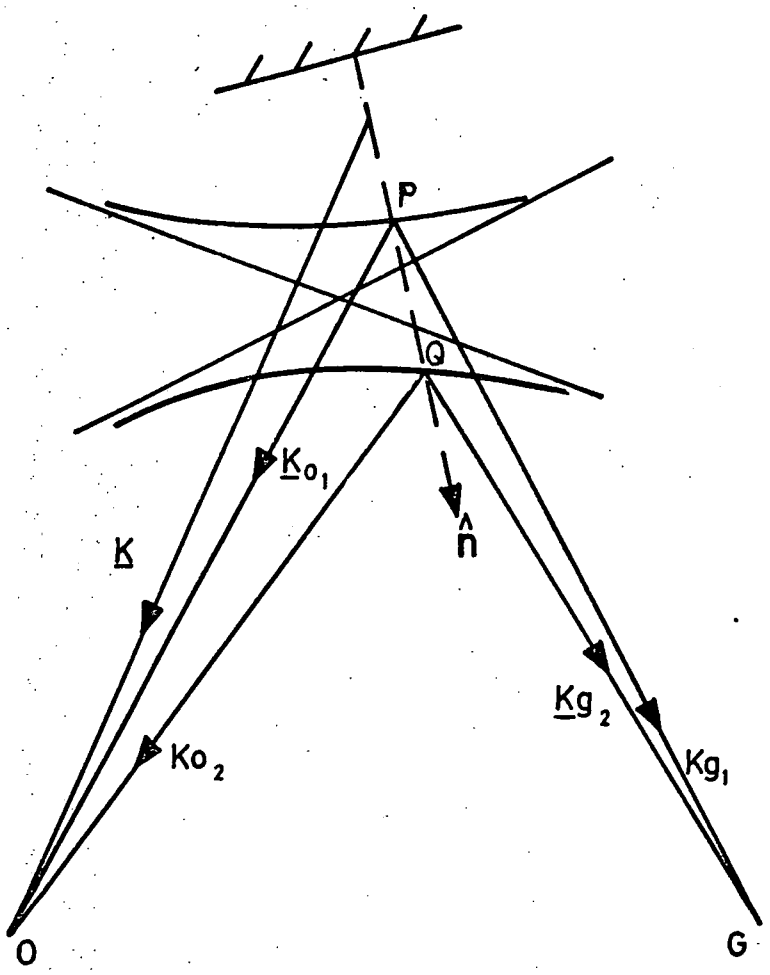

FIG. (2-7), Construction of the dispersion surface (after Tanner 1976)

Directions of the refracted and diffracted beams must satisfy the boundary conditions at the surface of the crystal. The continuity of the tangential components of the wave vectors at the crystal surface is the most important condition. This implies that the ends of the incident wave vector, $\underline{k}_o$, which excites the refracted wave $\underline{K}_o$ must lie on a normal to the crystal surface and this is shown for the two tie points P and Q in Fig. (2-7); $\underline{k}_o$ will in general be directed at or near the Laue point. The tie points for $\underline{K}_{o1}$ and $\underline{K}_{g1}$ or $\underline{K}_{o2}$ and $\underline{K}_{g2}$ will then be at P and Q. The energy flow is always perpendicular to the dispersion surface. The wave vectors $\underline{K}_{g1}$ and $\underline{K}_{g2}$ then define two diffracted X-ray beams which follow separate paths through the crystal under Bragg diffracting conditions. When the beams reach the exit surface of the crystal, both waves are decoupled giving rise to an independent beam outside the crystal. Thus there are four outgoing beams. This result was first observed experimentally by Authier (1961) and confirmed the physical reality of wavefields. However, it is only under very special circumstances that it is possible to describe the incident wave as a plane wave because the divergence of the incident beam is usually large compared with the perfect crystal reflecting range. In the case of a section topograph, Fig.(2-8), the incident beam is very divergent. All tie points on the dispersion surface are excited simultaneously and X-rays propagate along all possible paths. These paths fill the Borrmann triangle ABC (Fig.2-8), so that along any direction two wavefields (one from branch 1 and the other from branch 2) propagate. The two wave fields have a constant phase difference between

them and so will interfere. Along the base BC of the Borrmann triangle, the phase difference between the arriving wave fields differs and section topograph Pendellösung fringes can be obtained. These fringes were first observed by Kato and Lang (1959) and interpreted by Kato (1961). The phase difference between the wavefields is proportional to the structure factor. Kato (1969), from section topograph pendellösung fringe measurements in wedge crystal, could measure the structure factor with high accuracy.

2.10 Contrast of Dislocations

Authier (1967, 1970) characterized three types of images which contribute to the contrast of dislocation: "direct", "dynamical" and "intermediary". Fig.(2-9) shows how these arise.

2.10.1 Direct Image

The dislocation cuts the direct beam at D_1. The lattice planes are deformed in the vicinity of the dislocation. As the X-ray source is polychromatic, some of the X-rays not diffracted by the perfect crystal are diffracted by the strained region provided the effective misorientation is larger than $\Delta\theta_{\frac{1}{2}}$, the width of the reflecting range for the perfect crystal and less than the total divergence of the direct beam. Such a diffracted beam then can be received at i_1, on the photographic plate. i_1, is the "direct image" and is superposed on the diffracted beam by the perfect crystal and has a dark contrast with respect to the background. The direct image can be said in first approximation to be the image of a small imperfect crystal imbedded in the direct beam. In favourable

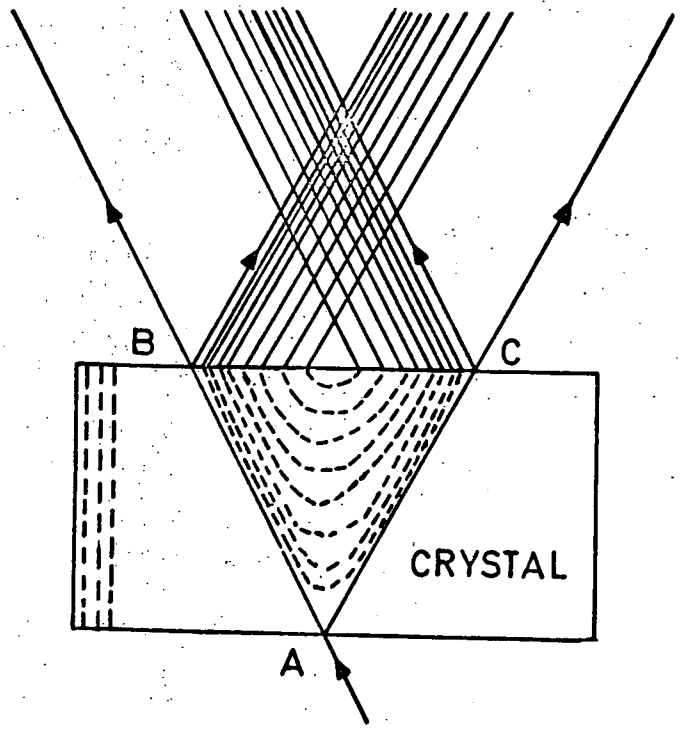

FIG.(2 - 8) Propagation of wavefields in direct space

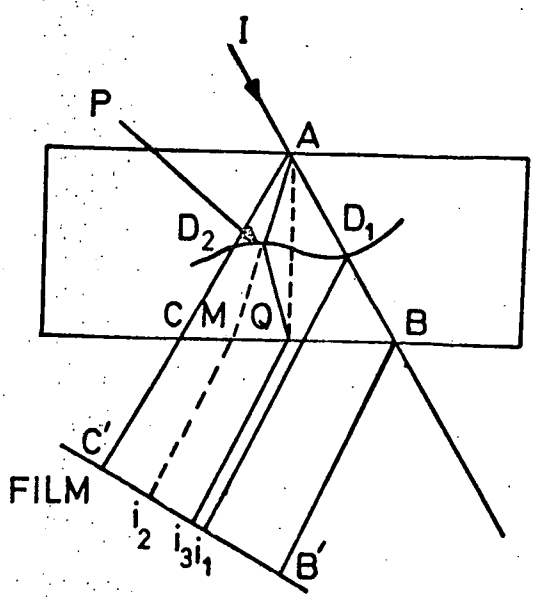

FIG.(2 - 9) Principle of dislocation image formation in transmission topographs, i_1 direct image; i_2 dynamic image; i_3 intermediary image. (after Authier 1967)

circumstances such as, when $\underline{g}.\underline{b}$ is equal to two or more, or with a high extinction distance, dislocations can show double contrast. Authier showed that this is a general phenomenon, arising as a consequence of the form of the dislocation strain field. Double contrast of dislocations has also been observed in synchrotron topographs of silicon and $KCoF_3$ crystals by Tanner, Midgley and Safa (1977) and will be shown in the third Chapter. The dislocation image width can be estimated, Lang (1970). In the case of a pure screw dislocation for $\underline{g} \parallel \underline{b}$, the misorientation at a distance r from the core of the dislocation is

$$\delta(\Delta\theta) = \frac{b}{2r\pi} \qquad 2\text{-}5a$$

The perfect crystal reflecting range for non-absorbing symmetrical Laue condition is given by

$$\theta_{\frac{1}{2}} = 2/g\,\xi_g = 2\, r_e\, \lambda^2 C (F_g F_{\bar{g}})^{\frac{1}{2}}/\pi v_c \,\mathrm{Sin}\, 2\,\theta \qquad 2\text{-}5b$$

where ξ_g is the extinction distance related to the structure factor F_g, r_e is the classical electron radius, v_c is the volume of the unit cell and $C = 1$ or $\mathrm{Cos}\, 2\,\theta_B$ for σ or π polarization respectively. Equating (2-5a) and (2-5b), one obtains an estimate of the screw dislocation image width $V_s = 2r$,

$$V_s = \xi_g/2\pi \;|\, \underline{g}.\underline{b}\,| \qquad 2\text{-}6$$

For an edge dislocation, the image width is given by

$$V_E = \frac{0.88}{\pi}\, \xi_g \cdot |\, \underline{g}.\underline{b}\,| \qquad 2\,7$$

The value of X-ray extinction distance depends on the wavelength, and the geometry of the reflection, and is typically tens of microns. Thus direct image widths of dislocations are generally upwards of a few micrometers. Image widths

predicted by equations (2-6) and (2-7) agree quite well with observations. Under low absorption conditions most of the dislocation images on a projection topograph are direct images.

Generally, a dislocation in a given Bragg reflection is invisible if its displacement field has no component normal to the Bragg plane used. In other words, for invisibility of a dislocation its effective misorientation should be zero. From this it follows that for a pure screw dislocation the effective misorientation is zero when $\underline{g}.\underline{b} = 0$ and for a pure edge dislocation it is zero when both $\underline{g}.\underline{b} = 0$ and $\underline{g}.\underline{b}. \times \underline{\ell} = 0$, and thus in reflections satisfying these conditions, the dislocation is invisible. Here $\underline{g}$ is the diffraction vector, $\underline{b}$ is the Burgers vector and $\underline{\ell}$ is the direction of the dislocation line. If we find two reflections with non-parallel diffracting vectors in which the dislocation is invisible, the direction of Burgers vector $\underline{b}$ can be determined unambiguously. Mixed dislocations can never completely disappear.

2.10.2 Dynamical Images

In Fig. (2-9) on crossing the dislocation wave fields propagating along AP will excite wave fields propagating in a parallel direction AM and new wave fields having a tie-point on the other branch of the dispersion surface and propagating along PQ. Therefore only part of the energy of the fields propagating along AP will be found along AM. Also the path of wave fields passing through the less strained region further from the core are curved and therefore deviated from their original direction. The result of both these effects is a

depletion in the direction APM of wave fields crossing a dislocation, which gives rise to a light shadow at i_2 on the photographic plate. The width of this kind of image depends on the dislocation depth and its position relative to the edges of the Borrmann fan.

2.10.3 Intermediary Image

Wave fields created by interbranch scattering in the more strained regions propagate along PQ giving rise to a third image, i_3, on the topograph which has been called the "intermediary" image. As the new wavefields interfere with the original wavefields, the intermediary image shows an oscillatory contrast. As the Borrmann fan is filled with wave fields propagating in different directions, the dynamical and intermediary images have much poorer spatial resolution than the direct image.

2.11 Domain Wall Observations

The contrast of magnetic domain walls in X-ray topography is produced by the magnetostrictive deformation. The visibility of magnetic domains on X-ray topographs cannot be explained by the direct interaction between the X-rays and the magnetization.

Using the Berg-Barrett method and a double crystal diffractometer, Merz (1960) performed the pioneering observation of magnetic domains by X-ray topography. He took advantage of the high value of magnetostriction of Cobalt Zinc ferrite and adjusted the crystal so that the diffraction condition was satisfied for some domains only. The image of these domains were recorded on the topographs. Polcarova and Lang

(1962), using the Lang technique were able to observe the domain patterns in Fe-Si with good contrast and resolution. Iron-silicon, has a positive magnetostriction constant λ. Consequently, the crystal lattice is elongated in the direction of magnetization and shortened in the direction normal to it. As the easy directions of magnetization are $\langle 100 \rangle$, a small tetragonal distortion with the ratio

$$c/a = 1 + \frac{3}{2}\lambda = 1 + 2 \times 10^{-5} \qquad 2\text{-}8$$

occurs in the magnetization direction. The distortion is very small, but large enough to influence the X-ray wavefield crossing the domain walls, and the contrast of the 90° wall results. As there is no misorientation between 180° domains, they are not visible on the topographs, but their position can be determined from the arrangement of the 90° domains. Fig. (2-10) shows a (110) 90° wall, where the magnetization $\underline{M}$ is along [100] in domain I, and M_2 is along [010] in domain II. Experiments of Polcarova and Kaczer (1967) and Polcarova (1969) have shown that (110) 90° walls are invisible in reflections such that,

$$(\underline{M}_2 - \underline{M}_1) \cdot \underline{g} = \Delta\underline{M} \cdot \underline{g} = 0 \qquad 2\text{-}9$$

i.e. the walls having $\Delta\underline{M}$ normal to the diffraction vector $\underline{g}$ are not visible on the topograph. Polcarova and Gemperlova (1969) studied the contrast of domain walls theoretically. They considered the distortion at a 90° domain wall and showed that it was identical to a coherent crystallographic twin, provided that the wall thickness was neglected. The domain wall widths are usually of the order of hundreds of Ångstroms and this is negligible on the scale of X-ray extinction distances. This coherent twin model is in good agreement with

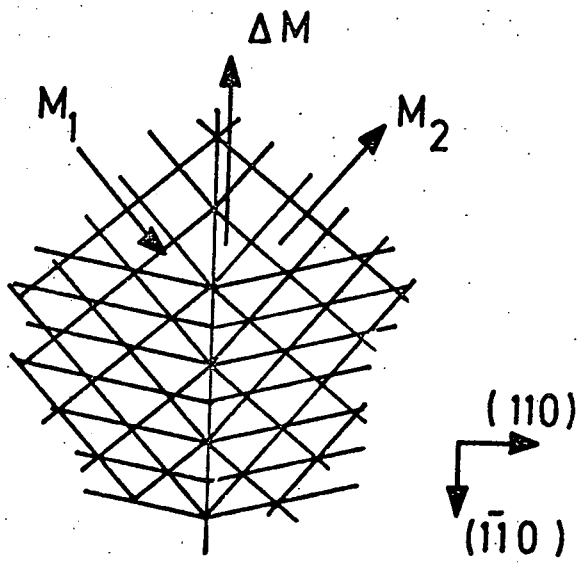

Fig.(2-10) Model of a flat 90° wall lying in the (110) plane.

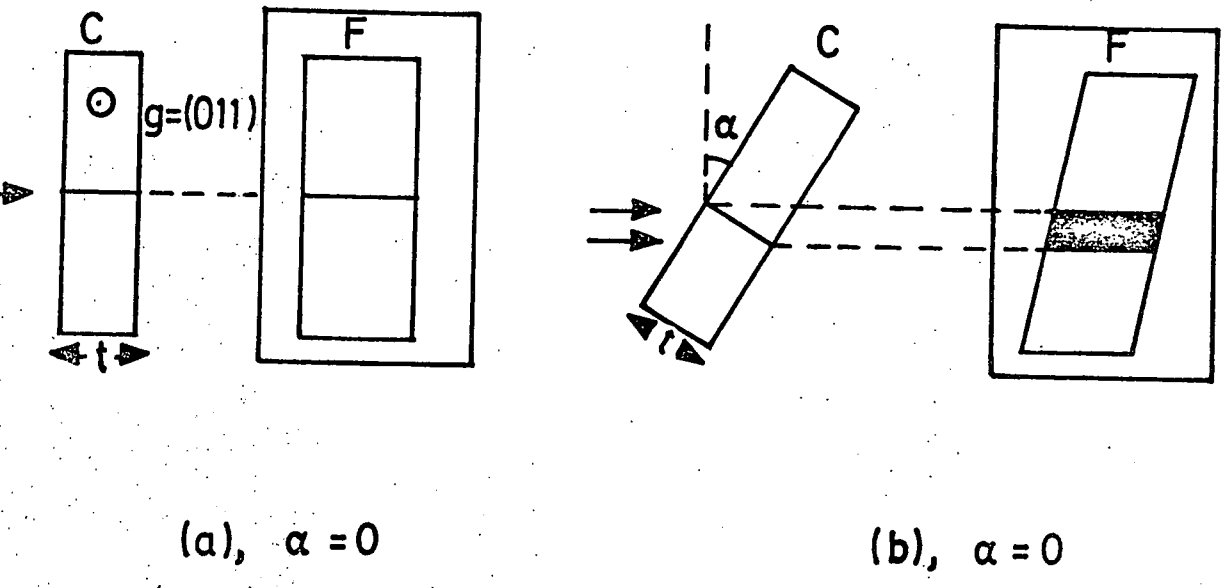

Fig.(2-11) Image of wall on photographic film F depending on rotation of crystal C around g vector. (After Polcarova 1969)

experimental observations. A quantitative comparison between the calculated and observed contrast was performed by Polcarova and Lang (1968) for the special case of 110 diffraction on a (001) plate of Si-Fe containing domain walls parallel to the $(1\bar{1}0)$ planes. It was shown that the wall appears as a dark band if $\Delta \underline{M}.\underline{g} > 0$, and a white one if $\Delta \underline{M}.\underline{g} < 0$. The width of the contrast band is not usually related to the intrinsic wall thickness, but it depends on the tilt of the sample about the diffraction vector $\underline{g}$. If the (001) plate of Si-Fe is rotated around the $\underline{g} = [110]$ vector, the image of the $[1\bar{1}0]$ wall appears as a broad band, the width of which is $t.\sin\alpha$, α being the angle of rotation, and t is the thickness of the sample. As seen in Fig.(2-11) the image is a faint narrow line for $\alpha = 0$, but it increases with increasing α independently of the sense of rotation. Polcarova (1969) noticed that the contrast was also dependent on the absorption, i.e. on the value of μt. (μ is the linear absorption coefficient) and her recent calculations based on the dynamical theory of diffraction show the dependence of the contrast on absorption and agree with experiments, Polcarova (1973).

The origin of the contrast depends on the magnitude of the magnetostriction contrast. For example in the antiferromagnetic crystal NiO, the magnetostriction is large and changes the interaxial angles by several minutes of arc. Therefore orientation contrast is observed. Using a small beam divergence, only one set of domains satisfy the Bragg condition at once and, angular misorientation between the domains can be measured from the rocking curve separation. Using the Berg-Barrett technique, the angular misorientation

of domains in NiO was measured by Kranjc (1969). When the magnetostriction is small, both domains diffract simultaneously and no orientation contrast is observed.

X-ray topography is a non-destructive technique for repeated observations of the internal domain structures in relatively thick non-transparent samples. This technique is extremely useful for the study of the fine structure of walls inside the specimen, the examination of stress fields around domain walls, and observation of domain wall interactions with other defects.

As there is no net magnetization in classical antiferromagnets, domains cannot be observed by the Bitter colloid, Faraday, or Kerr techniques. In some transparent antiferromagnets with large birefringence, e.g. NiO, the domains can be observed by optical microscopy, but in the case of $KNiF_3$, the birefringence is extremely low and domains have not been observed clearly. Thus X-ray topography is the only technique suitable for domain observation in some antiferromagnets. [X-ray topographic observations of domain walls in NiO, CoO, Cr, $KCoF_3$ and $KNiF_3$ were reviewed in sections (1-10) and (1-12).]

CHAPTER THREE

X-RAY SYNCHROTRON TOPOGRAPHY

3.1 Synchrotron Radiation

An electron accelerated in a circular orbit in a synchrotron or storage ring emits electromagnetic radiation, which in the very highly relativistic limit, is seen in the laboratory frame as a narrow cone peaked in the forward direction. The radiated power is proportional to the fourth power of the electron energy. Synchrotron radiation provides a very intense source of electromagnetic radiation for solid state Physicists. The beam is totally polarized in the orbit plane for radiation emitted along the tangent to the orbit. Because of betatron oscillations, the radiation has a continuous spectrum and extends through the visible and ultraviolet to the X-ray region. Due to the relativistic effects, the radiation is confined into an angle $\psi \sim \frac{m_o c^2}{E}$, $m_o c^2$ being the rest mass of an electron and E is the energy of the accelerated electron. Fig.(3-1) shows the calculated synchrotron radiation spectra for NINA, at Daresbury, Poole (1975). As seen, for 5 Gev. electrons the highest photon flux is around 1Å and the corresponding angular divergence is about 10^{-4} rad.

3.2 Synchrotron Topography

In Section (2-4) it was mentioned that, Guinier and Tennevin (1949), and Schulz (1954) performed white X-ray diffraction topography in the transmission and reflection modes, but the resolution obtained was very poor with stand-

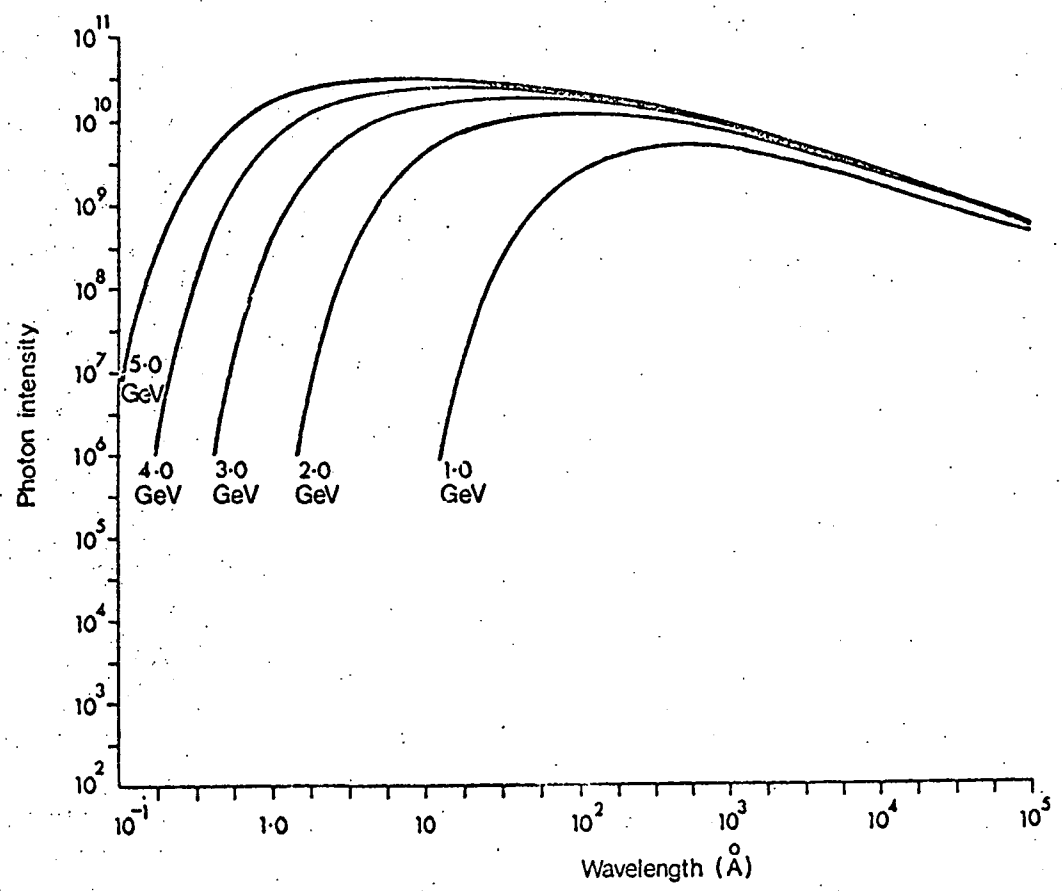

Fig.(3-1) Synchrotron radiation spectra from NINA. Photons/s/mA beam/mrad horizontally within a 0.1% bandwidth. (After Poole 1975)

ard sources. Recently the availability of synchrotron radiation in the X-ray region of the elctromagnetic spectrum with small angular divergence ($\sim 10^{-4}$ rad.) and enormous intensity has revolutionized X-ray topography. The technique is essentially the same as the Guinier and Tennevin, or Schulz methods. With continuous radiation, each set of crystal planes can select its own wavelength for a Bragg reflection and, just as in the well known Laue technique for crystal orientation, a pattern of "spots" is obtained. Due to the relatively wide beam no scanning of the crystal across the beam is required, and each Laue spot becomes an image of the crystal. Within each image, crystal defects are revealed and each spot provides as much information as a conventional Lang topograph, Tuomi et al. (1974). Fig.(3-2) shows the Laue pattern taken with synchrotron radiation of a Dy PO_4 crystal. Each image or topograph of this crystal shows the defects such as dislocations or growth bands. Thus by taking one exposure, one is able to analyse the defects, using the contrast in the different reflections. As the intensity of synchrotron radiation is of the order of 10^3 times higher than the intensity coming out of a rotating anode generator, exposure times are expected to be of a few seconds.

3.3 Intensity and Image Formation

Considering the effect of the following factors, (a) the structure factor F_{hkl}, (b) the effect of non-ideal Bragg conditions, (c) the continuous spectrum of radiation, (d) the absorption factor of the crystal, Tuomi et al.(1974) calculated the intensity of Laue reflections to be proportional to:

$$I_{hkl} \sim P(\lambda) \cdot F_{hkl} \frac{\lambda^3}{\mathrm{Sin}^2\theta} e^{-\mu t} \qquad 3\text{-}1$$

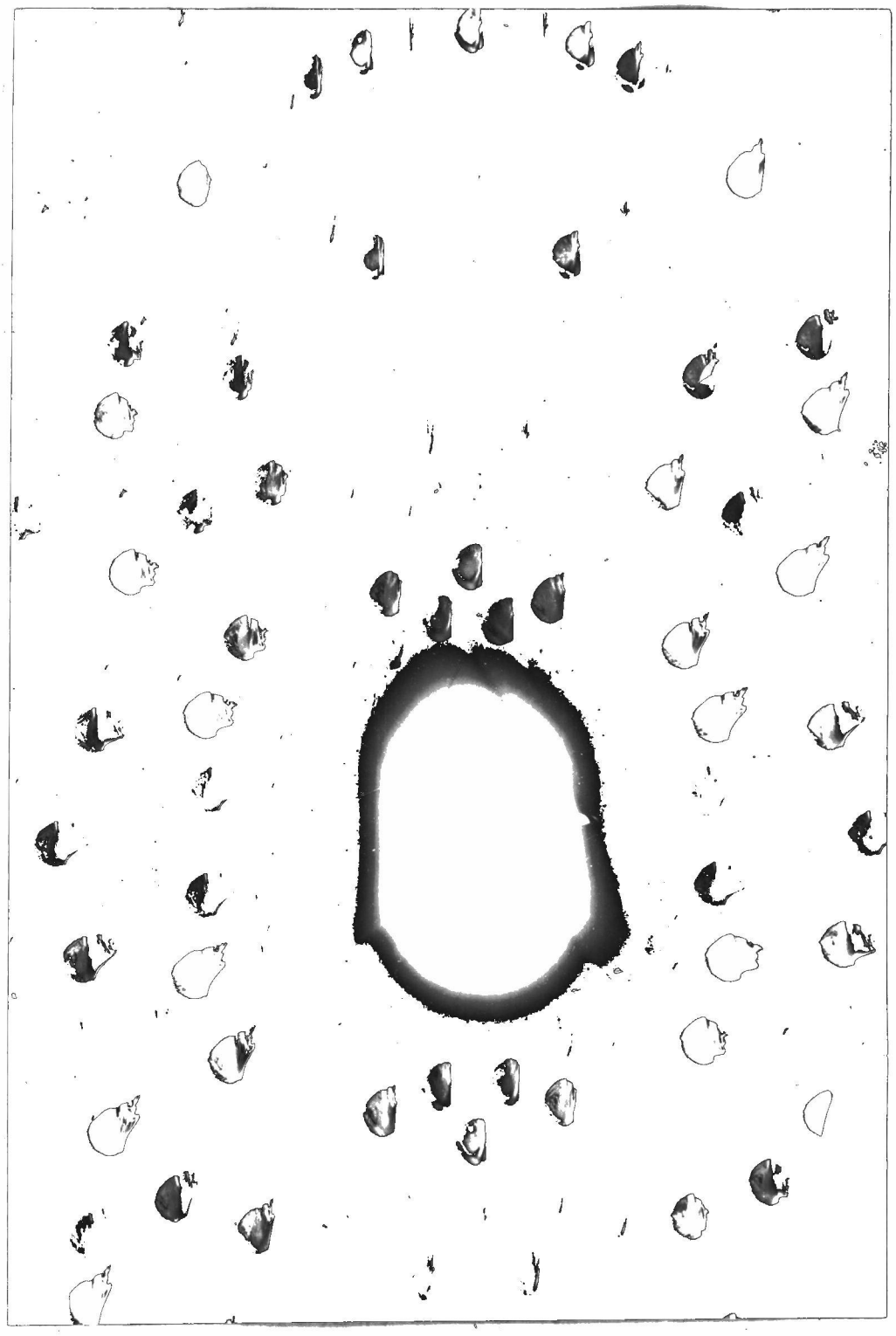

Fig. (3-2) Laue pattern of a $DyPO_4$ crystal taken with synchrotron radiation. Each "spot" is an image of the crystal within which contrast from imperfections can be seen. 5 Gev, 10mA, 50s exposure, L_4 10μm nuclear emulsion.

where $P(\lambda)$ is the radiated power per unit wavelength of the source, F_{hkl} is the structure factor of (hkl) diffracting planes, μ the absorption coefficient of the crystal, and t the thickness of the crystal. Here anomalous transmission is neglected. Tuomi et al (1974) also mentioned the effects of the polarization of synchrotron radiation and temperature on the intensity of the diffracted beam. Hart (1975) obtained the same results as (3-1) for the intensity of the diffracted beam, but he mentioned that the absorption of X-rays in air and the variation of the film sensitivity with X-ray wavelength are important factors which have been ignored by Tuomi et al. In interpreting the image features one must be aware that different orders of reflection are superimposed on the same topograph. As Hart (1975) and Tuomi et al (1974) point out, the lowest harmonic corresponding to the largest λ should be predominate but its intensity is heavily reduced by absorption. On the other hand higher harmonics formed with almost unabsorbed hard radiations have their contribution reduced by the lack of sensitivity of X-ray emulsions in the short wavelength range. The optimum condition is to choose a diffraction condition, in which the bulk of the diffracted beam belongs to only one order of reflection, with a strong intensity.

3.4 Resolution

In synchrotron topography, unlike conventional X-ray diffraction topography with characteristic radiation the whole source contributes to the intensity diffracted by each point in the sample. Therefore the spatial resolution depends upon the effective source size. For distance from

source to the crystal L, and the crystal to the plate distance x, the horizontal and vertical resolutions are given by

$$\begin{cases} r_h = x \frac{h}{L} \\ r_v = x \frac{v}{L} \end{cases} \qquad 3\text{-}2$$

where h and v are the horizontal and vertical dimensions of the source.

Table (3-1) shows the relevant quantities for the DESY and NINA synchrotron facilities

Source	Source dimensions (mm)	L(m)	x(m)	r(μm)
NINA	h = v = 0.5	47	0.05	0.5
DESY	h = 8 v = 4	40	0.05	r_h=10 r_v= 5

Tuomi et al. (1974), using the synchrotron radiation from DESY at Hamburg obtained Laue-case diffraction topographs in silicon with rather poor resolution. The poor resolution of their topographs is not only due to the large source size of DESY but it may be ascribed partly to the use of Kodak R film rather than nuclear emulsion plates and partly to the fact that the diffracted beams did not pass normally through the film. As it was pointed out in section (3-1) the high order reflections may in certain cases contribute most of the intensity in the image, as was the case of nnn reflections in the topographs of Tuomi et al (1974). In section (2-10) the width of pure edge and screw dislocations were estimated and given by expressions (2-6) and (2-7).

In both cases the width is proportional to the extinction distance ξ. If a small dislocation image width is desired, the conditions should be chosen in such a way that high orders of reflections, which correspond to small values of wavelength are suppressed, because high orders usually result in an increased extinction distance ξ. Hart (1975) took great care to obtain good resolution by using Ilford nuclear emulsion plates, placing the plate normal to the required diffracted beam, and shielding the plate from the scattered radiation. He obtained a resolution of 1-2 μm on the reflection topographs (Schulz mode) of Silicon and LiF. Tanner, Midgley and Safa (1977) avoiding high order reflections, and using L_4 25 μm nuclear emulsions, obtained transmission synchrotron topographs of Silicon and $KCoF_3$ with high resolution comparable to Lang topography.

3.5 Experimental Arrangement

The synchrotron radiation propagates in an evacuated beam-pipe with a beryllium window at the end, which is transparent for X-rays. This window is 47m from the source for the 5 Gev. electron synchrotron NINA at Daresbury. The X-ray beam emerges from a hole typically 5 mm in diameter drilled in a lead block placed in front of the beryllium window of the beam line. It then passes through a slightly wider aperture in a steel plate backed by aluminium which effectively absorbs the scatter and fluorescence from the lead collimator. It is important that this scatter shield does not cut into the main beam defined by the lead aperture otherwise severe scattering and fluorescence is experienced from the scatter shield itself, Tanner, Midgley and Safa (1977).

The experimental arrangement for synchrotron topography is very simple. Due to the almost complete polarization of the beam, the incident plane is chosen to be vertical in order to maximize intensity. Consequently rotation of the specimen about a horizontal axis normal to the beam is sufficient to orient the crystal to the desired Bragg reflecting planes. The laser beam which has been previously aligned with fixed film exposed to the radiation is an extremely useful guide for the exact position of the synchrotron radiation. The specimen can be mounted on a standard X-ray goniometer or on a simple holder which can rotate about a horizontal axis. Then the specimen can be aligned in the laser beam marking the path of the X-ray beam. Conveniently, the specimen orientation could also be determined and adjusted by observing the position of the reflected beam. Great care should be taken that the photographic nuclear emulsion plate is placed normal to the desired diffracted beam, and for symmetrical reflections this can be easily done by placing the plate normal to the reflected laser beam. For all the synchrotron topographic experiments which will be presented in this thesis, Ilford L_4, 25μm thick emulsions were used and processed at reduced temperature inside a domestic refrigerator. The advantages of synchrotron topography can be summarized as follows:

1 - Marked reduction in exposure time for a set of topographs. This reduction in exposure time is two to three orders of magnitude compared with the Lang technique. Several usable topographs are obtained in one exposure.

2 - Achieving a resolution of 1-2μm when the specimen to plate distance is 10-20 cm.

3 - Unlike the Lang technique no critical adjustment and accurately machined traversing parts are needed.

These extremely useful features of synchrotron topography proved that many step-by-step experiments could be performed successfully. For example Bordas, Glazer and Hauser (1975) demonstrated the feasibility of following phase transitions in $BaTiO_3$. At this time the author was very interested in studying the behaviour of antiferromagnetic domain walls in $KNiF_3$ and $KCoF_3$ in magnetic fields. However, because of the geometrical limitations of the Lang technique, it was practically impossible to design an electromagnet and a cryostat capable of fulfilling the requirements. By applying the newly developed synchrotron topography technique, the step-by-step domain wall motion in $KNiF_3$ was observed by Tanner, Safa, Midgley, and Bordas (1976), and since then the author has become involved in synchrotron topographic experiments, particularly, studying controlled domain wall motion in $KCoF_3$ and $KNiF_3$ at temperatures from 4.2°K upwards and in fields up to 14 KOe. Cryogenic X-ray topography using synchrotron radiation will be discussed in detail in Chapter Five.

3.6 Contrast in Synchrotron Topographs

Tanner, Midgley and Safa (1977) observed that the dislocation images in the synchrotron topograph of silicon wedge specimen taken with 5 cm specimen to plate distance show both direct and dynamical images, and several of the direct images show double contrast. Further, the dislocation image widths were very similar to those of Lang topographs, the narrowest

image we could measure being 8μm, in width, from a 220 reflection. The contribution of any other higher order diffraction was very small. The intensities in transmission of the beams diffracted from the {100} planes of $KNiF_3$ crystals with 200 μm thickness are calculated as a function of Bragg angle, at 5 Gev. electron energy and are presented in Fig.(3-3). For these calculations, the expression for the intensity given by Tuomi et al (1974) with an additional factor for film sensitivity from Hart (1975) were used. The structure factors of $KCoF_3$ and $KNiF_3$ for different diffracting planes were calculated and will be presented in the Appendix 1. The values of $P(\lambda)$ for X-ray synchrotron radiation at NINA can be obtained from Fig.(3-1). Fig.(3-4a) shows a 002 Lang transmission topograph of a 200 μm thick (100) plate of $KCoF_3$ crystal, taken with AgKα radiation ($\lambda = 0.56\text{Å}$). Fig. (3-4b) is a synchrotron transmission topograph of the same crystal; where the reflecting planes are of {001} type with the Bragg angle $\theta = 7^{\circ}$, and with a specimen to film distance of 10 cm. In this case, according to the intensity calculations, the basic diffracted beam comes from the (002) planes and the bulk of the intensity arises from X-rays of wavelength 0.5Å. As seen in Fig. (3-4a) and Fig. (3-4b), the contrast and the resolution is very similar in Lang and synchrotron topographs. On a synchrotron topograph, crystal defects can be observed both by extinction and orientation contrast. Orientation contrast is not usually observed in the Lang technique, which uses a collimated characteristic radiation, and the specimen and plate are close together. It is particularly important in synchrotron topographs of crystals containing dislocations, subgrains, twins

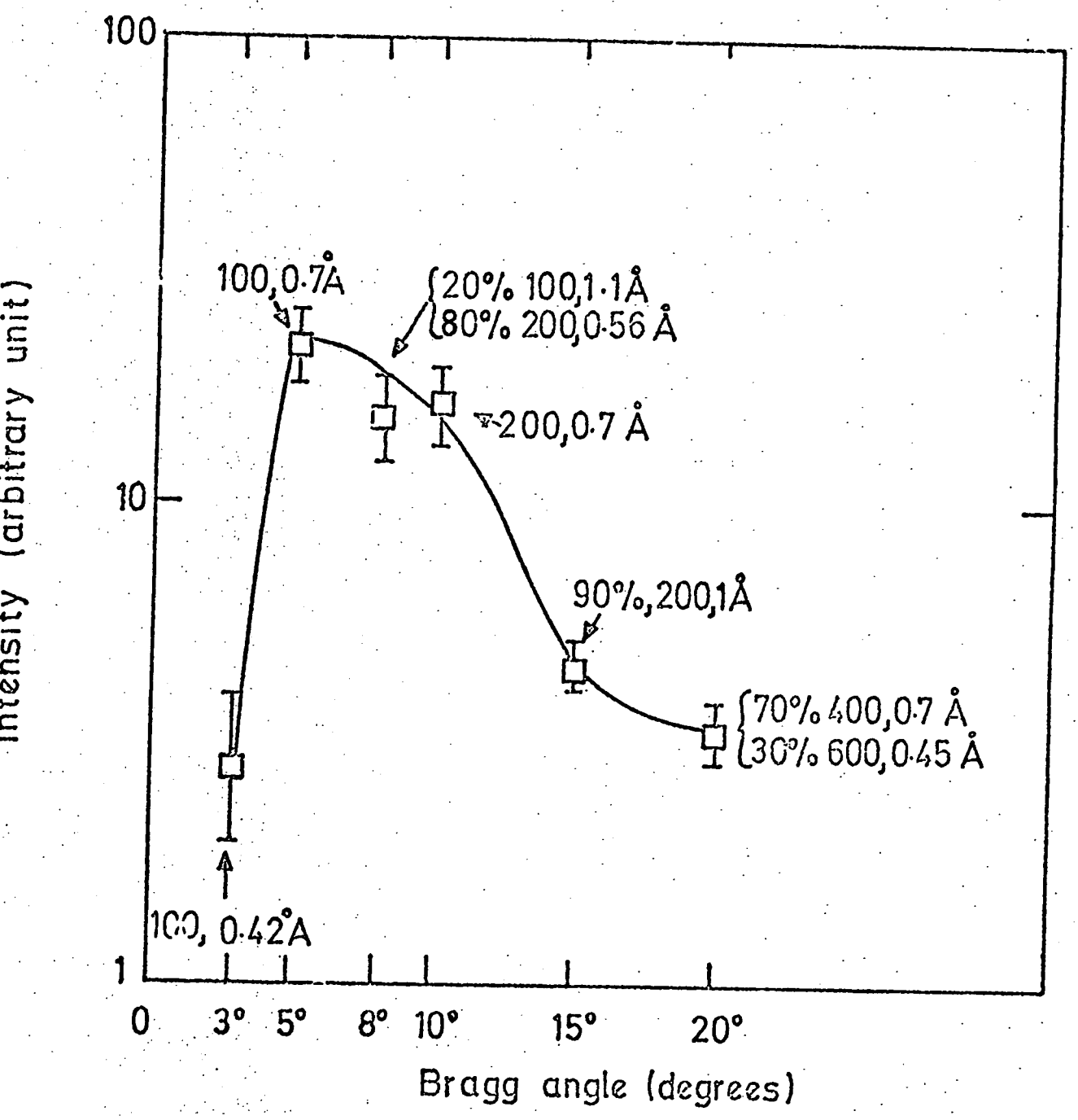

Fig. (3-3) Intensities in transmission of the beams diffracted from {100} planes of $KNiF_3$ as a function of the Bragg angle, using synchrotron radiation at 5 Gev. electron energy.

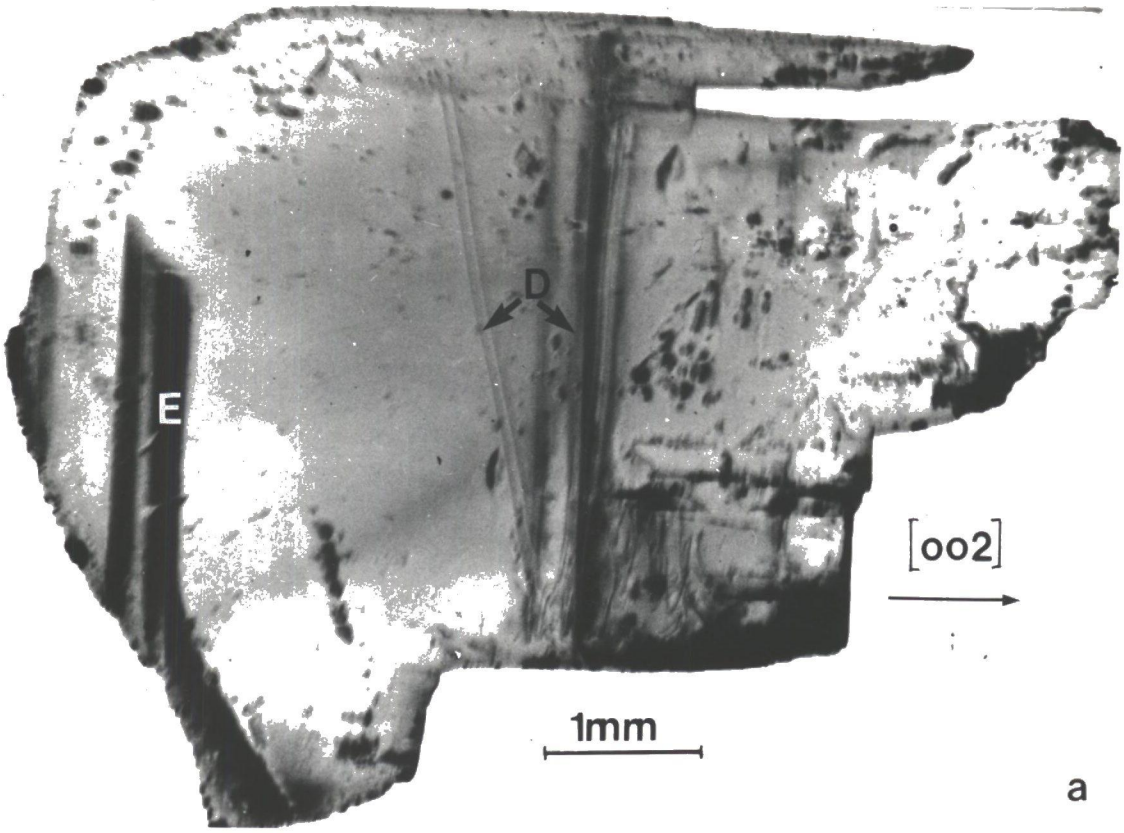

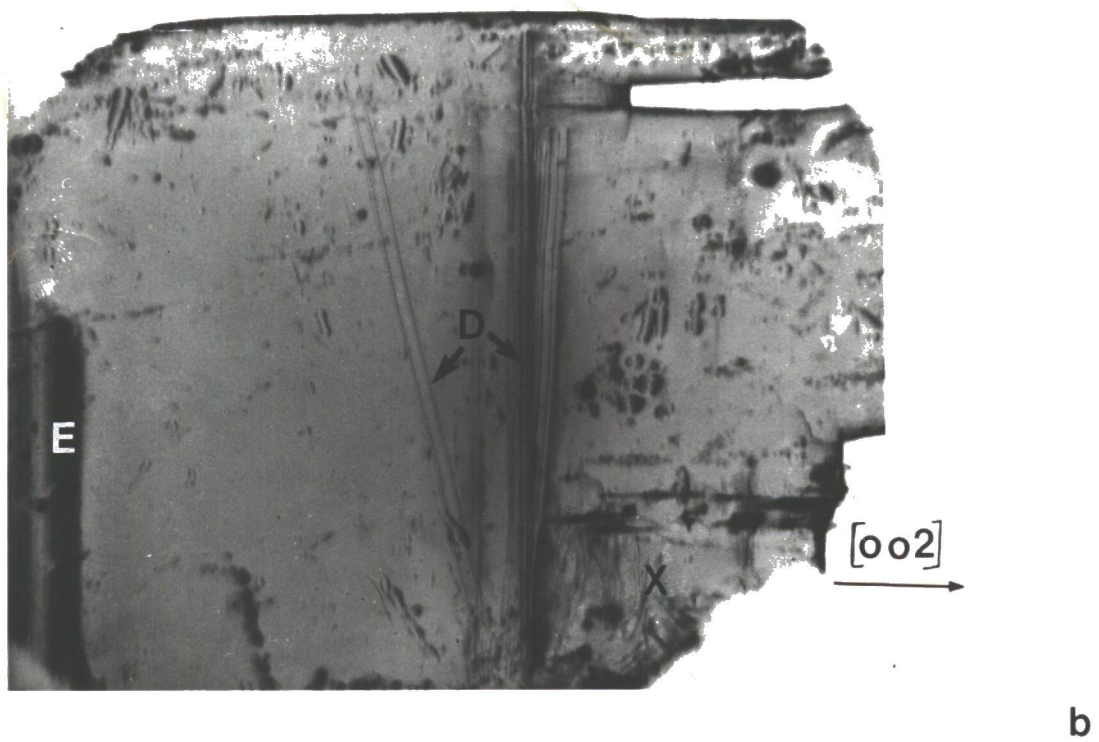

Fig.(3-4) Transmission topographs of a 200μm thick (100) plate of $KCoF_3$ crystal. (a) Lang topograph, 002 reflection, $AgK\alpha_1$ radiation (λ=0.56A), 3h exposure. (b) Synchrotron topograph, mainly 002 reflection, θ_B=7°, 5 Gev, 10mA, 20s exposure, L_4 25μm nuclear emulsion.

and magnetic domains. In the case of orientation contrast, spatial overlap or separation of the diffracted beam from the misoriented regions of the crystal varies with distance, therefore the orientation contrast changes for different specimen to plate distances. This is illustrated in Fig.(3-5) for a dislocation. The mixture of extinction and orientation contrast observed from defects when using synchrotron radiation can lead to difficulties in interpretation. Generally dislocation images in synchrotron topographs are broadened by orientation contrast and in dislocations exhibiting double contrast, the orientation can be seen clearly. Fig.(3-6a) and Fig.(3-6b) are the enlargements of a part of the 002 synchrotron topographs of $KCoF_3$ (Fig.3-4b) which were taken under identical conditions, except that the specimen to film distances were 10 cm and 20 cm respectively. As seen the separation of the maxima in the bimodal profiles of the pair of mixed orientation dislocations in $KCoF_3$ increases as the specimen to film distance increases. The orientation contrast enables the sense of the Burgers vector to be determined. In this case the "intermediary image" formed by new wavefields created beneath the dislocation line, is important, as the intensity profile of dislocations is not symmetrical. Thus all three types of images found in Lang topographs are present in synchrotron topographs.

Streaking of images is a common feature of synchrotron topographs. Using continuous synchrotron radiation, in a continuously bent lattice each point selects its own wavelength for diffraction and hence the Bragg angle varies continuously. Due to the large specimen to plate distance, the

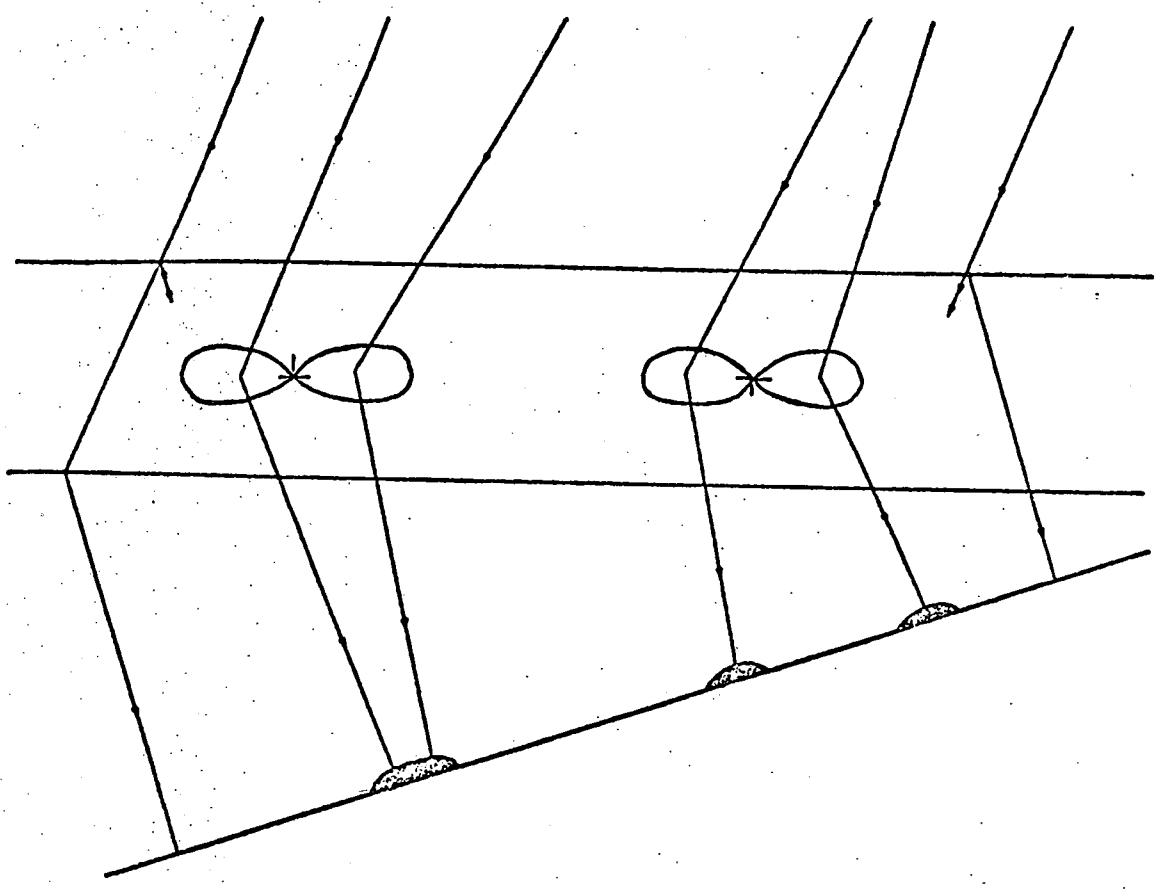

Fig.(3-5) Schematic diagram of the formation of the bimodal direct image.

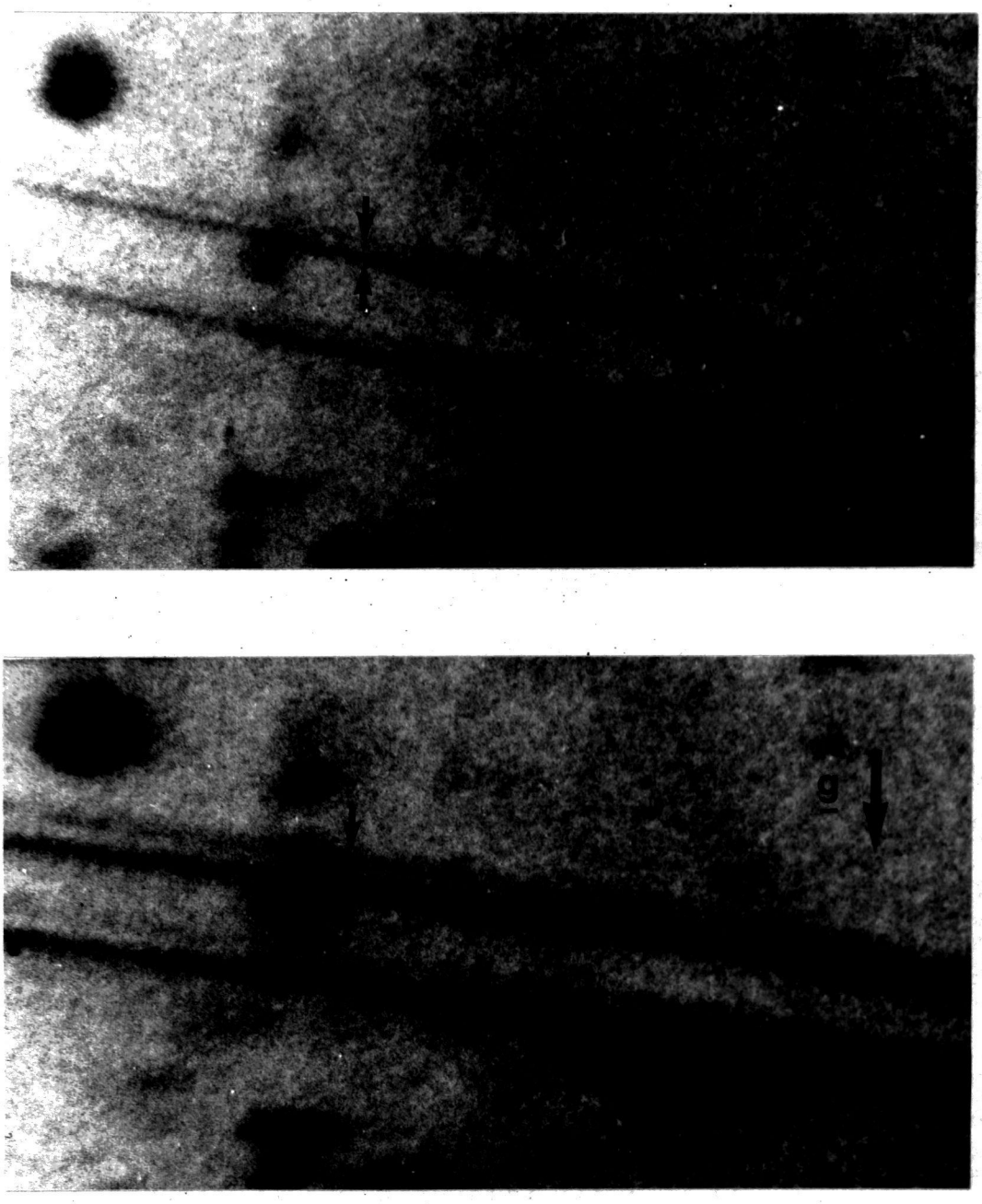

Fig.(3-6) Increase in separation of maxima in bimodal profiles of two dislocations in $KCoF_3$. Specimen to plate distance (a) 10 cm, (b) 20 cm. 7° Bragg angle, mainly 002 reflection. 5 Gev, 10mA, 20s exposure. L4, 25μm nuclear emulsion.

image is smeared out across the film. The streaking is always in the plane of incidence, i.e. perpendicular to the Bragg planes. This effect can be seen in Fig.(3-7) which is a synchrotron topograph of a rectangular crystal of $KCoF_3$ mounted at a corner C with rather a lot of varnish. Because of the glue the lattice planes at this corner bent and caused a large "tail" to develop in the image. Similar streaking is observed at the damaged edges of the specimen, e.g. at E. The direction of the streaking enables the sense of the lattice plane curvature to be determined by inspection. Provided the specimen to plate distance is known, the length of the streak enables the magnitude of the curvature to be estimated.

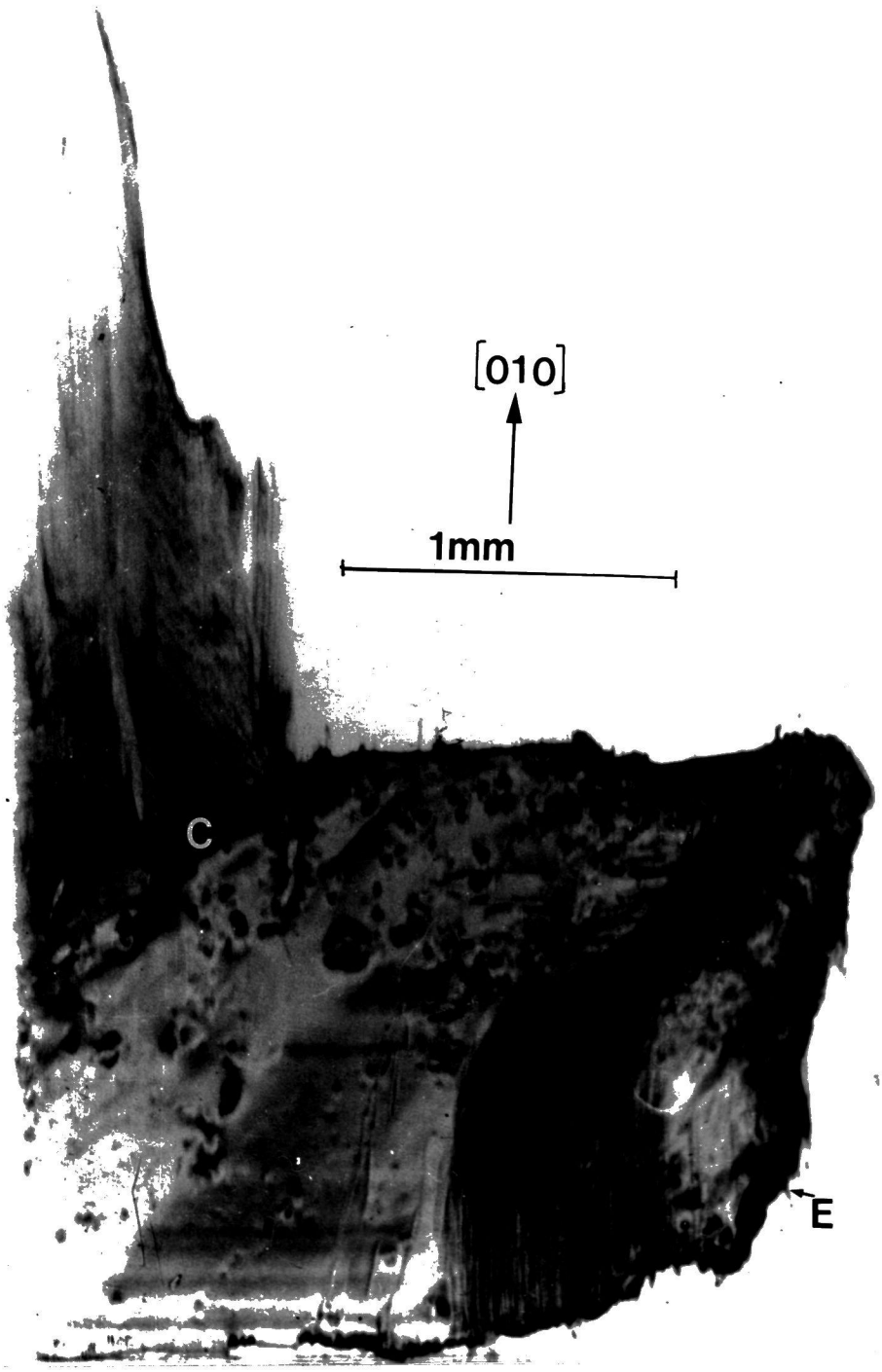

Fig.(3-7) Synchrotron transmission topograph of a $KCoF_3$ crystal bent at one corner. {010} reflecting planes, 5° Bragg angle, 5 Gev, 10mA. 30s exposure, L4 25 μm nuclear emulsion.

CHAPTER FOUR

PERFECTION STUDIES OF KMF_3 (M = Ni, Co, Fe) CRYSTALS GROWN FROM THE FLUX

4.1 Crystal Growth

The crystals were grown from the flux and kindly provided by Mrs. B. W. Wanklyn and Dr. B. J. Garrard at Clarendon Laboratory, Oxford University, and full details of the flux growth of KMF_3 crystals have been reported by Wanklyn et al. (1969, 1975) and Garrard et al. (1974,1975). In the earlier work, KMF_3 crystals were grown from a mixture of MF_2 and KCl, which resulted also in crystals of MF_2. A great degree of intergrowth took place which caused strain and deformation of the crystal. Later, better quality KMF_3 was obtained from compositions in the three-component systems MF_2 - KF-Pb Cl_2, and MF_2 - KF - KCl, from both of which it was possible to obtain KMF_3 in the absence of MF_2. The initial mixture was heated fairly rapidly at 100 to 200 Kh^{-1} to a temperature 50° to 80°C above the estimated liquidus. After melting, with a minimum rate of 2 to 4 Kh^{-1} the temperature of the furnace was decreased. If the rate of cooling was very slow, appreciable oxidation could occur. Also it should be mentioned that the increase in the rate of growth could result in poor optical quality when the crystals were large, or in the production of many small crystals. Therefore when growth takes place in air, a balance has to be struck between a desirably slow growth rate and contamination of the melt by hydrolysis or oxidation during growth. Within these limitations, one in three batches of $KNiF_3$ produced good

crystals; with $KCoF_3$ oxidation occurred more rapidly, and with $KFeF_3$, the crystals were dark brown or black when grown in air. To avoid oxidation, growth was carried out under N_2, using Mo crucibles with Mo or graphite lids since platinum is not an appropriate crucible material under these conditions, Garrard et al.(1974, 1975). The crystals grew firmly attached to the crucible wall or base, and had to be separated mechanically and finally cleaned in dilute HNO_3 when (KF + Pb Cl_2) was used as flux, whereas (KF + KCl) dissolved in water. Transparent crystals were selected for examination with the polarizing microscope. Under immersion oil, the crystals invariably showed strain; some which had only a small area attached to the crucible wall, showed strain only at those edges. The surface of the crystals was somewhat rough with many etch pits. Those provided for topographic assessment were the best in these respects and optical examination showed no special difference between them. The furnace programme, and starting compositions which produced the crystals used for topographic assessment, were kindly provided by Mrs. Wanklyn and are listed in Table (4-1). The topographic results of different batches are also shown in Table (4-1).

4.2 Preparation of Specimens for X-ray Topography

The as-grown cubic crystals were usually a few mm on edge. Fig.(4-1a) shows an as-grown crystal of $KNiF_3$. As the absorption of X-rays in the crystal is considerable, and preferably X-ray topographic studies should be performed when $\mu t < 1$ (μ is the absorption coefficient, and t is the

TABLE(4-1)

Starting compositions, furnace programmes and crystal products

No.	Starting composition	Crucible and capacity cm^3	Rate of heating Kh^{-1}	Max. temperature ^oC	Rate of cooling Kh^{-1}	Notes on Crystals	Topograph	Crystal
I	9.7g NiF_2, 11.6g KF, 38.5g $PbCl_2$, 3.5g NH_4HF_2	Pt, 50	100, to 500° C then 300	900	4, to 350°C, then 100	Small weight loss. Crystals of $KNiF_3$, 5mm on edge.	Figs. (4-2,3,4)	$KNiF_3$
II	12.6g NiF_2, 10.2g KHF_2, 17.9g KCl, 4g NH_4HF_2	Pt, 100	100	960	2, to 820°C, 3, to 580°C Then 50	Small weight loss. Crystals of $KNiF_3$, 4 mm on edges. Strain only present at regions attached to the crucible.	Fig.(4-5)	$KNiF_3$
III	10.7g NiF_2, 12.7g KF 44.6g $PbCl_2$, 3.5g NH_3HF_2	Pt,100	176	960	2, to 760°C 3, to 400°C, then 50.	Small weight loss. Crystals of $KNiF_3$, well separated, about 5 mm on edge.	Fig.(4-6)	$KNiF_3$
IV	9.7g CoF_2, 11.6g KF 38.5g $PbCl_2$, 3.5g NH_4HF_2	Pt,50	100	850	4, to 340°C. Then 100	Small weight loss. Only $KCoF_3$ crystallised, 3 to 4 mm on edge	Fig.(4-7)	$KCoF_3$
V	24g CoF_2, 15g KCl, 2g NH_4HF_2	Mo, 35	100	1050	4, to 400°C. Then 100	Almost all the flux evaporated $KCoF_3$ crystals up to 8 mm on edge and rods of CoF_2 were produced.	Fig. (4-8,9,10)	$KCoF_3$
VI	17.8g FeF_3, 4.2g Fe, 15g KCl, 2g NH_4HF_2	Mo, 35, with graphite lid	100	960	1.5 to 500°C. Then 100	Most of the flux evaporated. $KFeF_2$, about 3 mm on edge, and FeF_2 rods resulted. The The $KFeF_2$ crystals were pale yellow and transparent.	Fig.(4-11)	$KFeF_3$

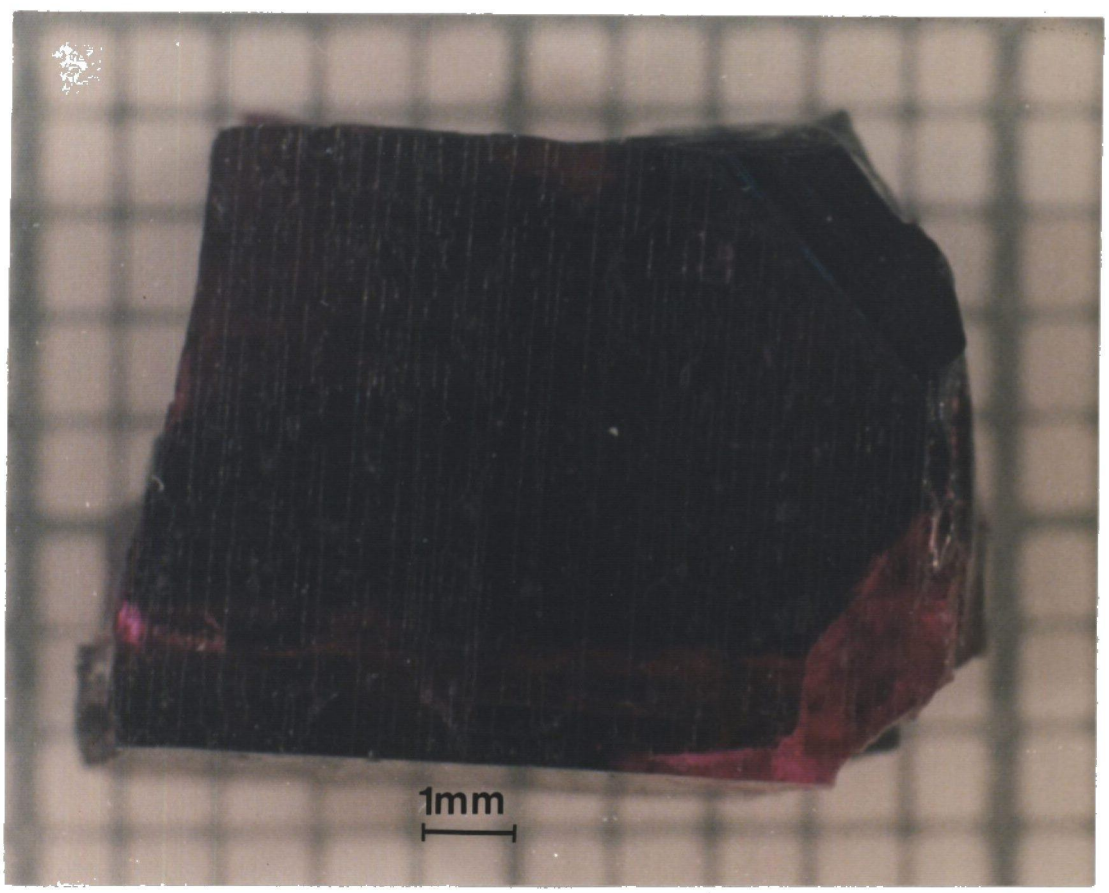

Fig.(4-1b) Photograph of an as grown crystal of $KCoF_3$.

thickness of the specimen), thin plates of crystals should be prepared. The values of absorption coefficient of $KNiF_3$, for Mo $K\alpha_1$, and Ag $K\alpha_1$ radiation are given in Table (4-2) and as seen for a 200 μm thick $KNiF_3$ sample the values of μt can just fulfil X-ray topographic requirements for the "thin crystal" case

TABLE 4-2

The absorption coefficients of $KNiF_3$

Radiation	λ(Å)	μ(cm^{-1})	t(cm)	μt
Mo $K\alpha_1$	0.5608	91	0.02	1.8
Ag $K\alpha_1$	0.7107	47	0.02	0.94

Thin plates, approximately 200 μm thick were prepared by mechanical grinding on silicon carbide paper. As the crystals are fragile and usually break easily along $\langle 100 \rangle$ directions, one should be extremely careful and patient during the grinding. Because of this, it was very difficult to grind the crystals down to a thickness less than 200 μm. Then the polished specimens were etched in HF extensively. Such a procedure left a somewhat irregular surface but one which was, in the main, free from strain. Fig.(4-2) is an optical micrograph of a 200 μm thick oriented plate of $KNiF_3$ crystal from batch I, which was prepared by grinding and extensively etched in HF. As seen, the surface is covered with many etch pits. HF attacks $KFeF_3$ and $KCoF_3$ quickly and etching periods were about one hour, whereas in the case of $KNiF_3$ at least an etching period of one week was required to get rid of surface strain and scratches introduced by polishing!

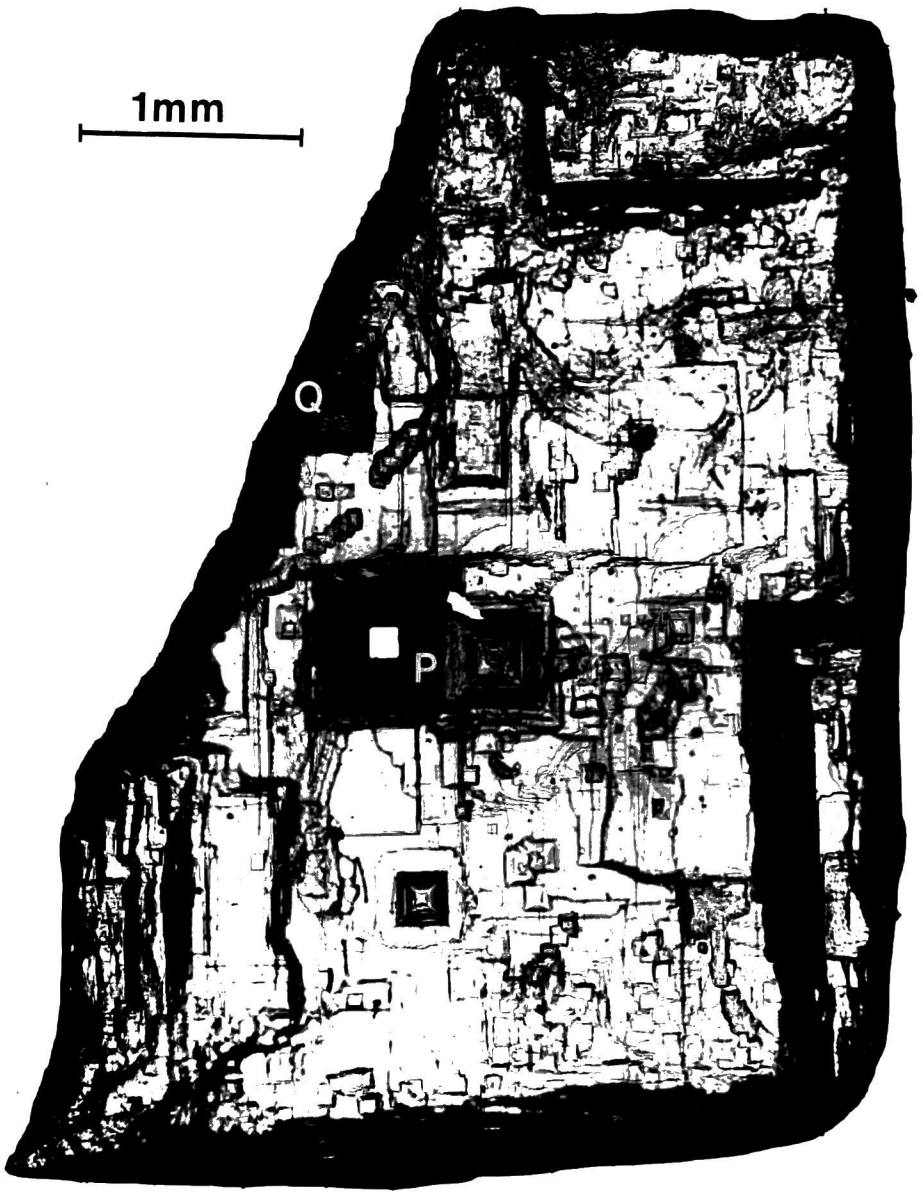

Fig.(4-2) Optical micrograph of $KNiF_3$ crystal from batch I showing well developed etch pits, P. Transmitted light. (100) oriented plate.

4.3 Choice of the Geometry of the Diffracting Planes

The extinction distances of $KNiF_3$ and $KCoF_3$ for different diffraction vectors $\underline{g}$ were calculated and are presented in Table 1 of Appendix I. This table shows that not only some of the reflecting planes such as $\{300\}$ have small structure factors and are not favourable reflections from the viewpoint of intensity but their extinction distances are also long and therefore very wide dislocation images result. As seen in the same table the 200 reflection is an ideal one for X-ray topographic studies of the KMF_3 system. In this case the diffraction is strong (relatively high structure factor), and dislocations resolve well (low extinction distance). For example the extinction distance of $KNiF_3$ 200 reflection $MoK\alpha_1$ radiation, is $\xi_{200} = 20.3\,\mu m$, and using the expressions (2-6) and (2-7), the image widths of screw and edge dislocations are $6.5\,\mu m$, and $11.4\,\mu m$ respectively. In most of the Lang topographic experiments of the present work, 200 reflections using $MoK\alpha_1$ or $AgK\alpha_1$ radiations have been studied, and the images were recorded on Ilford L_4 Nuclear Emulsion of thickness $50\,\mu m$.

4.4 X-Ray Topographic Observations of $KNiF_3$

Fig.(4-3) shows the X-ray topograph of the same crystal as shown in Fig.(4-2). As seen in Fig.(4-3) there is a dislocation L linking two well developed etch pits at P and Q. This dislocation completely disappears in the $0\bar{1}1$ reflection and it is concluded that it is of mixed character, having a large edge component. According to the Burgers vector analysis of mixed dislocations in $KNiF_3$ and $KCoF_3$ which will be

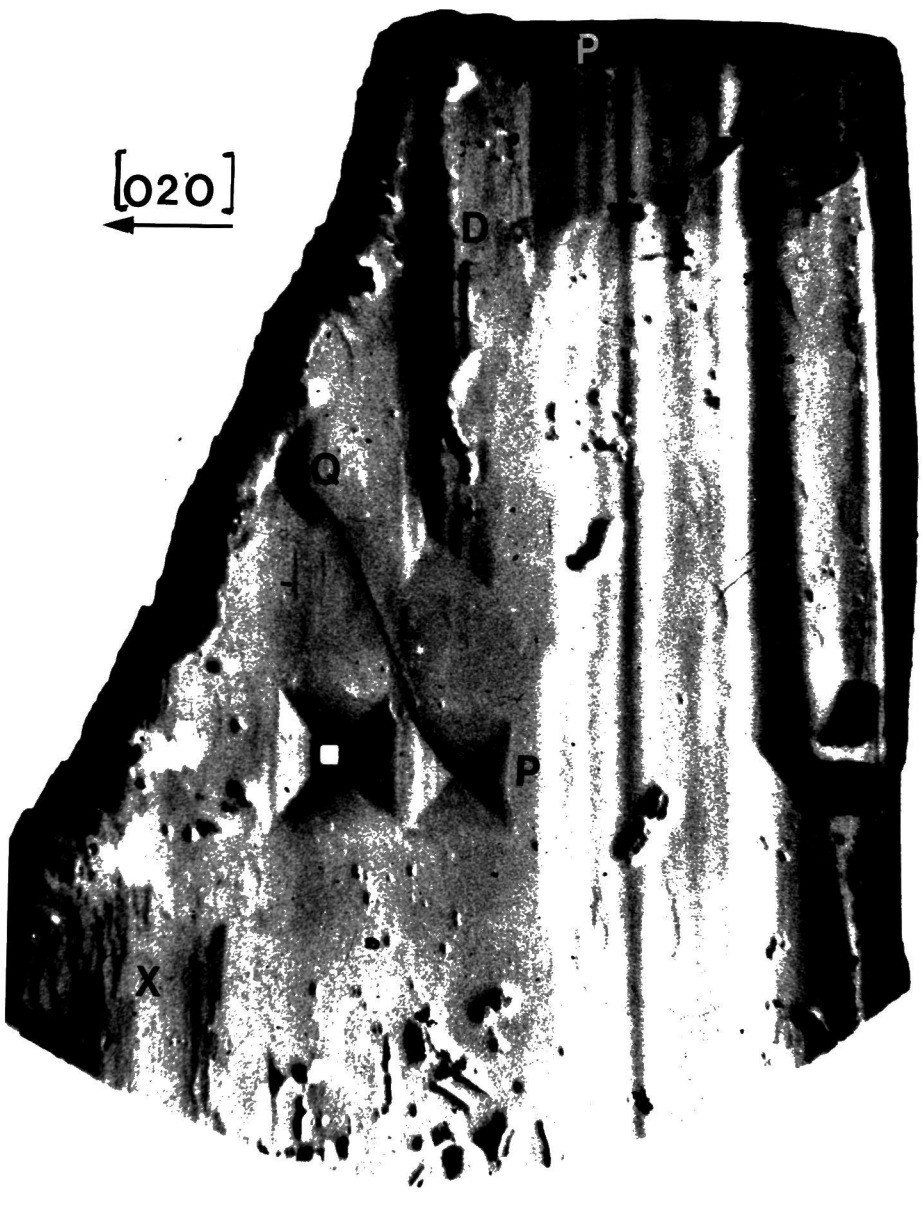

Fig.(4-3) X-ray topograph of the same crystal. 020 reflection Mo$K\alpha_1$ radiation. μt=1.8, L4, 50μm nuclear emulsion.

discussed in section (4-7) the line direction of this dislocation is consistent with a Burgers vector [011] . It seems that the bundle of dislocations marked D in Fig.(4-3), was generated by plastic deformation and it was not possible to determine the Burgers vector. The position of etch pits in Fig.(4-2) and Fig.(4-3) shows that only some of the etch pits like P and Q correspond to dislocation out-crops. The large etch pit P has developed to such an extent that a hole has been punched right through the specimen. Pendellösung fringes are usually seen in highly perfect crystals and their presence on the sloping sides of the etch pits and at the tapering edge of the crystal is interesting as it indicates high lattice perfection.

The growth history of crystals can be studied by X-ray topography, and growth band studies are valuable in tracing the morphology of the crystal throughout its growth history. The growth bands seen in X-ray topographs arise from fluctuation in the lattice parameter during crystal growth. Such changes may be produced during growth by variations in temperature which result in changes in the pattern of convective flow in the melt adjacent to the crystal surface. This results in very small changes in composition in the deposited layers of the crystal probably with ions of the flux incorporated substitutionally in the lattice. The crystal shown in Figs.(4-2) and (4-3) exhibits relatively weak growth striations, indicating that growth was quite uniform. In all crystals examined, the growth bands were parallel to $\langle 100 \rangle$ directions, though in Fig.(4-3) the growth bands are not perfectly straight. This shows that the growth face

was not exactly planar throughout the growth history. The topographs do not, however, give any indication as to the cause of this stepped growth. It seems that most of the other features correspond to mechanical damage introduced into the surface by handling. The faint wavy lines in the region X correspond to steps on the specimen surface. This particular crystal was the most highly perfect specimen found from batch I and has been used extensively for antiferromagnetic domain studies. The high perfection has enabled antiferromagnetic domain wall motion in magnetic fields up to 13KOe at low temperatures down to 4.2 K.

While batch I was of clearly superior quality to other batches, it would be incorrect to present the impression that all crystals in batch I were of comparable perfection to that shown in Figs.(4-2) and (4-3). In most crystals, the growth bands were much more pronounced, indicating that the lattice parameter variations within the crystal were much larger.

An example of a strongly banded crystal from batch I is given in Fig.(4-4). Again the surface of the specimen was very rough and some etch pits have developed right through the specimen. Around them, and the specimen edges, Pendellösung fringes are observed delineating contours of equal thickness. The crystal was of cubic habit, of side 4 mm, and from the growth band observations one can conclude that at all times growth occurred at the equal speeds on the $\{100\}$ faces. Nucleation occurred in the top right hand corner. As expected, the growth bands became invisible when $\underline{g}.\underline{f} = o$, $\underline{f}$ being a vector normal to the growth face.

Contrast arises from the boundary between the two growth sectors A and B observed in Figs.(4-4b)and (4-4c) but not in Fig. (4-4a). The straightness of the growth sector boundary is a good measure of the variation in growth velocity in the two sectors. When the diffraction vector is parallel to the growth sector boundary, no contrast is observed from it, and this is in agreement with the model of the lattice distortions at a growth sector boundary proposed by Bonse (1965) and Fishman and Lutsau (1970). While Parpia (1976) has proposed a model to account for the sector boundary contrast in synthetic quartz, with the present observations one can not determine whether Parpia's model is applicable here.

As is evident in Fig.(4-4), the dislocation density is low and three types of dislocations were identified. Dislocations D_1, form a pair running normal to the growth face in sector B. They are invisible in the 020 reflection (Fig.(4-4c) and also in the 110 reflection (not shown). The Burgers vector is therefore parallel to [001] and as the shortest lattice translation in this direction in the perovskite structure is [001] , therefore for these dislocations $\underline{b} = \pm [001]$. They are therefore pure screw dislocations and as seen they exhibit some waviness, which can be attributed to climb occurring while the crystal was at elevated temperature. The dislocations D_2 also run normal to the growth front and are also invisible in the 020 reflection Fig.(4-4c) and 110 reflection. These dislocations also have $\underline{b} = \pm [001]$ and are of pure edge type. It is interesting to note that no marked change in growth velocity occurred upon nucleation of the screw dislocation D_1, though with only

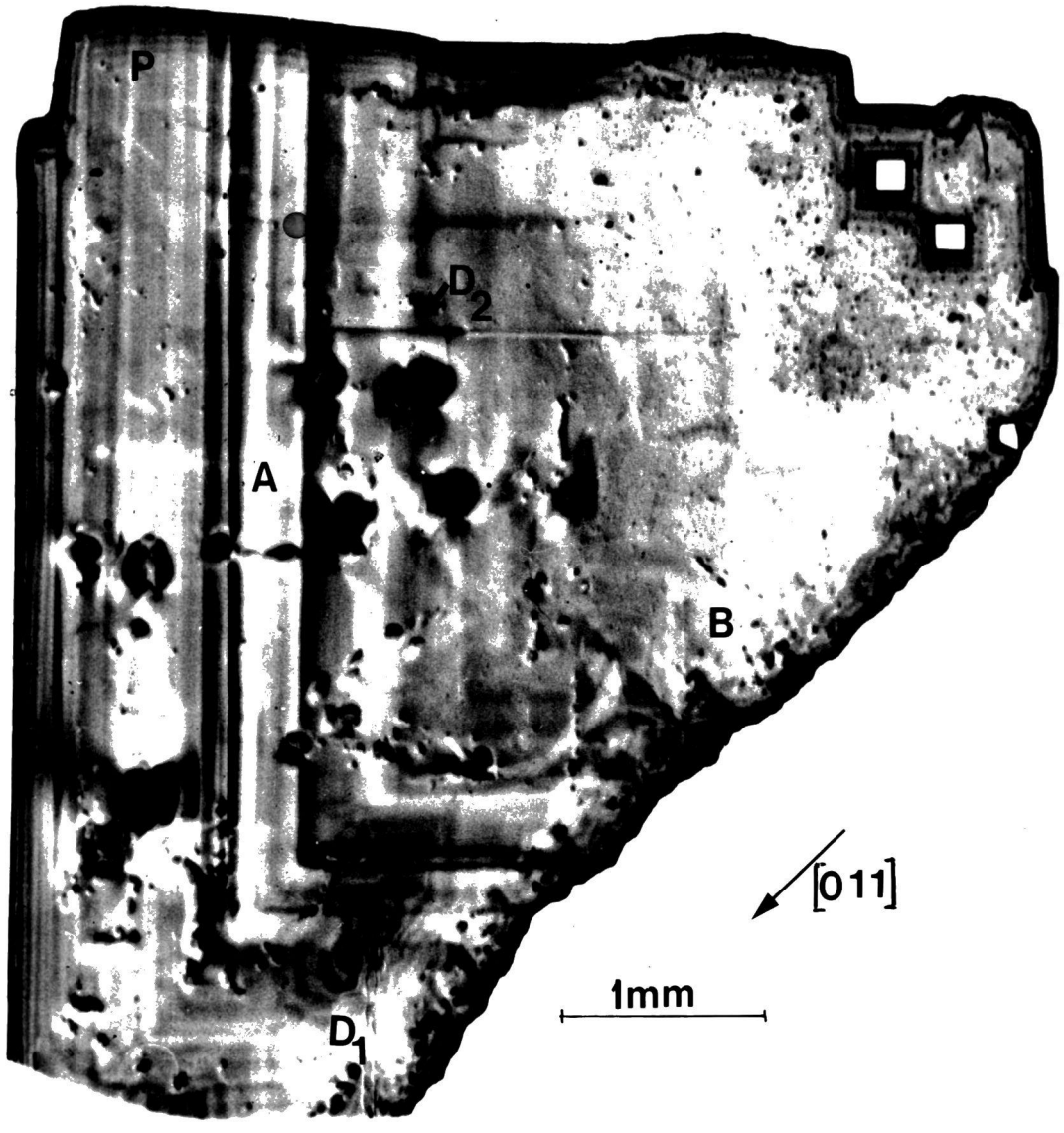

Fig.(4-4a)

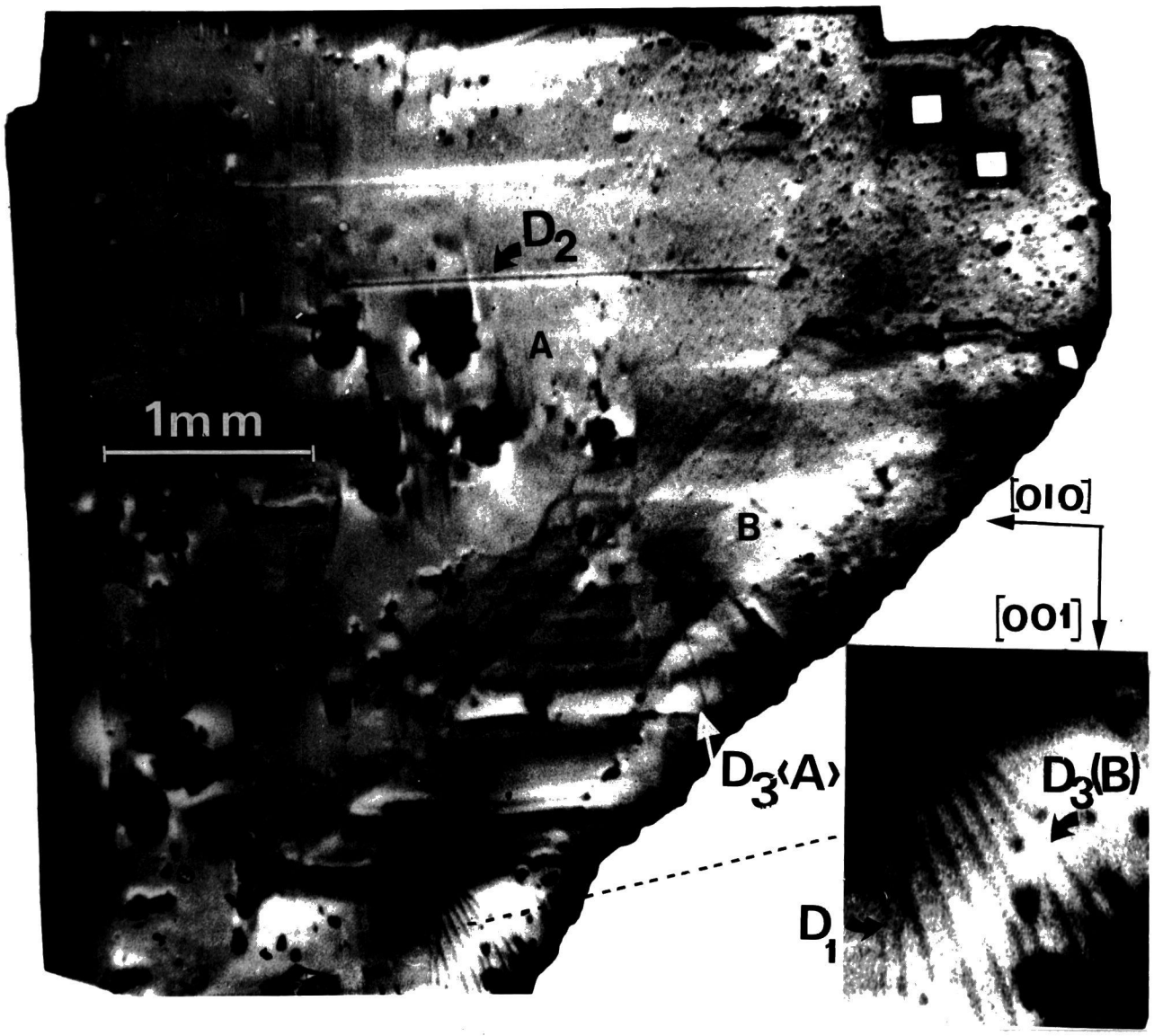

Fig.(4 - 4b)

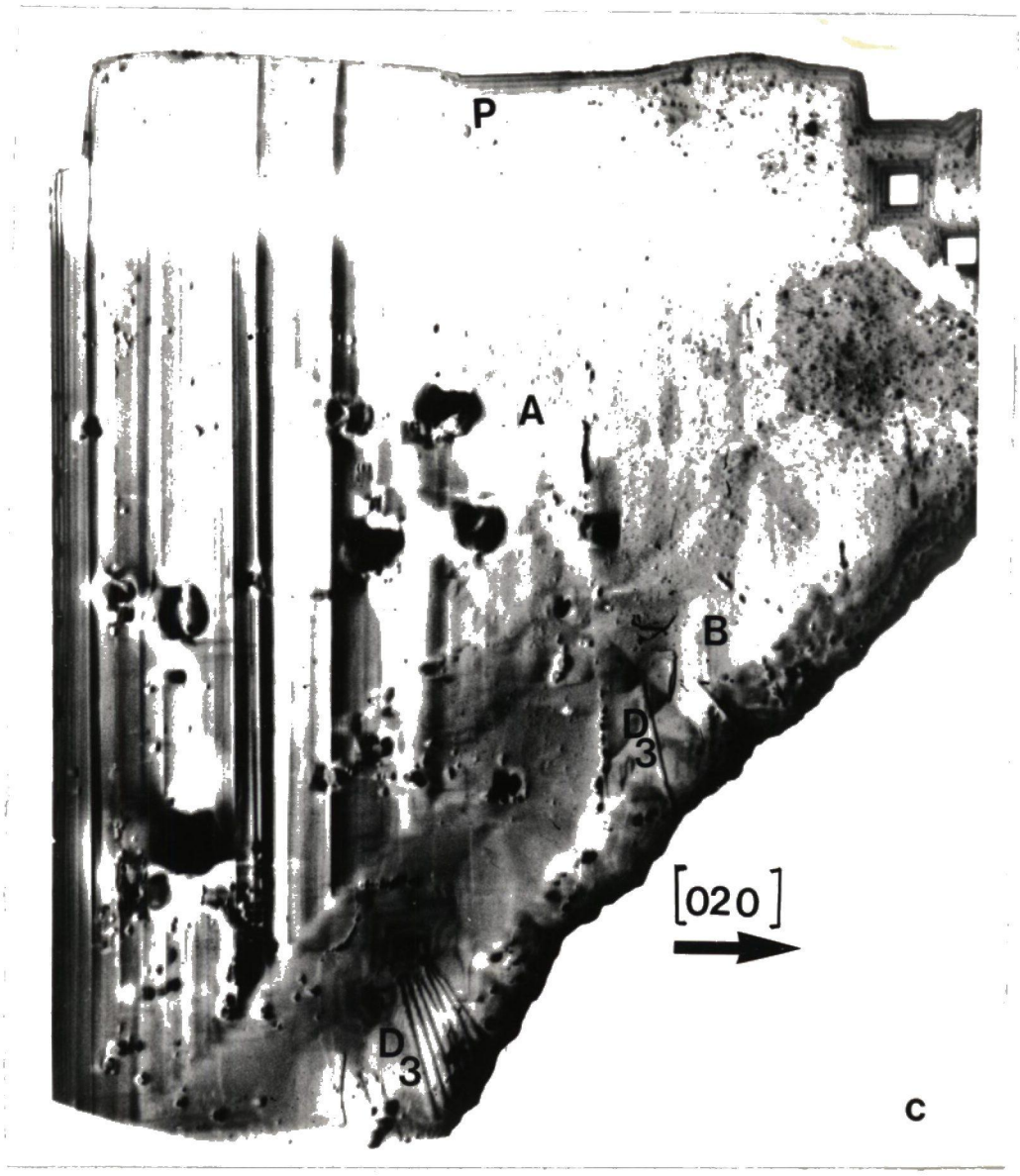

Fig.(4-4) Topographs of another crystal from batch I. Pendellosung fringes P indicate high perfection, Mo$K\alpha_1$, L4 50μm nuclear emulsion.

(a) 011 reflection. Growth bands in both sectors A and B visible. Sector boundary invisible. Dislocations D_3 invisible.

(b) 002 reflection. Bands in sector A invisible.

(c) 020 reflection. Bands in sector B invisible. Dislocations D_1 and D_2 invisible.

a thin section being examined it is possible that screw dislocations were already present at the growth front. The dislocations D_2 might be expected to exist in pairs, as do dislocations D_1, but one of the dislocations may have been lost in polishing the 200 μm thick plate. The dislocations D_3 vanish only in 011 reflection and it is concluded that $\underline{b} = \pm [0\bar{1}1]$. This particular crystal plate is of considerable interest as it exhibits in a flux-grown crystal many features characteristic of solution growth and as we will see in section (4-7) the directions of these dislocations are in agreement with the postulate that dislocations in solution-grown crystals run in such a direction as to minimize their elastic line energy per unit length of growth.

The early topographic studies of the crystals from the batch I revealed high dislocation densities which were mainly due to the plstic deformation.

Fig.(4-5) shows a topograph of a(110) slice of a crystal from batch II. As in all crystals examined from this batch, strong growth band contrast is observed. Many dislocation lines can be identified in the right hand part of the topograph. This observation is supported by the high density of etch pits found on the surface, and the general perfection of this batch was inferior to batch I. However, the strong growth bands observed in the (110) slice confirmed that growth occurred on the three $\{100\}$ faces at equal rates throughout growth.

Fig.(4-6) illustrates the typical product of batch III. The dislocation density is high and individual defects cannot

Fig.(4-5) Topograph of (110) plate of $KNiF_3$ crystal from batch II. $1\bar{1}0$ reflection $MoK\alpha_1$ radiation, L4 50μm nuclear emulsion.

Fig.(4-6) Much less perfect crystal from batch III. High dislocation density. 020 reflection, AgKα_1 radiation, L4 50μm nuclear emulsion.

be clearly resolved. The dislocations do not lie along crystallographic directions and are not straight. It seems that they arose from slip at high temperature.

Although the best crystals of $KNiF_3$ were obtained from batch I, and were grown using a $PbCl_2$ flux, there did not appear to be a significant correlation between crystal perfection and the flux composition as the crystals of batch III were inferior to those of batch II.

4.5 X-Ray Topographic Observations of $KCoF_3$

Fig.(4-7) shows the topograph of a 200 μm section of a crystal of $KCoF_3$ from batch IV. In the lower section, the dislocation density is high but in the upper left hand corner it is free from defects. The growth banding is quite strong, as in $KNiF_3$, indicating that growth took place on the $\{100\}$ faces throughout growth. Several dislocations D are visible which are clearly grown in and are of $[011]$ Burgers vector and as seen in Table (5-4) their direction is in excellent agreement with the theoretical prediction. The dislocations E are curved and as in the $KNiF_3$ crystal shown in Fig.(4-6) one may suggest that they arose from plastic deformation during growth.

The best as-grown $KCoF_3$ crystal in batch V is shown in Fig.(4-1b). The whole crystal was cubic of 8mm edge, and it was cut into three sections, and each section was prepared by mechanical grinding and then etching in HF.

The first section is shown in Fig.(4-8). As seen the growth bands are in $[001]$ direction and the pure screw dislocations d run normal to the growth bands. In the region X

Fig.(4-7) $KCoF_3$ crystal from batch IV. High dislocation density in the lower region but much more perfect region above. A few growth dislocation D identifiable. 020 reflection, MoKα_1 radiation L4 50μm emulsion.

a tangle of dislocations which can be attributed to plastic deformation is observed. The other features may be due to the surface damage.

The centre section is shown in Fig.(4-9). Although the growth banding is very strong, indicating a large change in lattice parameter during the course of growth, the dislocation density is very low. In the left hand region X of the micrograph evidence of plastic deformation is seen in the tangle of dislocation lines. Inspection of a photograph of the crystal <u>in situ</u> before removal from the crucible (Garrard, Wanklyn, and Smith (1974)) revealed that the plastic deformation occurred in a region where substantial intergrowth had taken place. Reference to the growth bands shows that this region was that which was first to grow. Fig.(4-8) also shows a similar dislocation tangle in the corresponding position X in the adjacent slice.

It is interesting to note that this crystal did not always grow at equal rates on all $\{100\}$ faces.

As in $KNiF_3$ there are several long straight dislocations typical of solution-grown crystals. In Fig.(4-9a) dislocations D_1 and D_3 are visible; D_1 being pure screw in character with Burgers vector $[010]$ while D_3 are of mixed character and of Burgers vectors $[011]$, these being completely invisible in the $[0\bar{1}1]$ reflection. In Fig.(4-9b) another set of dislocations D_2 are invisible and are of pure edge character and Burgers vector $[001]$. As we will see in section (4-7) and Table (5-4) the direction of these dislocations are in good agreement with the minimum elastic energy principle.

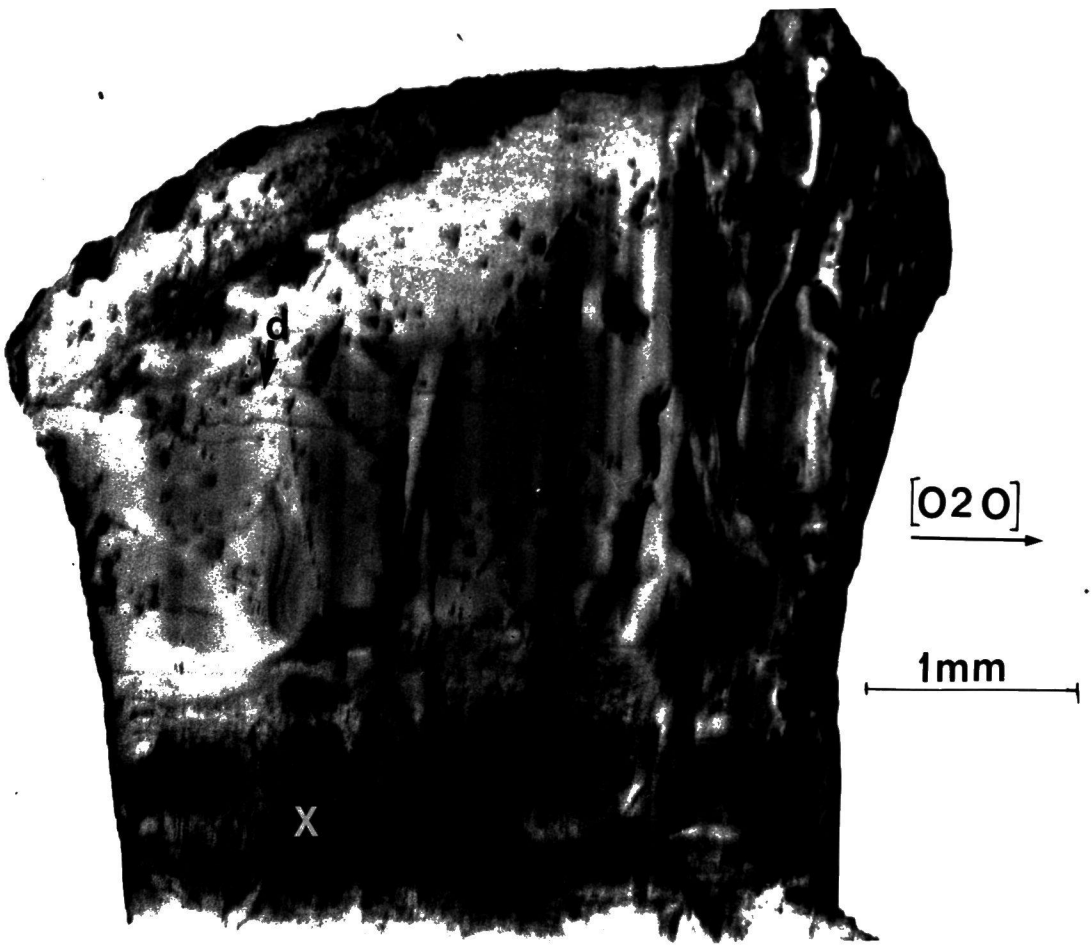

Fig.(4-8) First slice of the best $KCoF_3$ crystal from batch V. Growth bands in contrast in [001] direction. Dislocations d visible. 020 reflection, $AgK\alpha_1$ L4 50μm emulsion.

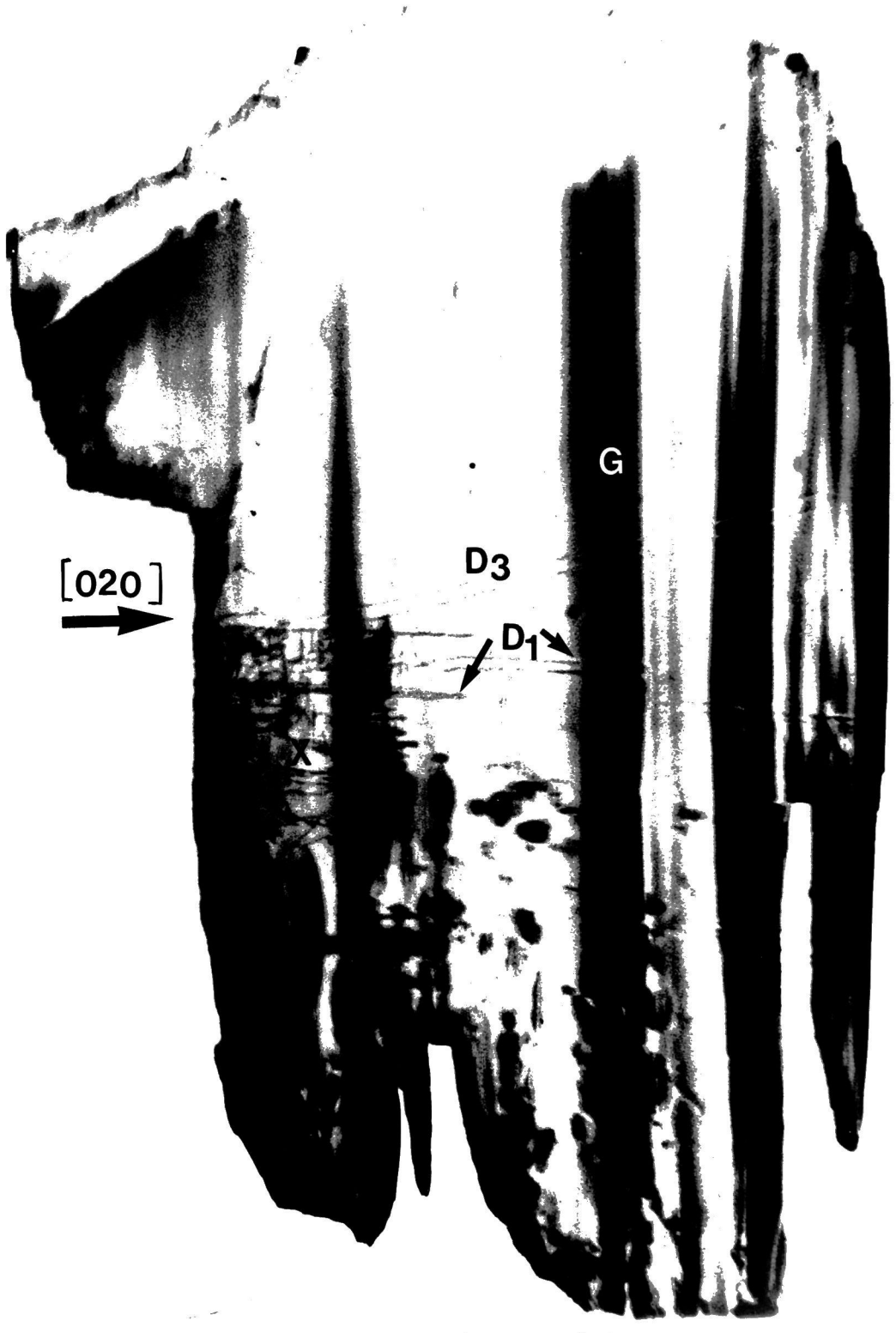

Fig.(4-9) The centre section of the best $KCoF_3$ crystal from batch V.

(a) 020 reflection, $AgK\alpha_1$ radiation. Dislocations D_1 and D_3 in contrast. Growth bands G in contrast.

Fig.(4-9) (b) 002 synchrotron topograph, 7° Bragg angle, now dislocations D_2 are visible, growth bands G invisible.

Fig.(4-10) The third slice of the best $KCoF_3$ crystal from batch V. 020 reflection, $AgK\alpha_1$, $\mu t \simeq 4$, L4 50μm nuclear emulsion.

Fig.(4-10) shows a Lang topograph of the third slice of $KCoF_3$ crystal from batch V. This slice was rather thick ($t = 800\,\mu m$) and for $AgK\alpha_1$ radiation $\mu t \simeq 4$. Although it is difficult to interpret all the contrast in this absorption condition, surface features appeared strongly on the topograph. In Fig.(4-1b) straight lines which can be attributed to cracks on the surface of the as-grown crystal are observed. Although this slice was polished, most of these lines were seen optically. The X-ray topographic contrast also shows several horizontal lines which may be due to small cracks. The vertical black bands are very similar to growth bands, but the contrast is complicated. Baruchel (1973) has also observed similar contrast on an X-ray topograph of $KCoF_3$. In order to reduce the crystal thickness, it was ground mechanically, but due to the presence of cracks in the crystal, it shattered. However one small piece of the crystal (2x3mm) of $300\,\mu m$ was prepared. X-ray topographic observations on this thin plate proved that it was of comparable quality to the first and second slices. No surface features were observed.

4.6 X-Ray Topographic Observations of $KFeF_3$

Fig. (4-11) shows a topograph of a crystal of $KFeF_3$ from batch VI, grown from Koch-Light FeF_3 under similar conditions as (batch V). The quality is clearly inferior to the $KNiF_3$ and $KCoF_3$. Although the contrast is difficult to analyse, it appears that many precipitates exist throughout the crystal, not just at the surface. It is suggested that these are oxide particles incorporated during growth.

Fig.(4-11) Relatively imperfect crystal of $KFeF_3$ from batch VI. $MoK\alpha_1$ radiation 020 reflection.

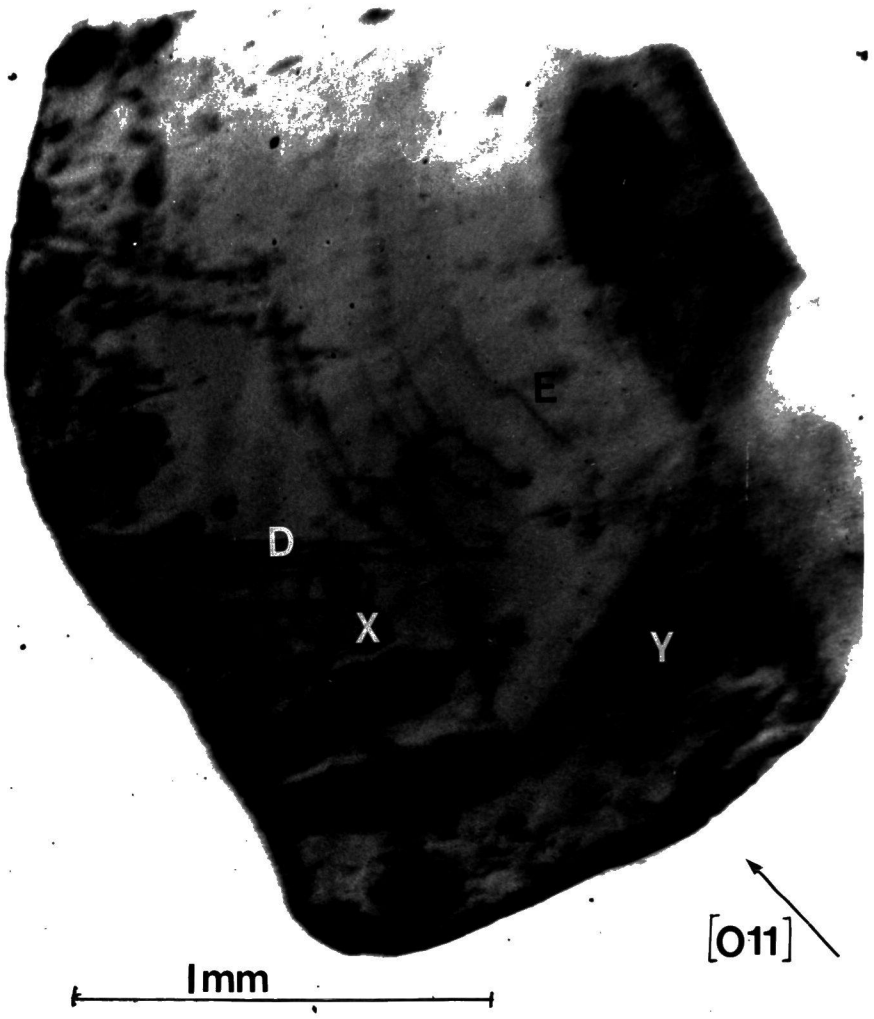

Fig.(4-12) Topograph of the best $KFeF_3$ crystal. A few growth dislocations D and E are seen. 110 reflection, $AgK\alpha_1$ radiation.

Fig.(4-12) shows a topograph of a crystal of $KFeF_3$ grown from Cerac FeF_2 instead of Koch-Light FeF_3. As seen the crystal can be grown with comparable perfection to the other fluorides. The dislocation D runs normal to [001] and the dislocations E are of mixed orientation. The directions of these dislocations are similar to those seen in $KNiF_3$ and $KCoF_3$. The dislocations in the regions X and Y were presumably generated by plastic deformation.

4.7 The Direction of Dislocations in Flux-Grown Crystals

An extensive series of experiments by Klapper (1972, 1973), and Klapper and Küppers (1973, 1974) on crystals grown from aqueous solution have revealed that the dislocation configurations may be interpreted using a single hypothesis. If it is assumed that the crystal grows in such a way as to minimise its free energy, it follows that dislocation lines preferentially run in those directions which minimise their elastic line energy per unit growth length. This condition is also equivalent to the dislocation line experiencing zero force due to the growth surface. Klapper and his coworkers have calculated the line energy $E\ (\underline{b},\ \underline{l},\ C_{ij})$ of dislocations in crystals using anisotropic elasticity theory. The energy may be written

$$E\ (\underline{b},\underline{l},C_{ij}) = K\ (\underline{b},\underline{l},C_{ij})b^2.\ \ln(R/r)/4\pi \qquad 4\text{-}1$$

where K is the energy factor, R and r the outer and inner cut off radii of the dislocation, $\underline{b}$ the Burgers vector, $\underline{l}$ the line direction and C_{ij} the elastic constants.

The energy per unit growth length is then

$$W\ (\underline{b},\underline{l},C_{ij},\underline{n}) = E(\underline{b},\underline{l},C_{ij})/\cos\alpha \qquad 4\text{-}2$$

where $\underline{n}$ is the normal to the growth face and $\alpha(\underline{n},\underline{l})$ is the angle between $\underline{n}$ and $\underline{l}$. The theory gives very good agreement between theoretically preferred directions and dislocation line directions observed by X-ray topography in a wide range of aqueous solution grown crystals. Epelboin et al. (1973) have also found that the theory was applicable to hydrothermal growth, and the agreement between the theory and their X-ray topographic observations was quite good. In order to test the theory in high temperature flux-grown $KNiF_3$ and $KCoF_3$ crystals, Dr. H. Klapper kindly computed the preferred dislocation directions and as seen in Tables (4-3) and (4-4) the agreement between the present X-ray topographic observations and the theory is excellent. This work will be reported by Safa, Tanner, Wanklyn and Klapper (1977).

In the case of $KNiF_3$ Table (4-3) shows that the dislocation lines $\underline{l}$ in Fig.(4-4) obey the three general rules formulated by Klapper and Küppers (1973, 1974). These are:

1. For Burgers vector $\underline{b}$ parallel to $\underline{n}$, $\underline{l}$ is parallel to $\underline{n}$ (screw dislocations D_1).
2. For $\underline{b}$ normal to $\underline{n}$ and $\underline{n}$ parallel to a direction of two-fold symmetry, $\underline{l}$ is parallel to $\underline{n}$ (edge dislocations D_2).
3. For $\underline{b}$ neither parallel nor normal to $\underline{n}$, $\underline{l}$ lies between $\underline{n}$ and $\underline{b}$ (mixed dislocation D_3).

Using values of elastic constants taken from Rousseau, Nouet and Zarembowitch (1974) the variation of the elastic line energy per unit growth length W was computed as a function of orientation. As seen in Table (4-3), the theoretical preferred directions of dislocations D_1 and D_2 lie normal to the respective growth fronts as expected on symmetry grounds.

Agreement for these dislocations is excellent. For dislocation D_3, the theoretically preferred direction makes an angle of 12° to [001] in the (100) plane and the direction of the isolated dislocations, e.g. dislocation D_3(A), is in excellent agreement with the theoretical prediction. The agreement for the bundle of dislocations D_3(B) is not so good but it should be noted that the curvature of the energy surface is very small and the variation in elastic line energy per unit growth length between an angle of 12° and 20° is only 1%. In such a case other influences may become important, for example, the mutual elastic interaction within the dislocation bundle or with the strain fields of growth bands. This may push the dislocations apart, thus increasing the angle of the fan around the mean angle of about 17°. It should also be noted that the angular spread of the fan decreases when the dislocation lines D_3(B) propagate from their origin in the growth band producing strong X-ray topographic contrast. Here their orientation approaches the calculated direction.

TABLE 4-3

Observed and Theoretical Preferred Line Directions in $KNiF_3$

Dislocation	Growth Sector	$\underline{b}$	Angle made with [001] in (100) plane	
			Observed	Theoretical
D_1	(001)	[001]	0°	0°
D_2	(010)	[001]	90°	90°
D_3	(001)	$[0\bar{1}1]$	13°±0.5° for A 15-30 for B	12°

Similar computations were performed to determine the preferred line directions of dislocations in $KCoF_3$ crystals grown from flux.

Table (4-4) shows that there is excellent agreement between the theoretical and observed directions of dislocations in three different crystals of $KCoF_3$.

TABLE 4-4

Observed and the Theoretical Preferred Line Directions in $KCoF_3$

Dislocation	Growth Sector	$\underline{b}$	Angle made with 010 in (100) plane	
			Observed	Theoretical
D_1, Fig(4-9)	(010)	[010]	$4^\circ \pm 0.5^\circ$	0°
D_2, Fig(4-9)	(010)	[001]	$0^\circ \pm 0.5^\circ$ for D_2(A) $0\text{-}5^\circ$ for D_2(B)	0°
D_3, Fig(4-9)	(010)	[011]	$13^\circ \ddagger 0.5^\circ$	16°
d, Fig(4-8)	(010)	[010]	0°	0°
D, Fig(4-7)	(010)	[011]	13° - 14°	16°

Calculations show that the energy minimum is quite sharp for the screw dislocations D_1 and d but rather flat for the edge dislocations D_2. The energy minimum of mixed dislocations D_3 and D is also shallow, the variation in W between 12° and 20° with [010] is only 0.3%.

Although the values of elastic constants used were necessarily room temperature values, the agreement between the observed and theoretically preferred line directions is excellent. The small discrepancies probably arise more from mutual elastic interactions between dislocations than from the inaccuracy

in values of the elastic constants. Although changes in the absolute values between 20°C and 900°C might be expected, the relative values are not expected to vary very much.

The present work has demonstrated that a concept originally formulated in relation to growth from aqueous solution at room temperature can be applied successfully to solution growth from molten salts at high temperatures. When plastic deformation or dislocation climb does not mask the intrinsic features, the dislocation configuration in flux-grown crystals can be understood in terms of one very simple principle.

CHAPTER FIVE

CRYOGENIC X-RAY TOPOGRAPHY

5.1 Review of the Low Temperature X-ray Topographic Experiments

Despite the considerable interest which exists regarding room temperature X-ray topographic experiments, very few low temperature topographic studies have been performed. As X-ray topography is a very powerful technique for domain observations in the bulk of the specimen, and many materials become magnetic or antiferromagnetic at low temperatures, the development of cryogenic X-ray topography is extremely important.

The first low temperature X-ray topographic experiment was performed by Saito, Nakahigashi, and Shimomura (1966) to observe antiferromagnetic domains in CoO by the Berg-Barrett technique. They used a liquid air cryostat in which a goniometer with a copper specimen holder was attached to the bottom of the metal container for liquid air. The specimen was glued to the copper holder, so that it was cooled by thermal conduction through the goniometer. The specimen was enclosed by a plastic cover which is transparent for X-rays as well as for visible light. The specimen chamber thus formed, was connected directly to a vacuum space for heat insulation in the cryostat. Under usual conditions, the specimen temperature was estimated to be about 123 K. Hosoya and Ando (1971 and 1972) using a liquid nitrogen cryostat studied antiferromagnetic domains in Cr by X-ray and neutron topography respectively. Schlenker, Baruchel and Nouet (1973) using a liquid nitrogen cryostat especially designed for X-ray transmission topography observed domains in $KCoF_3$. In the liquid

helium range, MERIC have manufactured a variable temperature cryostat specially designed for Lang topography. The details of this cryostat will be discussed in section (5-3). Mathiot, Petroff and Bernard (1973); Petroff and Mathiot (1974); Mathiot and Petroff (1975) used this cryostat for Lang X-ray topographic studies of magnetic domains in terbium iron garnet at temperatures down to 4.2 K, and we have also performed topographic experiments at temperatures down to 4.2 K with this cryostat.

The author has been involved in the design of three different cryostats for X-ray topography using Lang and synchrotron techniques. In this chapter the designs of these cryostats and also the one manufactured by MERIC will be described.

5.2 Glass Cryostat with Cold Finger Tail

This cryostat was originally constructed for use with the Lang camera in the liquid nitrogen range and it was designed in collaboration with Mr. D. Midgley.

Fig.(5-1a) shows the cryostat mounted on the Lang camera. Fig. (5-1b) shows the details of the bottom part of the glass cryostat. The dewar itself was made from glass and a glass-to-metal seal carried a copper cold finger E from the nitrogen reservior to the specimen situated about 5 cm below the reservoir. Specimens were mounted on brass holders H capable of crude adjustment about a horizontal axis on two grub screws. As the holder can not be rotated in the vertical plane, the specimen should be mounted carefully in an accurate geometrical position within a degree to satisfy the desired Bragg-

reflection. $KNiF_3$ and $KCoF_3$ have the perovskite cubic structure, and the specimens are prepared as (100) thin plates. These specimen plates usually have well defined [010] or [001] edges, therefore using a set square, one can glue the specimen in the desired position and fulfil the diffraction condition. For low temperature topographic experiments, varnish was used to glue the specimen. A glass cap C fitted with mylar windows W which were fixed with epoxy resin, covered the specimen and ensured a vacuum space round it to minimize heat loss. This vacuum space connected with the dewar space and for this reason the dewar was continuously pumped with a rotary pump during operation. Due to the relatively poor vacuum there was considerable heat loss down the cold finger and the specimen area constituted the weakest part of the design. Consequently, the cryostat has never achieved a temperature of 77 K, and the typical temperatures obtained, were estimated to be about 100 K.

In Lang's method using a conventional generator, the photographic plate must be situated within 1-2 cm of the specimen in order to obtain a geometrical resolution of 1-2 μm. As a result a diffracted beam slit is required in order to eliminate the unwanted direct beam from the photographic plate. As seen in Fig. (5-1a) and Fig. (5-4b), the slit S is located immediately after the cap C and the photographic plate is placed just after the slit. In the case of the glass cryostat, it was possible to place the film within 2 Cm of the specimen. Using this arrangement, domain patterns of $KNiF_3$ were observed with good resolution. It has proved difficult to design cryostats capable of fulfilling these requirements

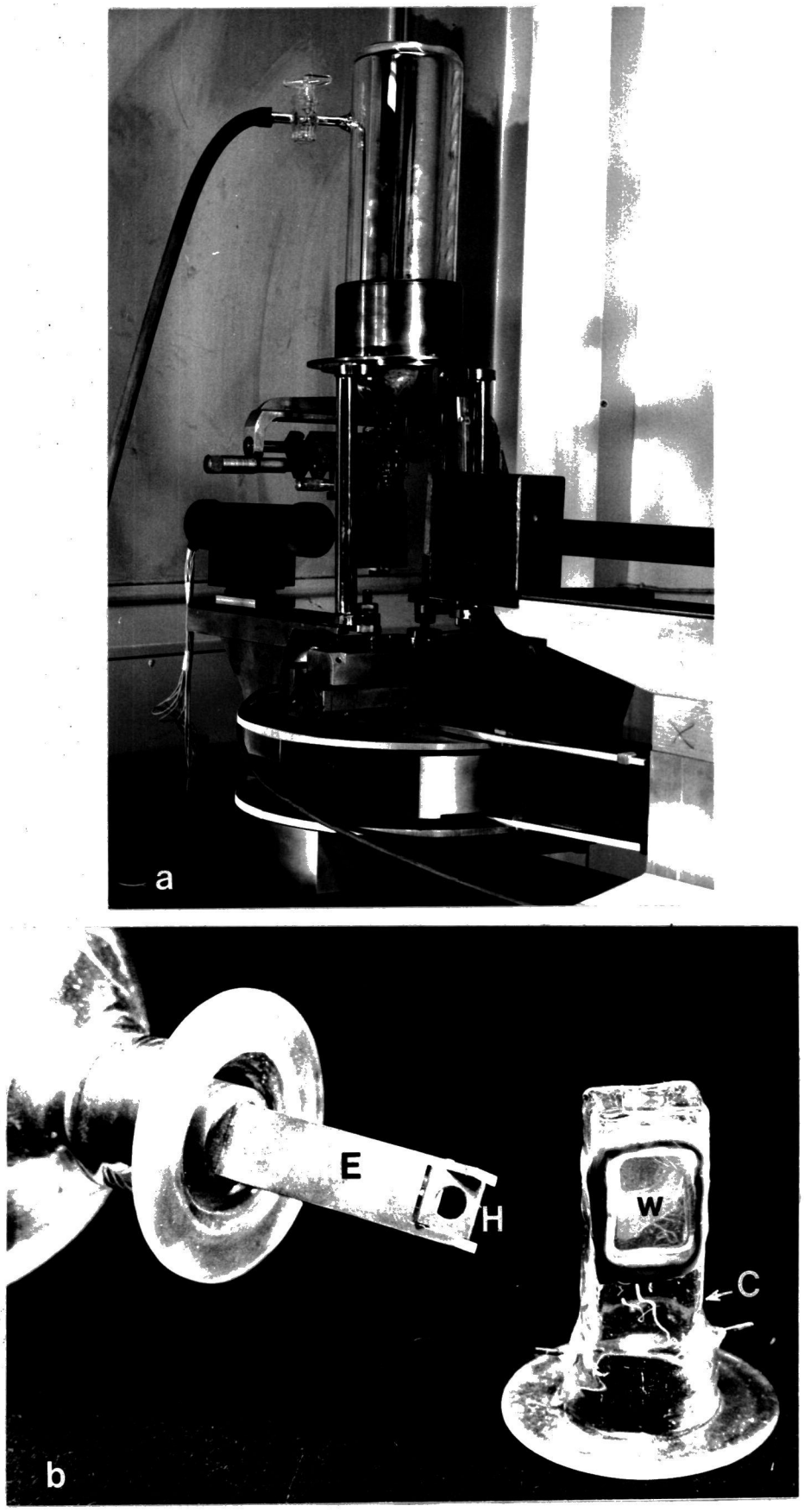

Fig.(5-1) (a) The glass cryostat mounted on Lang camera.

(b) Details of the lower part of the cryostat, note the cold finger E and specimen holder H, and mylar windows W on the cap C.

while at the same time being traversed across the X-ray beam. It turns out to be almost impossible to place the whole assembly between the pole pieces of an electromagnet having a gap of 2-5 cm. Only one example of a topographic study in magnetic fields up to 10 KOe has been performed by Yamada et al. (1966). This is a room temperature study of antiferromagnetic domains in NiO using the Berg-Barrett topography method in which no traversing mechanism is involved. As this is a reflection technique, domains in the interior of the crystal were not imaged.

in Chapter Three the advantages of X-ray topography using synchrotron radiation were discussed, and we saw that with the 5 Gev electron synchrotron NINA at Daresbury Laboratory a geometrical resolution of 1 μm can be achieved when the specimen to plate distance is 10 Cm, and no scan is needed. Synchrotron radiation enables many new experiments to be designed which require considerable quantities of other apparatus around the specimen. For the first time this technique was employed to study domain behaviour of $KNiF_3$ and $KCoF_3$ in the presence of magnetic fields up to 14 KOe at low temperatures, (Chapter Eight).

The glass cryostat proved to be particularly suited for synchrotron work. Fig. (5-2) shows the schematic arrangement of the cryostat and electromagnet for synchrotron topography. The cryostat was mounted directly on to the electromagnet coils, and as the specimen was arranged to be situated at the centre of the coils, the angle of tilt of the specimen could be changed without altering the height simply by sliding the cryostat mount around the rim of the electromagnet. Coarse

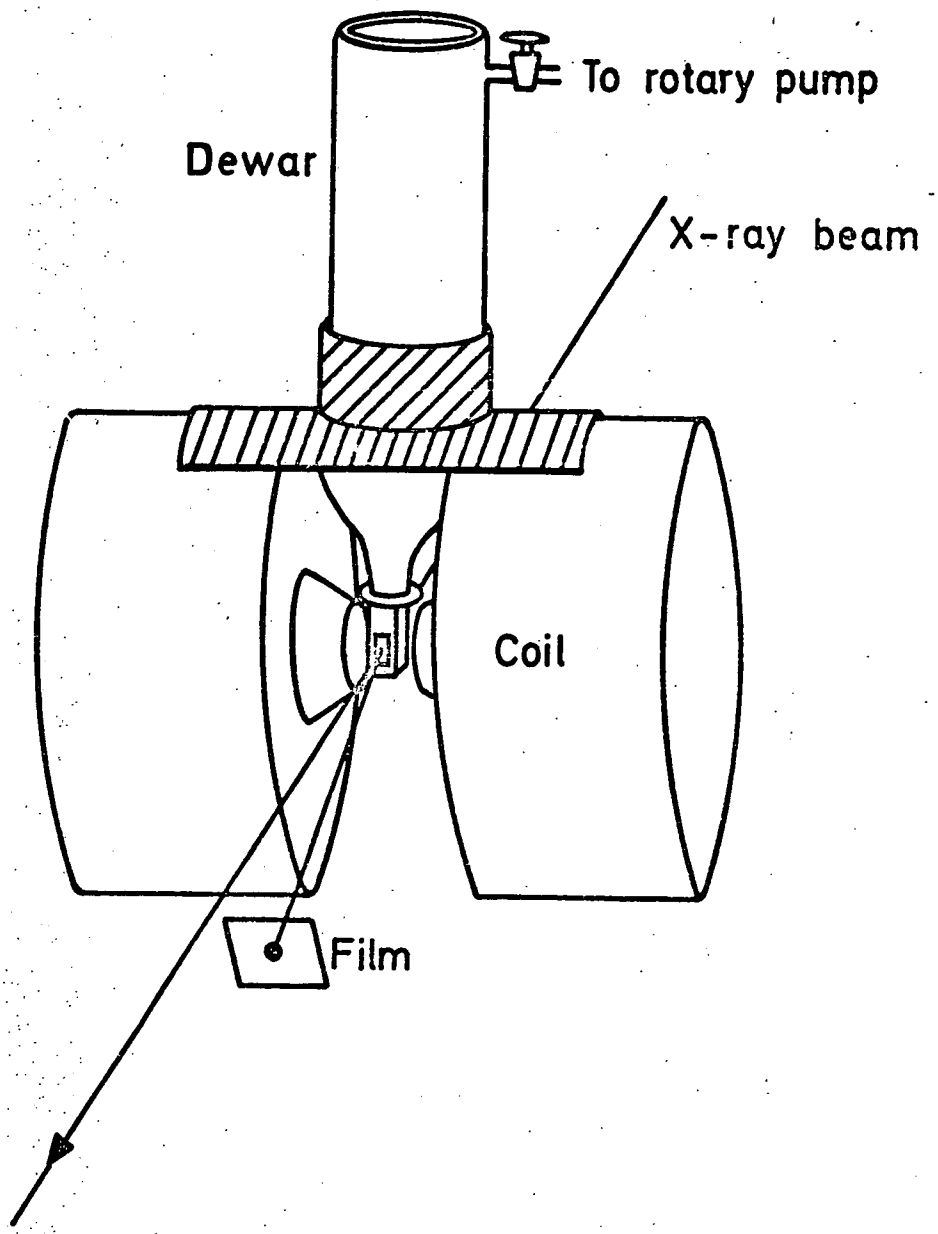

Fig.(5-2) Schematic diagram of the cold-finger cryostat mounted directly on the electromagnet coils C for synchrotron topography.

height adjustment was made by jacking the whole electromagnet up on four threaded legs. Lateral adjustment was made by pushing the whole electromagnet along its base by two large screws. Due to the almost complete polarization of the beam, the incidence plane was chosen to be vertical in order to maximize intensity. Consequently, the rotation of the specimen about a horizontal axis normal to the beam was sufficient. Brass specimen holders of this cryostat were capable of this rotation. The electromagnet used was a Newport 4 inch model providing a field of 13 KOe at 12A in a gap of 2.6cm. The intensity of synchrotron radiation is extremely high and therefore, due to the health hazard, no adjustments can be made with the X-ray beam on unless they are performed remotely.

As mentioned in section (3-5) the specimen can be aligned in the laser beam marking the path of the X-ray beam. Use of transparent mylar for the X-ray window permitted observation of the position of the light beam on the specimen, and the adjustment of the specimen was easy. The cryostat was used for domain wall motion studies of $KNiF_3$.

5.3 Stainless Steel Cryostat with a Gas-Cooled Tail

This variable temperature cryostat was manufactured by Meric for work in the temperature range of 2-300 K. Fig.(5-3) shows a schematic diagram of the cryostat. The specimen is cooled by convection in a current of helium drawn off from the reserve through a needle valve. Circulation of coolant is achieved by pumping on the central canal containing the crystal which is mounted on a holder enabling 360° rotation in the vertical plane to be obtained while the specimen is at low temperature. This rotation is extremely useful for fine

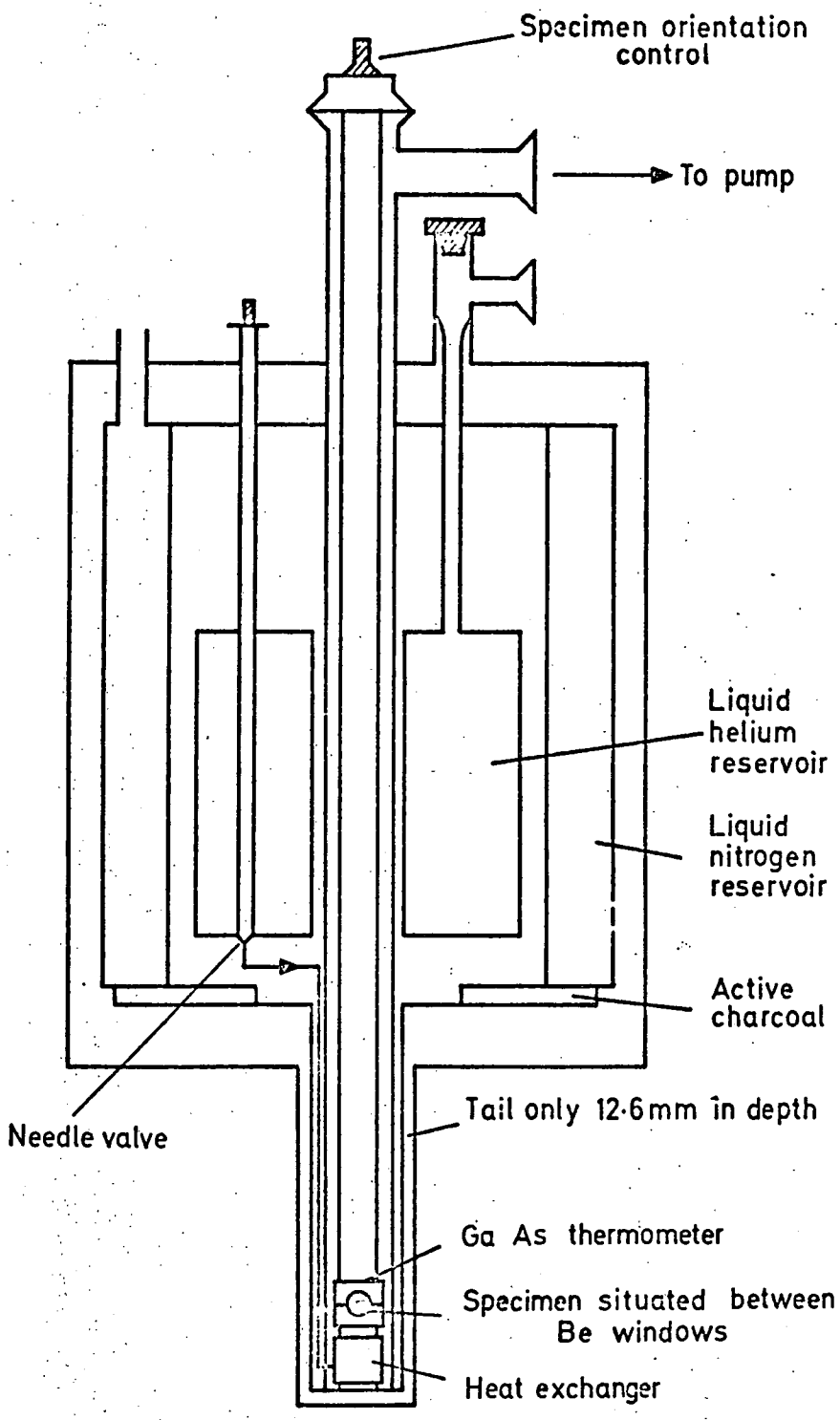

Fig.(5-3) Schematic diagram of the Meric cryostat for X-ray topography at liquid helium temperature.

adjustments and also for taking topographs of different reflections while the sample is kept in a desired low temperature. By means of the heat exchanger, which incorporates an electrical heater, temperatures above 4.2K may be maintained with the stability of 0.02 K. The helium reserve is of 2 litres capacity and is surrounded by a liquid nitrogen shield of capacity 3.4 litres. At 4.2 K one 2-litre fill of liquid helium lasts between 10 and 12 hours, so relatively long exposures on the Lang camera are possible. Fig.(5-4a) shows the Meric cryostat mounted on the Lang camera, using the rotating anode GX6 X-ray generator. For Lang topography it is extremely important that the film be placed very close to the specimen and the cryostat tail containing the specimen holder is so designed as to be only 1.26 cm thick. As seen in Fig.(5-4b), with care it is possible to place the film within 1 cm of the crystal. Two beryllium windows W in the tail allow passage of the X-rays. Temperature measurement and its control is achieved by means of a Ga As thermometer mounted on the specimen holder.

Fig.(5-5) shows the front and back views of the Meric cryostat mounted between the magnet pole pieces at the end of the beam line in the NINA Synchrotron Radiation Facility. The emulsion plate holder F was mounted on the outside of the electromagnet coils at a distance of 15 cm from the specimen.

This cryostat could satisfy both long exposure requirements of Lang topography and the short exposure requirements of synchrotron topography, although because of its relatively wide tail (5 cm), using the Newport 4 inch electromagnet, only fields of 6.4 KOe at the specimen was achieved. This cryostat

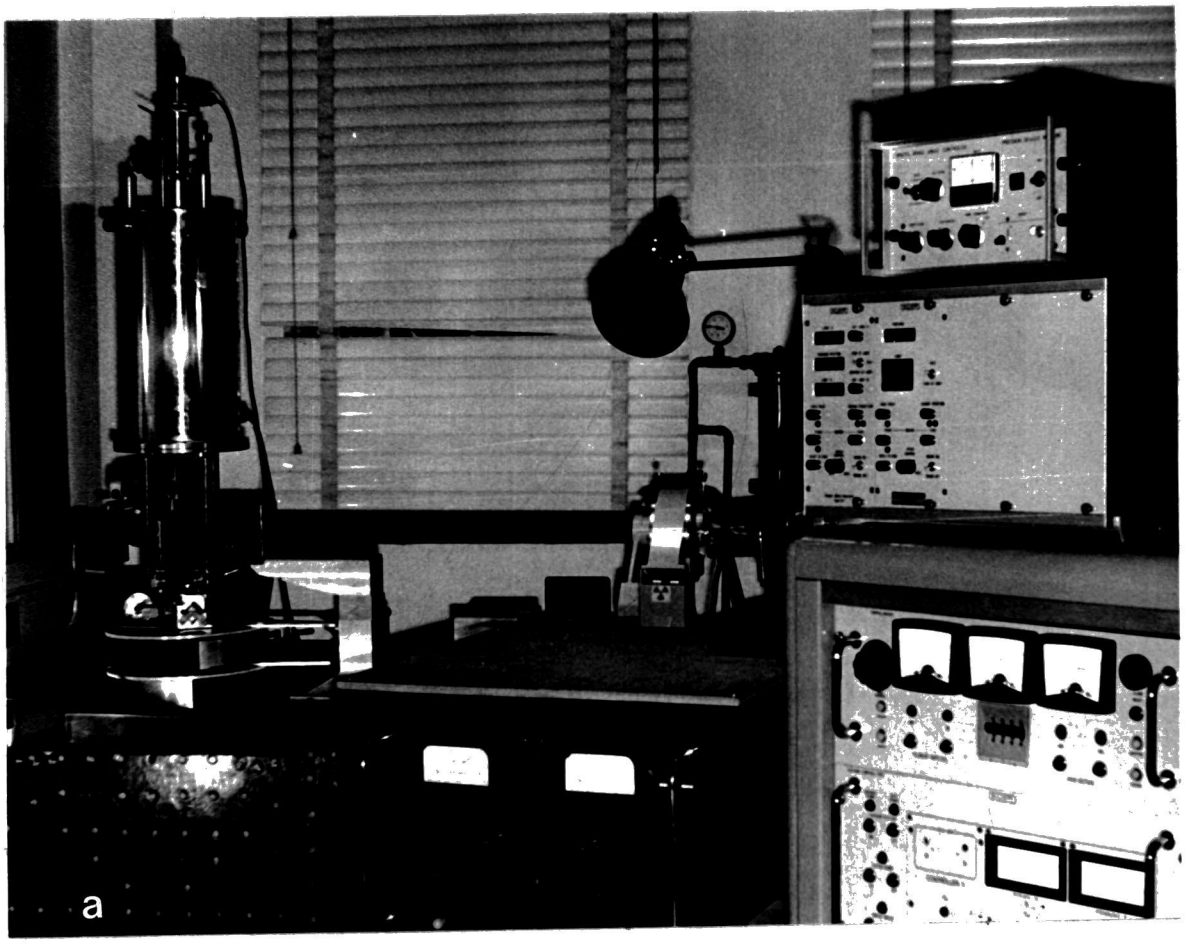

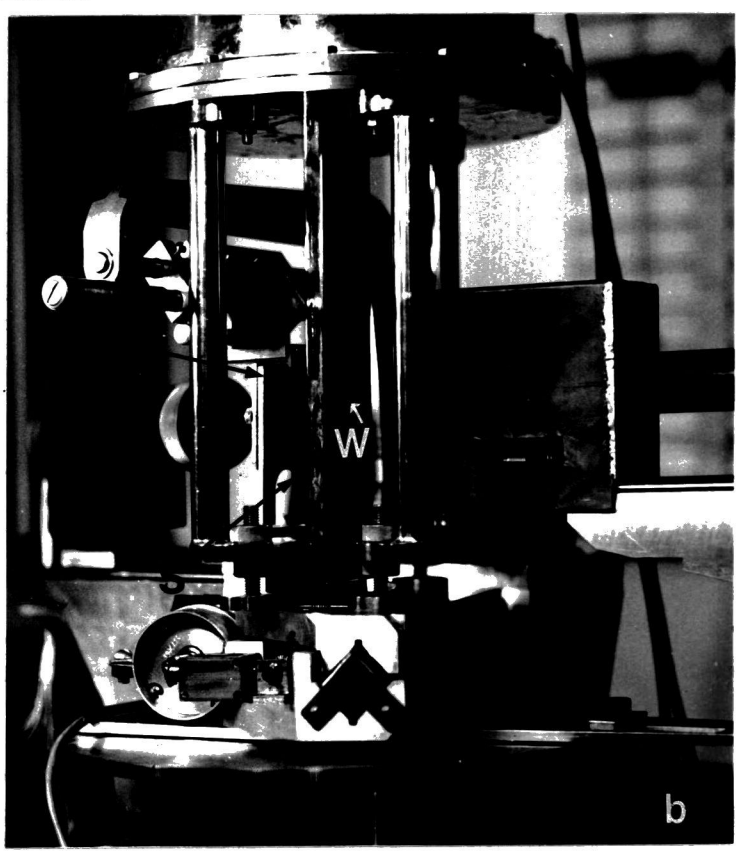

Fig.(5-4) (a) The Meric cryostat mounted on the Lang camera, using rotating anode GX6 X-ray generator.

(b) The position of the tail of the cryostat, slits, S, and film F for Lang topography.

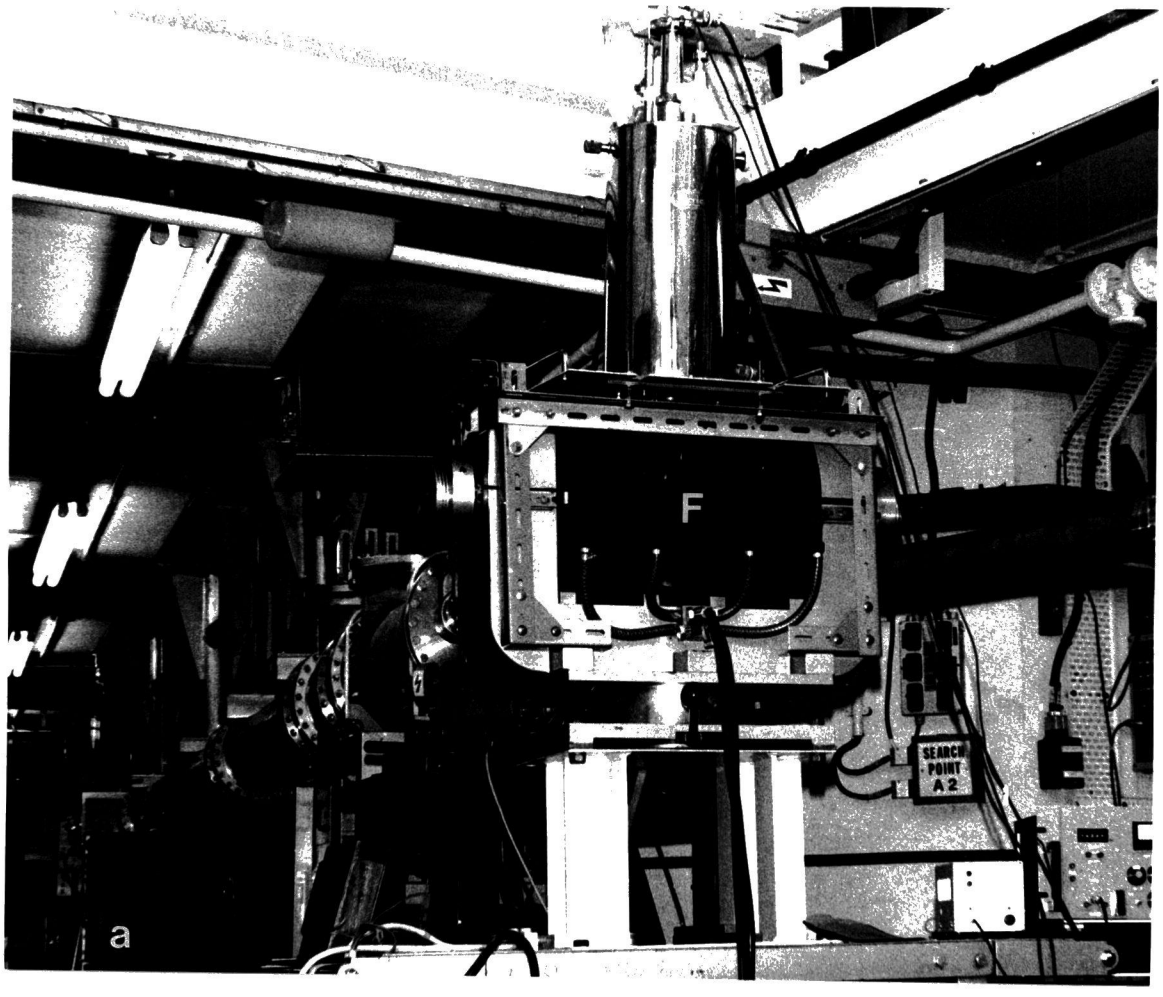
F
SEARCH
POINT
A2
a

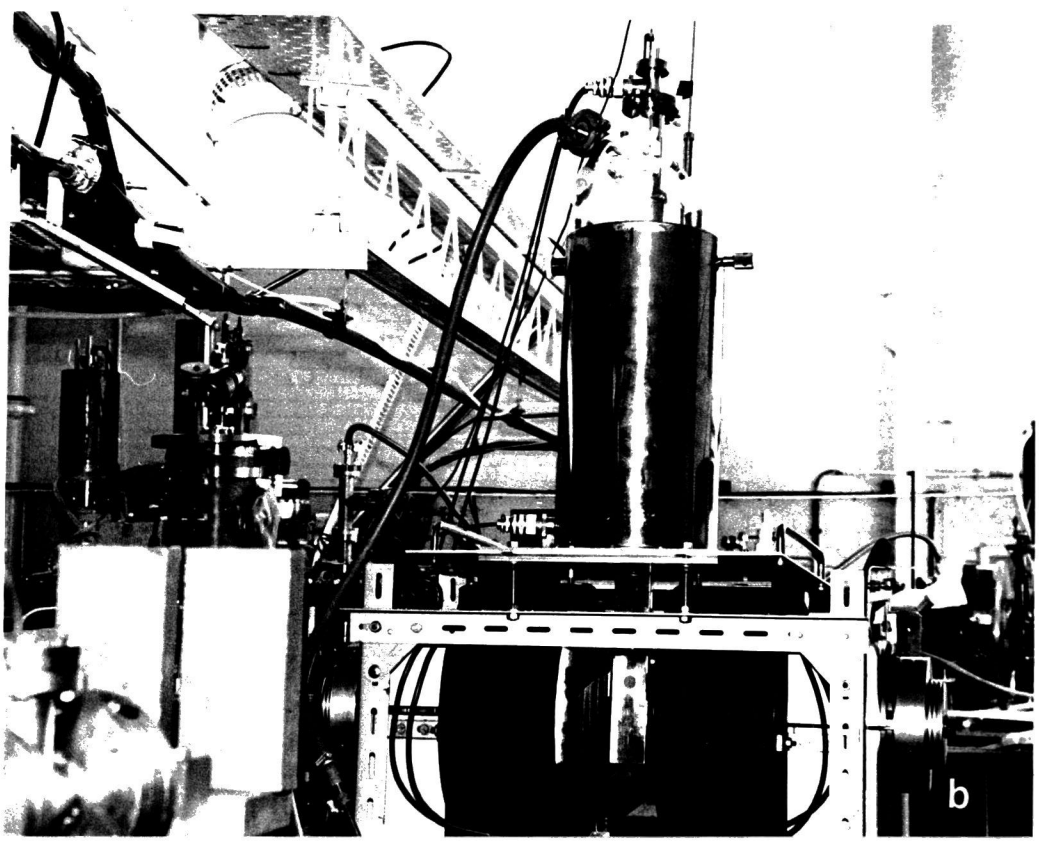

Fig.(5-5) Photograph of the Meric cryostat mounted between the electromagnet pole pieces on the beam line from NINA at Daresbury.

(a) Front view, (b) back view.

was extremely useful for domain wall motion studies of $KNiF_3$ and for this purpose the magnetic fields up to 6.4 KOe were sufficient.

5.4 Glass Cryostat with no X-ray Window

Domain wall movement experiments revealed that the critical magnetic field at which antiferromagnetic domain wall motion ceased in $KCoF_3$ was considerably higher than the maximum field (6.4 KOe)which could be obtained using the Meric cryostat and Newport 4 inch electromagnet. As the transition temperature of $KCoF_3$ is T_N = 114 K, a cryostat capable of achieving stable temperature well below 114 K was needed. Although the glass cryostat with mylar windows and cold finger had a tail of 2.4 cm width, and experiments up to 1.3 T could be performed with it, because of heat loss the achieved temperature depended upon the vacuum condition of the cryostat, and one could not be certain of the actual temperature of the sample. Therefore the problem was to design a cryostat capable of achieving higher magnetic fields at 77 K. The only solution was to reduce the gap between the pole pieces, but at the same time maintaining a temperature of 77 K. The problem was overcome by immersing the specimen in liquid nitrogen contained in a thin-walled narrow-tailed glass cryostat. Although the absorption of X-rays in the glass and liquid nitrogen is considerable, by exploiting the enormous intensity of synchrotron radiation this kind of cryostat proved to be successful. As illustrated in Fig.(5-6) the specimen was attached to a brass holder on the end of a stainless steel rod clamped at the top of the dewar. The tail of the dewar was left unsilvered, and thus, it was easy to align the crystal

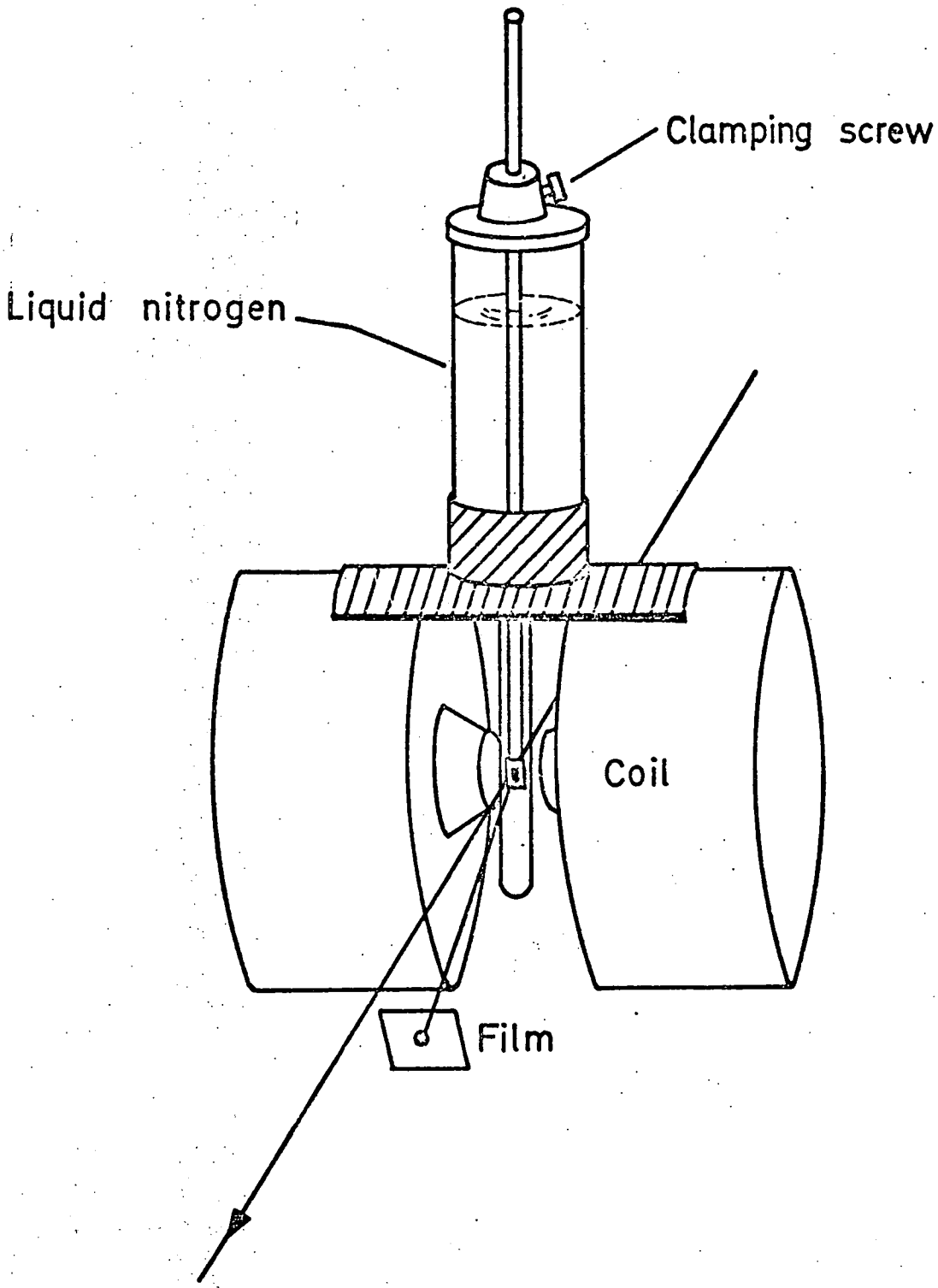

Fig.(5-6) Schematic diagram of the windowless cryostat for high field work at 77K.

in the laser beam while it was immersed in the liquid nitrogen. Although considerable bubbling occurred at the specimen due to the heat leak down the stainless steel holder, this did not seem to cause unacceptable vibration of the specimen. The glass cryostat worked extremely well particularly as the glass rather conveniently absorbed the nitrogen scatter and much of the background from the direct beam. The topographs of KCoF in different steps of fields up to 14 KOe taken with this cryostat will be presented in Chapter Eight.

The intensity of the synchrotron topographs was calculated by Tuomi et al (1974) and was given by expression (3-1). In the case of this glass cryostat, the absorption of X-rays in the glass and nitrogen should also be taken into account, therefore the intensity of the {hkl} diffracted beam is given by

$$I_{hkl} \sim P(\lambda). \quad F_{hkl} \frac{\lambda^3 . S}{\sin^2\theta} e^{-(\mu t + \mu_1 t_1 + \mu_2 t_2)} \qquad (5\text{-}1)$$

Where S is the film sensitivity which varies with λ. μ, μ_1 and μ_2 are the absorption coefficients of the specimen, liquid nitrogen, and glass, t, t_1 and t_2 are the thicknesses of the specimen, nitrogen, and glass respectively. The other symbols have their usual meaning. According to the analysis of the Jobling Laboratory Group Glass, the following is a typical composition of the glass used for the construction of this cryostat,

SiO_2	80.60%	CaO	0.1%
B_2O_3	12.60%	Cl	0.1%
Na_2O	4.15%	MgO	0.05%
Al_2O_3	2.20%	Fe_2O_3	0.05%

The absorption coefficients μ, μ_1, μ_2 for different wavelengths were obtained from the International Tables for X-ray Crystallography (1962). The thickness of liquid nitrogen in the tail of the dewar was t_1= 1 cm and the total glass thickness of the dewar t_2 = 0.6 cm. Using the values of $P(\lambda)$ from Fig. (3-1), film sensitivity S from Hart (1975) and values of structure factors F_{hkl} from table 1 of Appendix I, the intensities I_{hkl} could be calculated. Fig. (5-7) shows the relative intensities of the diffracted beam from {100} planes of $KNiF_3$ as a function of Bragg angle, at 5 Gev electron energy, with and without the glass cryostat and nitrogen. As might be expected all wavelengths except those less than about 0.7 Å suffer very marked absorption in the glass. For all Bragg angles there is an increase in the exposure time of roughly a factor of twenty. Using a conventional X-ray generator and a Lang camera such an increase would be unacceptable but with the very high flux produced by the synchrotron an increase of the exposure time from 20 seconds to 6 minutes caused no inconvenience.

5.5 Polystyrene Immersion Cryostat

The absorption of X-rays in glass is relatively high, and this results in a considerable increase in exposure time for topographic experiments using the glass immersion cryostat. In order to overcome this problem it seemed an obvious step to attempt to contain the liquid nitrogen in an expanded polystyrene container and again immerse the specimen in the liquid. The construction of the cryostat was extremely easy, and in fact, it was fabricated from scrap expanded polystyrene in approximately ten minutes. Fig.(5-8) shows the schematic

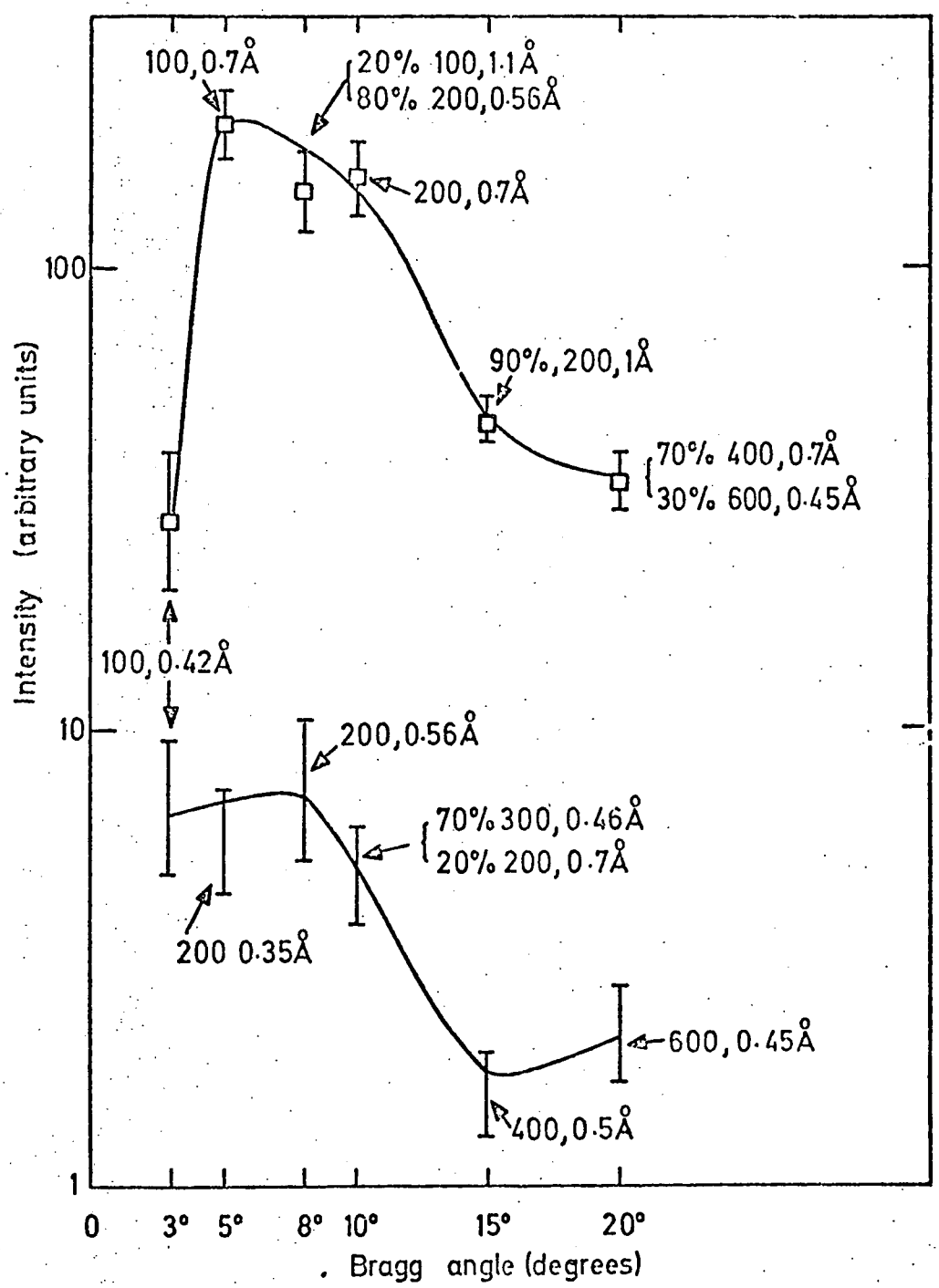

Fig.(5-7) Intensities in transmission of the beams diffracted from {100} planes of $KNiF_3$ as a function of the Bragg angle at 5 Gev. (a) Upper curve is for the crystal without cryostat, (b) Lower curve shows equivalent intensities for a crystal inside the windowless glass cryostat.

diagram of the expanded polystyrene cryostat, and the specimen support rod clamped in a retort stand. As polystyrene is opaque to light, it was not possible to adjust the position of the specimen while immersed in the liquid, therefore the crystal was aligned in laser beam prior to bringing up the polystyrene container. Contraction of the support rod on cooling did not cause trouble, and again although bubbling occurred at the specimen this did not affect the resolution. Using this cryostat, it was proved that the resolution of dislocation lines at 77 K is still good. The inside dimensions of the polystyrene container which was used for this experiment were 40 x 6 x 3 cm^3, and the thickness of polystyrene was about 1.5 cm. The boil off rate was found to be quite low and topping up was only necessary approximately every half hour.

Fig. (5-9) shows the intensities of $\{100\}$ topographs of $KNiF_3$ as a function of Bragg angle, at 5 Gev electron energy. Here only nitrogen absorbs X-rays and the absorption of polystyrene is negligible. As seen in Fig.(5-9) the removal of the glass results in a gain of a factor of four in exposure time for a nitrogen path of 3 cm.

The naive design of this cryostat proved to be very successful. However, there are only two disadvantages which may be improved as follows,

1. This cryostat operates only at fixed temperatures (e.g. liquid nitrogen or dry ice methanol temperature) but by using an insert and heater coil one can overcome this limitation.

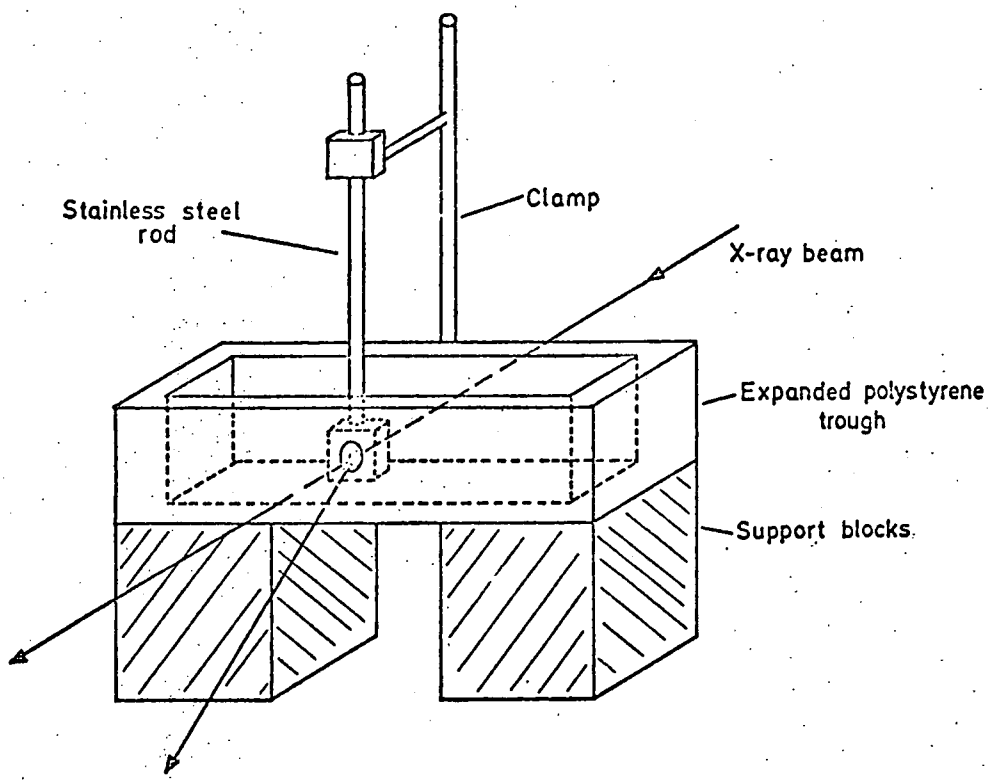

Fig.(5-8) Schematic diagram of the expanded polystyrene cryostat.

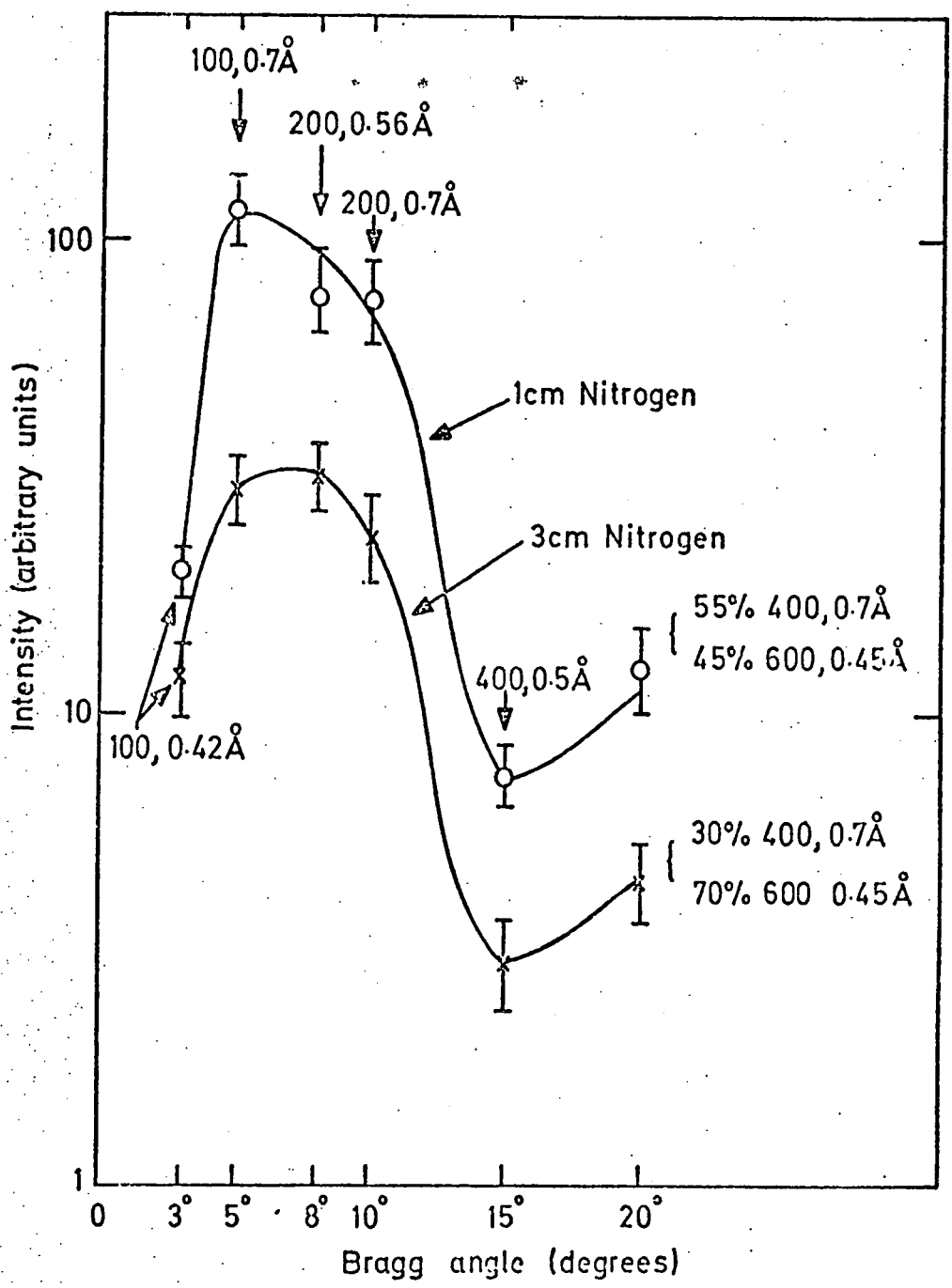

Fig.(5-9) Intensities for a crystal immersed in liquid nitrogen contained in an expanded polystyrene trough.

2. The nitrogen scatters appreciably and causes a considerable increase in the background. In order to reduce the scattering, small Bragg angles should be avoided and also the photographic plate must be placed sufficiently far from the specimen.

Because of the availability of high flux synchrotron radiation, the cryostat design in topography is not now dictated by the topographic camera, and many new experiments are possible in which X-ray topographs are taken simultaneously with other measurements.

CHAPTER SIX

STATIC DOMAIN STUDIES IN $KNiF_3$ AND $KCoF_3$ BY X-RAY TOPOGRAPHY

6.1 Predicted Domain Studies

The torque magnetometry experiments of Hirakawa et al. (1961) showed that the spins in $KNiF_3$ and $KCoF_3$ crystals lie in $\langle 100 \rangle$ directions. Hirakawa and his co-workers considered the existence of domain (twinned) structures in $KNiF_3$ and assumed the crystal to consist of three kinds of domains in each of which the direction cosines of the spin axes relative to the cubic axes are 1,0,0, 0,1,0, and 0,0,1 respectively. Thus domain walls lying in the $\{110\}$ planes are to be expected. Using the proposed model for domain walls and Nagamiya's (1960) ideas concerning domain wall movement, Hirakawa et al. concluded that the origin of the observed 4θ-term in the torque curves arose from reversible movement of the antiferromagnetic domain walls in $KNiF_3$. Spectroscopic experiments of Ferré et al. (1976) and Petit et al. (1975) also indicated the existence of domain walls in $KNiF_3$ and $KCoF_3$, and confirmed the domain wall geometry which was proposed by Hirakawa et al. However, no direct evidence for antiferromagnetic domain walls in $KNiF_3$ existed prior to this work.

6.2 Observation of Domain Walls in $KNiF_3$

At 246K the cubic perovskite $KNiF_3$ undergoes an antiferromagnetic transition but unlike related compounds no

deviation from cubic symmetry has been detected by classical X-ray diffractometry (section (1-6)). Although no distortion had previously been observed in the antiferromagnetic region of $KNiF_3$, in the present work, antiferromagnetic domain walls were observed in highly perfect $KNiF_3$ crystals.

Fig.(6-1) shows a topograph of a crystal of $KNiF_3$ taken at the temperature T = 100K using the glass cryostat with cold finger. The room temperature topograph of this crystal was shown in Fig.(4-3), and as seen this particular crystal was a highly perfect $KNiF_3$ sample. A well defined domain configuration is observed, consisting of two sets of walls parallel to each of the $\langle 011 \rangle$ directions in the specimen plane.

Fig.(6-2) shows an 011 type topograph, where one set of walls lies parallel to and one set perpendicular to the diffraction vector $\underline{g}$. When the specimen was vertical no walls were visible, but on tilting the crystal approximately 15° about the diffraction vector the walls parallel to $\underline{g}$ became visible, while the other set remained invisible. The effect of the tilt angle on the observation of domain wall contrast was demonstrated in Fig.(2-11). As seen in Fig.(6-2), the walls perpendicular to $\underline{g}$ are invisible. The rule for the invisibility of walls based on the coherent twin model is $\Delta\underline{M}.\underline{g} = 0$. Therefore $\Delta\underline{M}$ is parallel to the $[0\bar{1}1]$ direction, and assuming 90° type walls, the sublattice magnetization in $KNiF_3$ is parallel to the $\langle 100 \rangle$

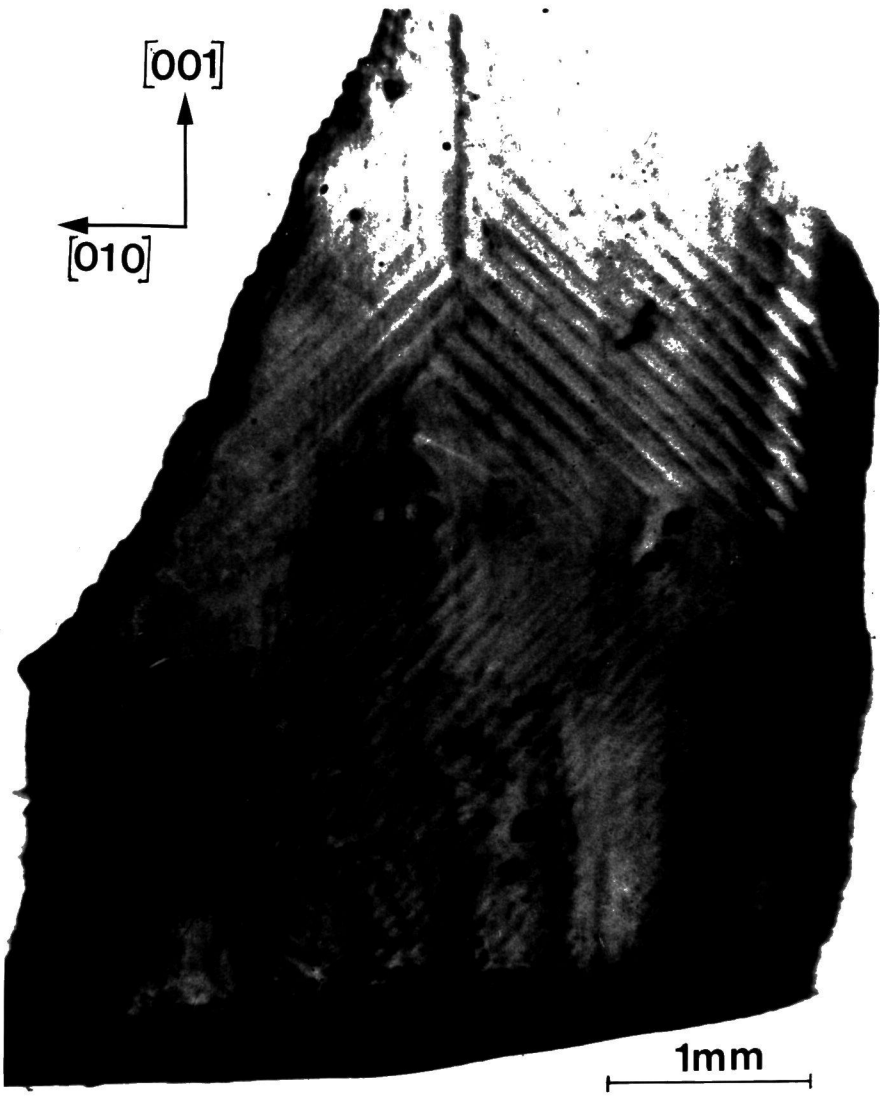

Fig.(6-1) Lang topograph of a crystal of $KNiF_3$ at T=100K. Mo$K\alpha_1$, 020 reflection, recorded on 50μm Ilford L4 Nuclear Emulsion, exposure time 2h. Anti-ferromagnetic domains with walls in $\langle 110 \rangle$ directions are visible.

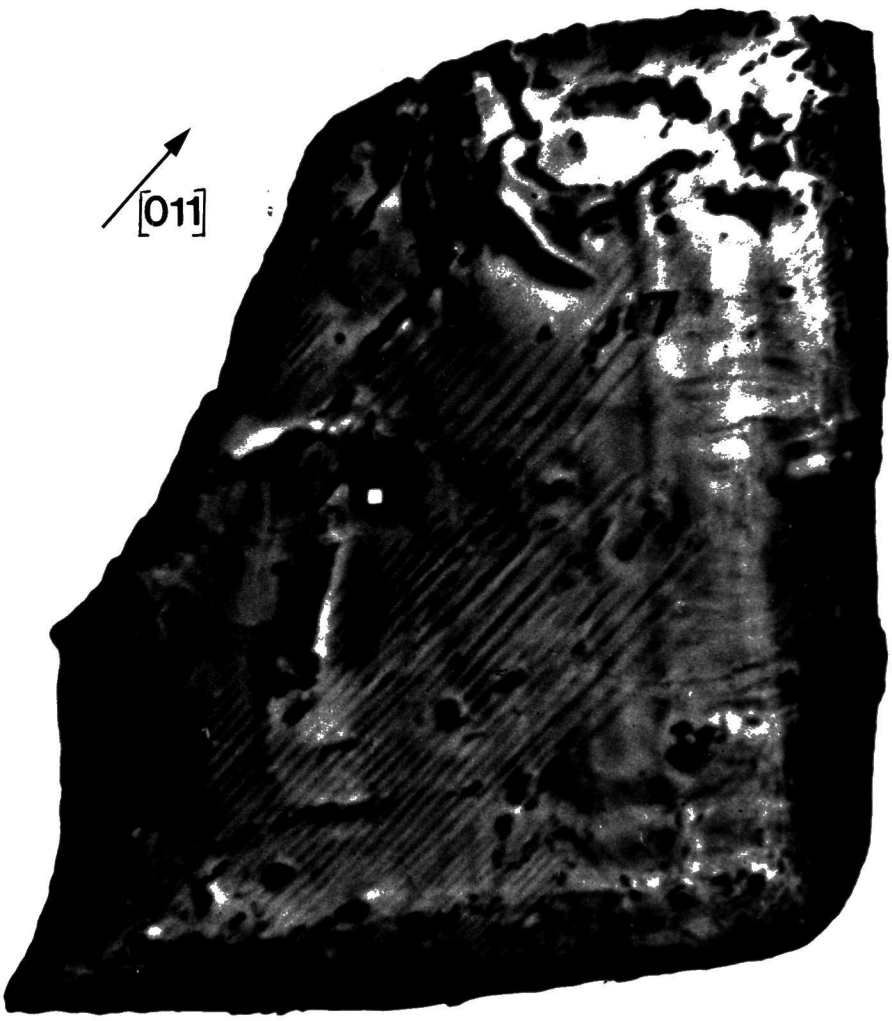

Fig.(6-2) 011 type Lang topograph of the same crystal as in Fig.(6-1), MoKα_1 radiation. Now the set of walls parallel to [0$\bar{1}$1] are invisible.

direction which is in agreement with Hirakawa et al.'s results.

The contrast of the domain wall on X-ray topographs arises from the difference in magnetostrictive deformation on opposite sides of the wall. Therefore a small tetragonal magnetostrictive distortion accounts for the observation of domain walls. No splitting of the rocking curve was observed in the Lang camera, indicating $\frac{c-a}{a} \lesssim 10^{-4}$. However, quite strong topographic contrast is found and one can tentatively ascribe a lower limit of $\frac{c-a}{a} \gtrsim 10^{-5}$, corresponding to the angular reflection range of the perfect crystal.

Fig.(6-3) shows a topograph of the same crystal at a temperature of around 200K (using the glass cryostat with cold finger containing dry ice and methanol). Two sets of $[011]$ and $[0\bar{1}1]$ domain walls similar to Fig.(6-1) are observed, but the contrast is rather faint, and this is due to the decrease of magnetostrictive deformation at T = 200K.

The domain configuration is not reproducible on successive cooling below T_N. After taking the topograph shown in Fig.(6-1), the specimen was warmed above the Néel temperature and subsequently cooled to T = 100K again. This time the domain pattern which was obtained, Fig.(6-4), differs from what is seen in Fig.(6-1). Now two sets of walls A along $\langle 011 \rangle$ directions and one set of walls B with wide images lying on inclined $\{011\}$ planes are observed. The small strains introduced in mounting markedly

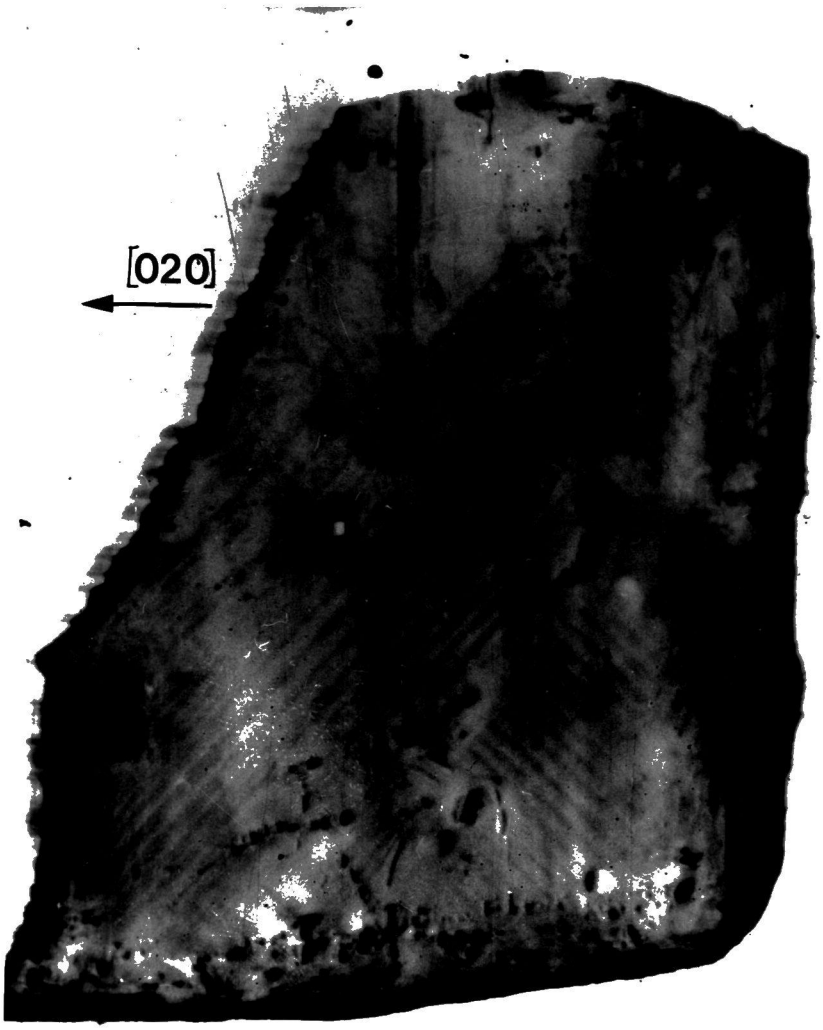

Fig.(6-3) 020 Lang topograph of the same crystal of $KNiF_3$ at T=200K $MoK\alpha_1$ radiation. Note two sets of $\langle 110 \rangle$ walls with faint contrast are visible.

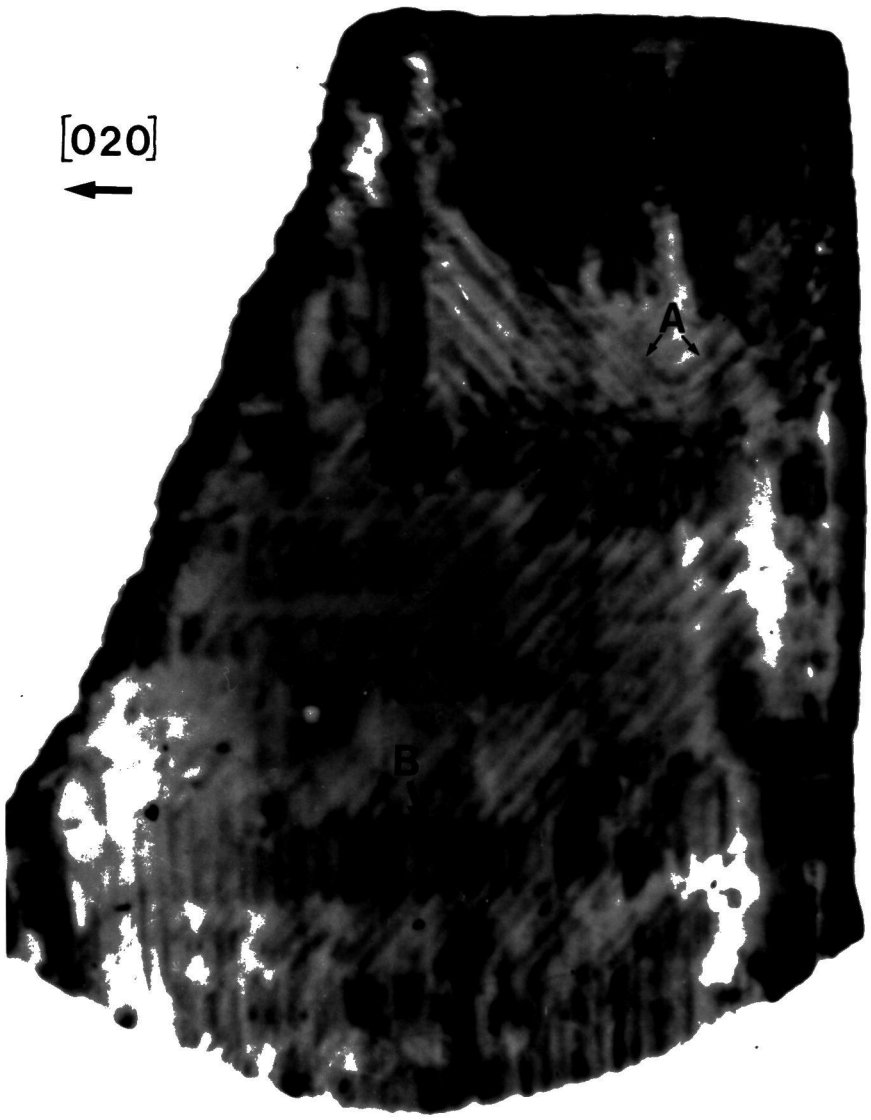

Fig.(6-4) Domain pattern obtained when the specimen was warmed above the Néel temperature and subsequently cooled to T=100K again. 020 reflection MoKα_1 radiation.

influence the domain pattern. Figs.(6-5 and 6-6) illustrate the influence of mounting conditions for the same crystal of $KNiF_3$ at 100K. When the crystal was mounted with a small amount of glue on one corner, a low stress configuration of domains was obtained, Fig.(6-5). Walls X are sharp indicating that they lie close to {011} planes when unstressed. Walls Y give wide images as they lie on inclined {011} planes. When the same crystal was slightly stressed in mounting, domain walls do not exactly lie on {011} planes, Fig.(6-6).

It is extremely important to have a highly perfect crystal of $KNiF_3$ for domain studies with X-ray topography. As the magnetostriction is very small, if the crystal contains growth bands or a high density of dislocations, when the crystal is cooled through its Néel temperature the magnetostrictive distortion will be much smaller than the distortions which the imperfections introduce and domain observations will not be successful. To emphasise how vital it is that highly perfect specimens be used if successful domain observations are to be performed, a much less perfect crystal of $KNiF_3$, Fig.(4-6), in which the dislocation density was high and individual defects could not be clearly seen was studied at low temperatures. Fig. (6-7) shows the same crystal at 100K, illustrating that in most of the imperfect parts the domains can not be observed and even in the regions in which domains are seen the contrast is very weak. Again in Fig. (6-8) because of very strong growth bands in a crystal of $KNiF_3$, in most parts of the

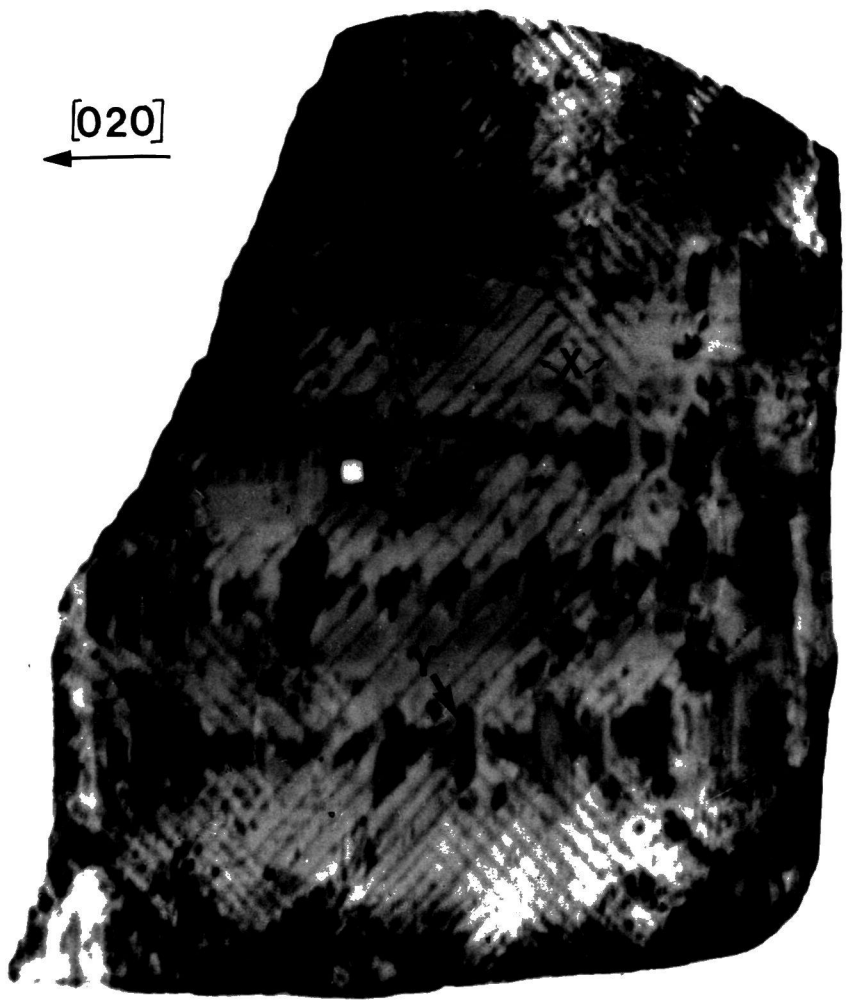

Fig.(6-5) Lang topograph of the same crystal of $KNiF_3$ at T=100K. $AgK\alpha_1$ radiation, 020 reflection.

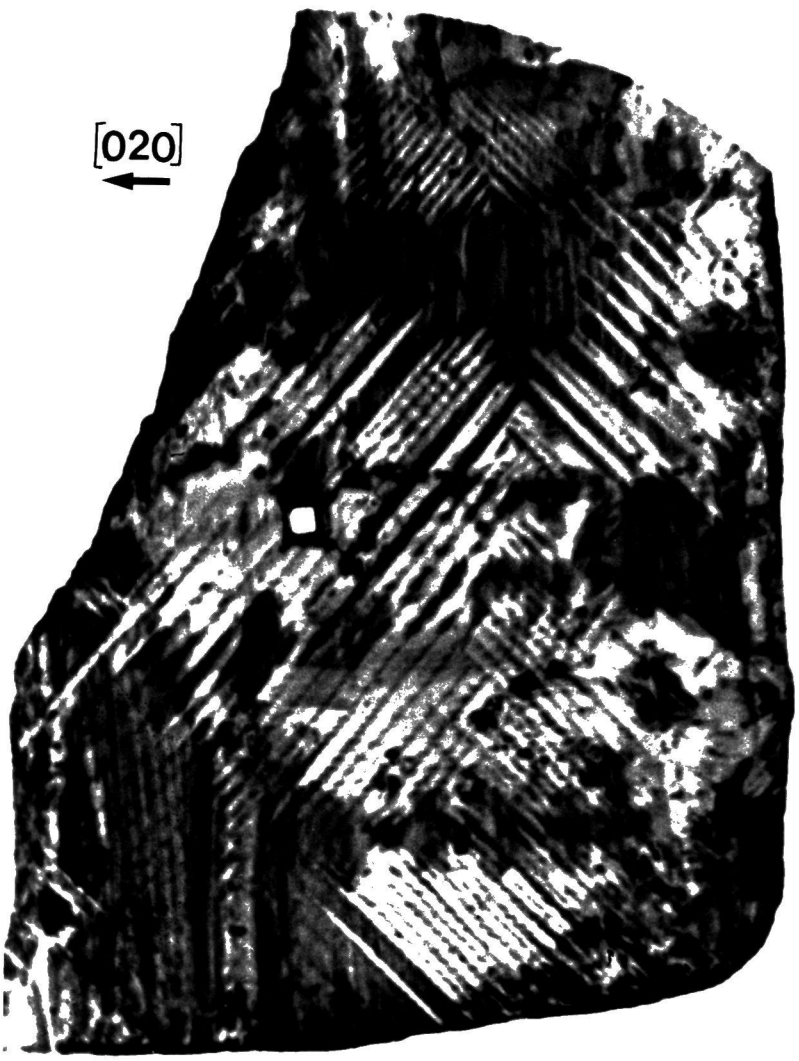

Fig.(6-6) Lang topograph of the $KNiF_3$ crystal at T=100K. In this experiment the crystal was mounted with a lot of glue. $AgK\alpha_1$ radiation 020 reflection.

Fig.(6-7) 020 Lang topograph of a much less perfect crystal of $KNiF_3$ at T=100K. Domains can not be observed in the imperfect regions. $AgK\alpha_1$ radiation.

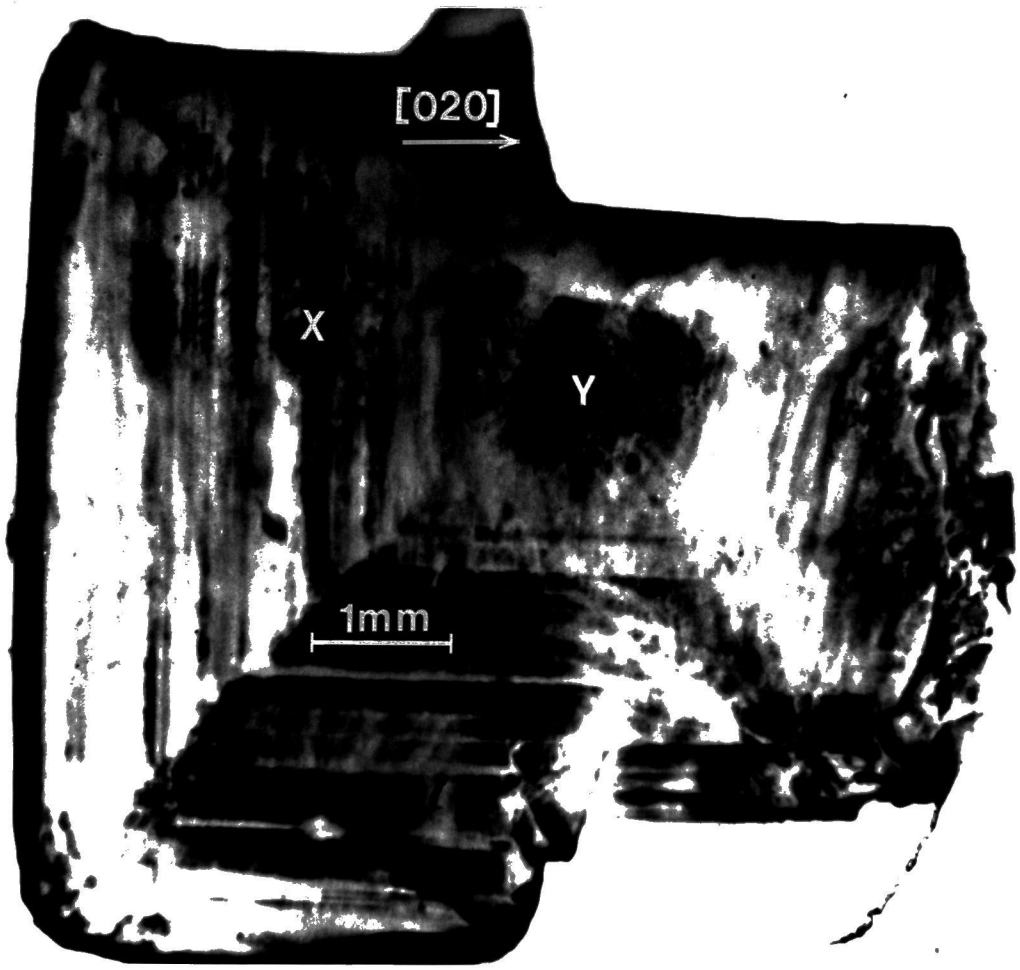

Fig.(6-8) Lang topograph of a crystal of $KNiF_3$ with very strong growth bands at T=100K. 020 reflection AgKα_1 radiation. $\langle 011 \rangle$ oriented domain walls are only observed in the regions, X and Y.

specimen domain walls do not appear and only in the regions X and Y are walls visible. This is because the imperfection distortion dominates the small magnetostrictive distortion.

6.3 Observation of Domain Walls in $KCoF_3$

At 114K, the perovskite $KCoF_3$ crystal becomes antiferromagnetic and classical crystallographic measurements indicate that below the Néel temperature a tetragonal distortion accompanies this transition. According to Julliard and Nouet (1975) the distortion at 78K is $\frac{c-a}{a} \simeq -2.5 \times 10^{-3}$, and the temperature dependence of $\frac{c-a}{a}$ for $KCoF_3$ was illustrated in Fig.(1-7).

Although domains were observed in zero field at 78K by Schlenker and his co-workers (1974), the domain pattern they obtained was not clear and they proposed a rather complicated model for the domain structure. In the present work extensive topographic experiments on different samples were performed to study the antiferromagnetic domain walls in $KCoF_3$ at 77K and 4.2K.

The first observation of domains in $KCoF_3$ was performed on a sample Fig.(4-7) which contained a high dislocation density in the lower region, but was more perfect in the upper part. Fig.(6-9) is the Lang topograph of the crystal taken at 77K using the Meric cryostat. In this micrograph very sharp domain walls of $\langle 011 \rangle$ orientation with strong contrast are observed. This micrograph illustrates the dependence of the contrast on the magneto-

Fig.(6-9) Lang topograph of a crystal of $KCoF_3$ at T=77K. (011) type walls are visible. 020 reflection $AgK\alpha_1$ radiation.

striction very well, and as it is large, it easily dominates the imperfection distortion. Therefore strong domain wall contrast is seen even in the deformed part of the crystal. Unlike Schlenker et al.(1974), the author has never observed substructure within the T domains in any experiment on different samples. Therefore it is concluded that the sublattice magnetization lies along the cube edges. This is in agreement with the torque data, Hirakawa et al.(1961).

Fig.(6-10) shows a synchrotron topograph of a $KCoF_3$ crystal at 77K. The polystyrene cryostat described in section (5-5) was used to perform this experiment. The crystal was glued at one corner, using a very small amount of varnish. Rather diffuse images of antiferromagnetic domains are visible at A and B, but the bulk of the crystal is single domain. This seems to be a common feature in $KCoF_3$ when it is carefully mounted without strain. The room temperature topograph of this sample was shown in Fig.(4-9). In the low temperature topograph Fig.(6-10), it seems that there is much diffuse contrast from inhomogenous strains arising from differential thermal contraction. However, the resolution of the dislocation lines D is still quite good and demonstrates that the bubbling of the nitrogen at the specimen does not lead to unacceptable vibration.

Experiments proved that the domain pattern is entirely dependent on the way the crystal is mounted, and the length of the sample in contact with the cement and sample holder.

Fig.(6-10) Synchrotron topograph of a $KCoF_3$ crystal taken at 77K using the expanded polystyrene cryostat. Antiferromagnetic domain walls appear at the top left and bottom right of the micrograph. 002 reflection, 7° Bragg angle. 5 Gev, 7mA, 20 seconds exposure on L4 25μm emulsion.

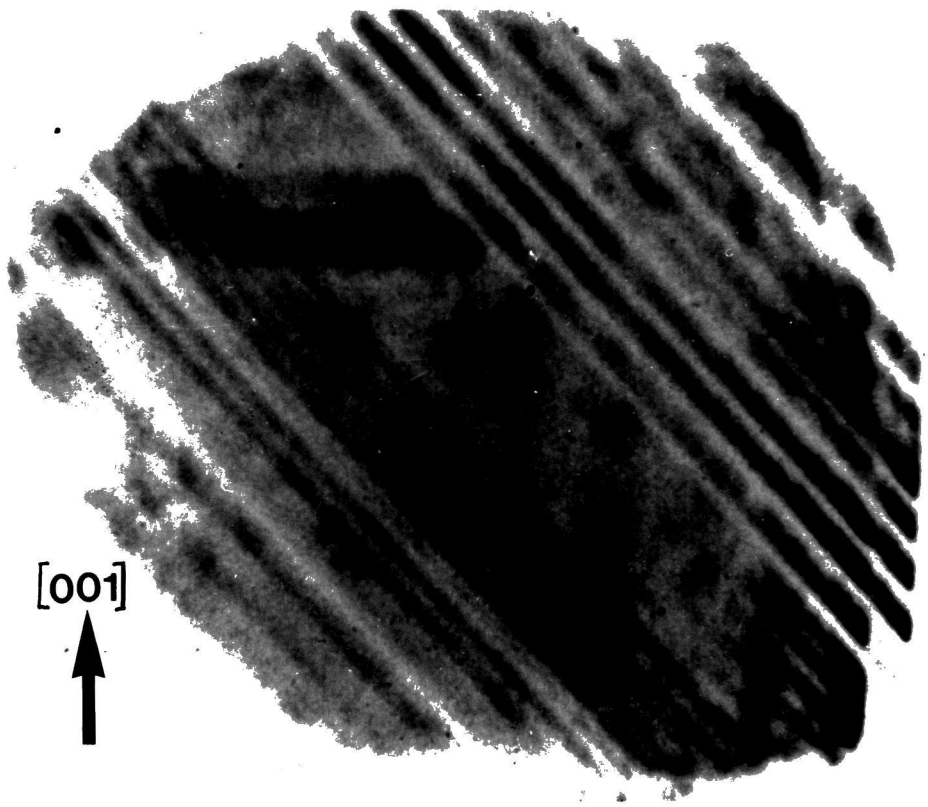

Fig.(6-11) Antiferromagnetic domains in the same $KCoF_3$ crystal at 77K with the polystyrene cryostat and mounted with more glue than in Fig.(6-10). 002 reflection, 8^{o} Bragg angle, 4 Gev, 5mA, 3 minutes exposure.

The domain configuration is influenced by the strain introduced on mounting. Fig.(6-11) shows a multi-domain pattern in the same $KCoF_3$ crystal, again using the polystyrene cryostat, but remounted using more glue. A markedly different domain configuration has resulted on cooling through the Néel temperature.

Fig.(6-12) is an optical micrograph of a $KCoF_3$ crystal mounted on a small ring and then fixed in the specimen holder of the Meric cryostat. This micrograph illustrates that a considerable amount of varnish was used to mount the crystal. The room temperature topograph of this crystal was presented in Fig.(4-8). At 4.2K a considerable number of domain walls running in $\langle 011 \rangle$ directions were observed on the synchrotron topograph of this crystal, Fig.(6-13). Analysis of the contrast in 011 type topographs show when $\underline{g}$ is perpendicular to a set of walls, they become invisible. The rule for the invisibility of the walls based on the coherent twin model is $\Delta \underline{M}.\underline{g} = 0$. Thus $\Delta \underline{M}$ is parallel to $[0\bar{1}1]$. This is to be expected for 90° walls between spins parallel to $\langle 001 \rangle$. No interaction of domain walls with a pair of dislocations d is observed, Fig.(6-13). It is noticed that the crystal was mounted on the holder in such a way that the lower side of it, was in contact with a large quantity of varnish and sample holder, and it is suggested that it is the influence of the cement which deforms the domain pattern in the lower part of the sample. Schlenker et al. (1974) also pointed out that the domain structure in

$KCoF_3$ was largely influenced by stresses and when they glued the sample so that the length of the [010] side in contact with the cement was reduced to about $\frac{1}{3}$ of its value in the preceding case: the domain structure which was then obtained consisted essentially of one T domain with a few imbedded lamellae. Hirakawa et al.(1961) did not detect any 4θ-term in the torque curves of $KCoF_3$ at 77K in the absence of any external stress. They mentioned that any undirectional stress along one of the edges of the twinned crystal, may make the sample single domain. It seems that the dependence of domain configuration on the mounting conditions is very complicated. Although it is possible to obtain a single domain crystal by applying a stress higher than the critical stress, it seems that a minimum stress is necessary to nucleate domain walls in the sample.

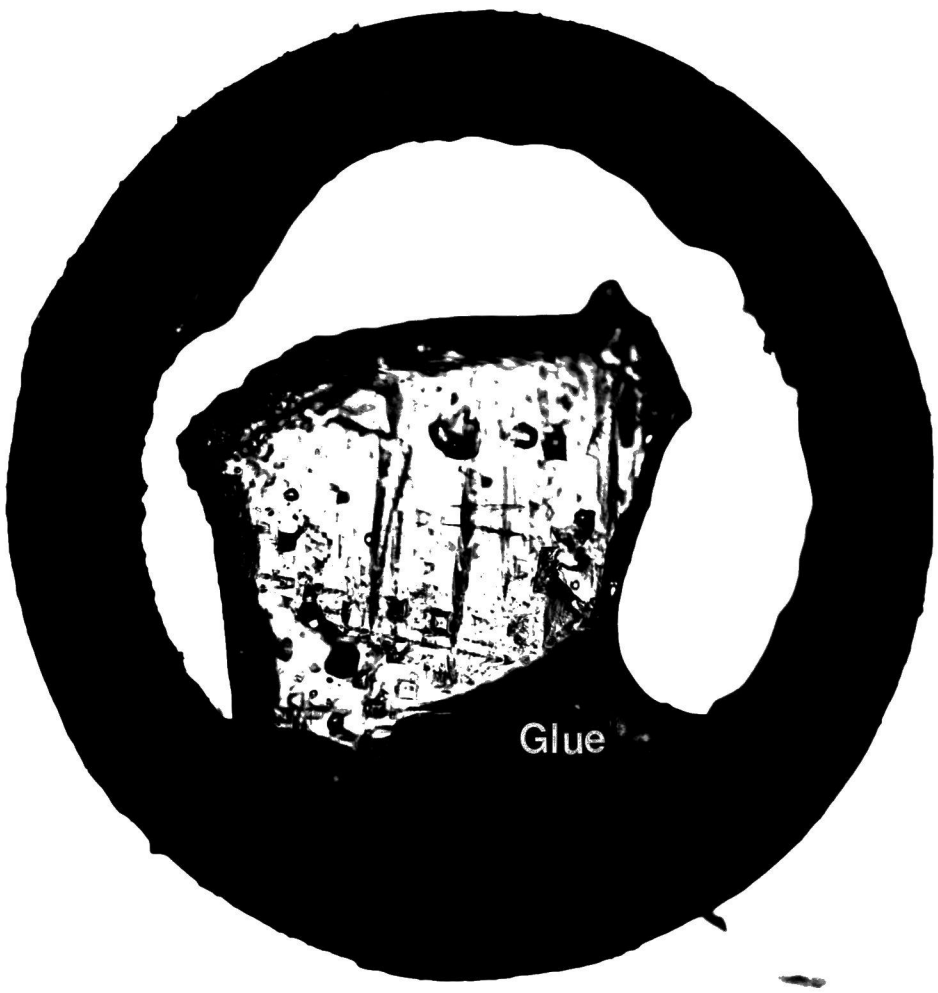

Fig.(6-12) Optical micrograph of a $KCoF_3$ crystal glued with a large amount of varnish.

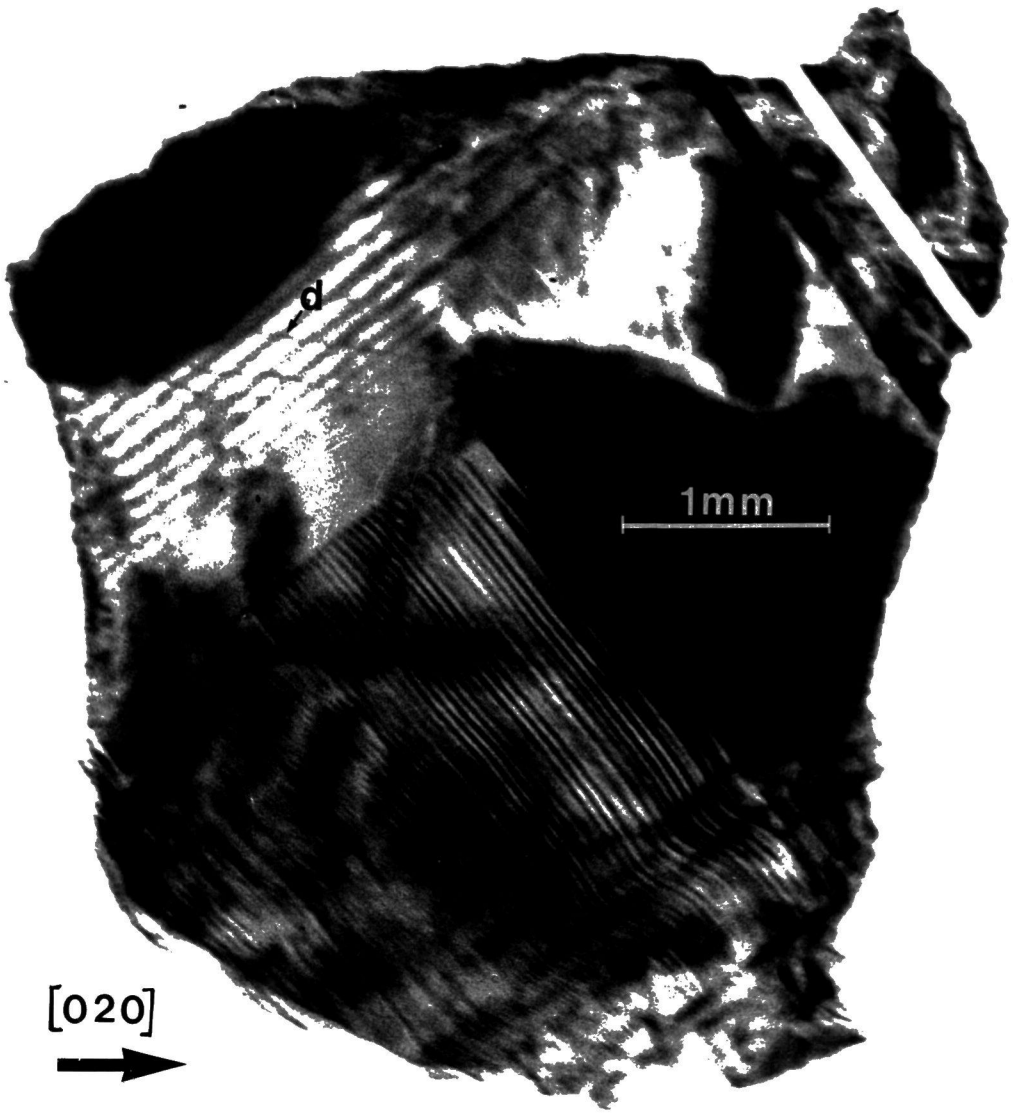

Fig.(6-13) Synchrotron topograph of the same $KCoF_3$ crystal as in Fig.(6-12) at 4.2K. Now a multi-domain configuration is observed. 020 reflection, 7^{o} Bragg angle, 5 Gev, 15mA, 30 seconds exposure.

CHAPTER SEVEN

MAGNETOCRYSTALLINE ANISOTROPY AND THE THEORY OF DOMAIN WALL MOVEMENTS IN CUBIC ANTIFERROMAGNETS

7.1 The Origin of the 4θ-term in the Torque Curves of $KNiF_3$ Crystal

Hirakawa et al. (1961) observed that when $KNiF_3$ crystals were suspended along a crystallographic cube edge, their torque curves could be expressed by the formula,

$$T=C_1H^2\sin 2\theta-C_2H^4\sin 4\theta \qquad (7\text{-}1)$$

in the antiferromagnetic region. Where H is the magnetic field intensity, θ the angle of rotation of H relative to one of the cube axes, and the C's are constants. Later Parkes (1971) also observed a 4θ-term in the torque curves of $KNiF_3$.

It was Nagamiya who first investigated the origin of the 4θ-term in the torque curves of MnO [Uchida, Kondoh, Nakazumi, and Nagamiya (1961)]. He proposed two possible mechanisms, one of which was an intrinsic feature of the crystal and the other was concerned with reversible movements of antiferromagnetic domain walls.

7.1.1 Intrinsic Effect

The total anisotropy energy per unit volume of the cubic crystal consisting of a single domain can be expressed by formula

$$E=K_1(\alpha_1^2\alpha_2^2+\alpha_2^2\alpha_3^2+\alpha_3^2\alpha_1^2)+K_2(\alpha_1^2\alpha_2^2\alpha_3^2)+\cdots\cdots \qquad (7\text{-}2)$$

where the K's are the anistropy constants and α's the direction cosines of the spin axis relative to the three

cubic axes. Neglecting every term except the K_1 and considering the case in which the crystal is suspended along the [001] axis, the energy expression (7-2) is reduced to

$$E = \frac{K_1}{4}\mathrm{Sin}^2(2\varphi) \qquad (7\text{-}3)$$

where φ is the small angle of deflection of the spin axis from the equilibrium position of the x axis Fig.(7-1). If the magnetic field $\underline{H}$ is applied in a direction θ with respect to the x-axis, the free energy per unit volume can be written as

$$F = -\frac{1}{2}\chi_{\perp}H^2\mathrm{Sin}^2(\theta+\varphi)-\frac{1}{2}\chi_{\parallel}H^2\mathrm{Cos}^2(\theta+\varphi)+\frac{1}{4}K_1\mathrm{Sin}^2(2\varphi) \qquad (7\text{-}4)$$

Using the conditions that $\frac{\partial F}{\partial \varphi} = o$ and φ is very small.

$$\varphi = \frac{(\chi_{\perp}-\chi_{\parallel})}{4K_1}H^2\mathrm{Sin}2\theta \qquad (7\text{-}5)$$

Then using the expression (7-4) and (7-5) the torque T can be calculated as:

$$\begin{aligned} T = -\left(\frac{\partial F}{\partial \theta}\right) &= \frac{1}{2}\chi_{\perp}H^2\mathrm{Sin}2(\theta+\varphi)-\frac{1}{2}\chi_{\parallel}H^2\mathrm{Sin}2(\theta+\varphi) \\ &= \frac{1}{2}(\chi_{\perp}-\chi_{\parallel})H^2(\mathrm{Sin}2\theta\mathrm{Cos}2\varphi+\mathrm{Cos}2\theta\mathrm{Sin}2\varphi) \\ &\simeq \frac{1}{2}(\chi_{\perp}-\chi_{\parallel})H^2(\mathrm{Sin}2\theta+2\varphi\,\mathrm{Cos}2\theta) \\ &= \frac{1}{2}(\chi_{\perp}-\chi_{\parallel})H^2\mathrm{Sin}2\theta+\frac{1}{8K_1}(\chi_{\perp}-\chi_{\parallel})^2H^4\mathrm{Sin}4\theta \end{aligned} \qquad (7\text{-}6)$$

The contribution of different kinds of domains to the actual torques of the crystal has been taken into account by Hirakawa et al.(1961) and Parkes(1971). The crystal consists of three kinds of domains in each of which the spin axis is directed along either the x, y or z axis. If the crystal is suspended along the z axis, the z domain is not expected to contribute to the torque in the xy plane.

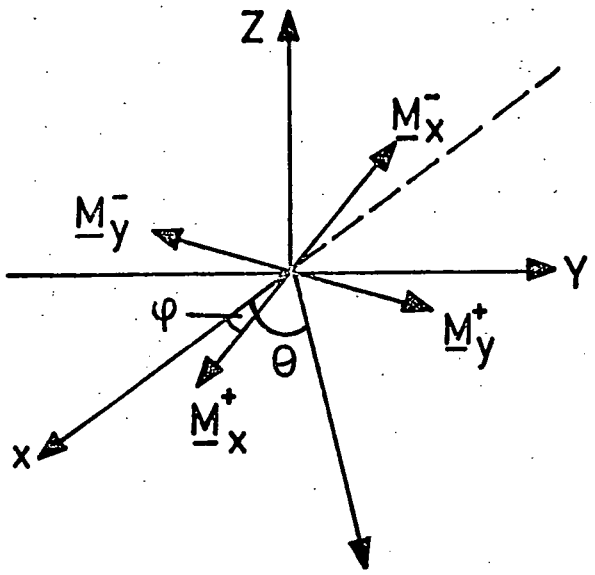

Fig.(7-1) The deflection of the spin axis with respect to the crystal axes in the xy plane by the application of a magnetic field.

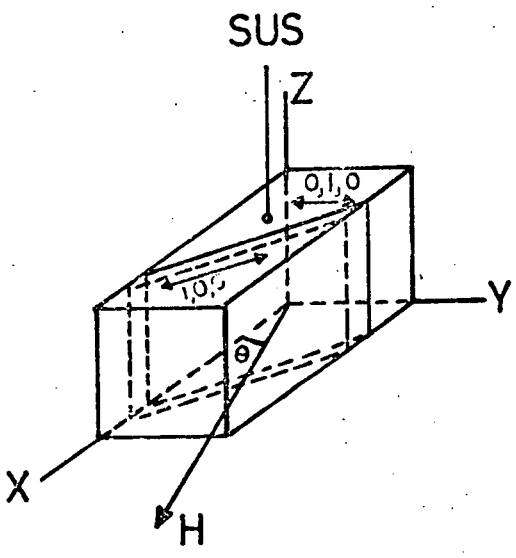

Fig.(7-2) The spin directions in two different kinds of domain. The dotted line shows the displacement of an antiferromagnetic domain wall by the application of a magnetic field. After Hirakawa et al. (1961).

Since in the antiferromagnetic state the sublattice magnetizations along the ±x axes are expected to remain collinear, for the sublattice along -x, the same expression for φ is obtained on minimizing the free energy. This indicates that the total energy is also a minimum. Therefore the total torque for this domain is

$$T_x = (\chi_\perp - \chi_{||})H^2 \sin 2\theta + \frac{1}{4K_1}(\chi_\perp - \chi_{||})^2 H^4 \sin 4\theta \qquad (7\text{-}7)$$

A similar treatment could be applied for y domains, but because of an effective change of 90° in the applied field direction, a change of sign of the 2θ-term in the expression of the torque results.

$$T_y = -(\chi_\perp - \chi_{||})H^2 \sin 2\theta + \frac{1}{4K_1}(\chi_\perp - \chi_{||})^2 H^4 \sin 4\theta \qquad (7\text{-}8)$$

If e, f and g are the fractions of x, y, and z domains respectively

$$T_x + T_y = (e-f)(\chi_\perp - \chi_{||})H^2 \sin 2\theta + \frac{e+f}{4K_1}(\chi_\perp - \chi_{||})^2 H^4 \sin 4\theta \qquad (7\text{-}9)$$

where $e+f+g = 1$.

As seen the calculated torque based on an intrinsic crystal effect consists of 2θ and 4θ-terms. According to (7-9), for a crystal having equal volumes of the three kinds of domains ($e=f=g=\frac{1}{3}$), the 2θ contribution to the torque will disappear. As seen in the calculated torque expression (7-9) the 4θ-term is of positive sign. Hirakawa et al. therefore concluded that the proposed intrinsic mechanism was not responsible for the observed 4θ-term in $KNiF_3$. Parkes (1971), allowing for the domain distribution, attempted to fit his results at low fields

to the above intrinsic mechanism and estimated the value of magnetocrystalline anisotropy, $K_1 = 3 \times 10^3 \text{erg/gm} = 1.2 \times 10^4 \text{erg/cm}^3$ He pointed out that this is an approximation to the equal distribution of three kinds of domains, $(e+f=\frac{2}{3})$, and should be checked on an annealed, single domain crystal. Unfortunately, there is an error in the calculations of the torque expression in Parkes' thesis, and the sign of the 4θ-term should be positive. However, it is not clear whether this affects the conclusion as the Fourier coefficients are by definition all positive (square root of sums of squares) and it is not possible to determine the relative phase of the 2θ and 4θ components unambiguously. This criticism can also be applied to Hirakawa et al.'s work as in the (001) plane the [100] and [010] directions are equivalent. The torque data are ambiguous on this point and when two types of domains are introduced, (e-f) in the torque expression (7-9) can have either + or - sign depending on the relative numbers of x and y domains. One cannot determine from the torque data whether or not the intrinsic mechanism is operating.

7.1.2 Movement of Domain Walls

As we saw in section (1-3), in antiferromagnets the susceptibility is larger when the spins lie perpendicular to rather than parallel to the field and hence the total energy of the system is minimized for the perpendicular orientation of the spins. Néel (1953) suggested that in an increasing applied field domain wall motion occurs in such a way that one of the domains whose spin axis is more

nearly perpendicular to the field will expand by domain wall movement. On the other hand, the wall will experience an elastic restoring force so that it will settle at a new equilibrium position. This kind of restoring force may result from magnetic anisotropy.

Let us apply Néel's idea to the problem of movement of the walls in a magnetic field. Assuming the direction cosines of spin axes in one domain are (α,β,γ) with respect to the cubic axes, the free energy per unit volume due to the interaction with the applied field can be written as,

$$F = -\frac{1}{2}\chi_{\parallel}H_{\parallel}^2 - \frac{1}{2}\chi_{\perp}H_{\perp}^2 = \frac{1}{2}(\chi_{\perp}-\chi_{\parallel})H^2(\alpha a+\beta b+\gamma c)^2-\frac{1}{2}\chi_{\perp}H^2 \qquad (7\text{-}10)$$

Here (a,b,c) are the direction cosines of the applied magnetic field with respect to the cube axis. We can assume that the direction cosines of the spins in the other domain are (α',β',γ'). The domain boundary wall shifts by a distance x, enlarging the domain in which the spin axis is more nearly perpendicular to the field and diminishing the other domain in which the spin axis is more nearly parallel to the field. Then the variation in the free energy per unit area is given by

$$F = \frac{1}{2}x(\chi_{\perp}-\chi_{\parallel})H^2\left[(\alpha a+\beta b+\gamma c)^2-(\alpha' a+\beta' b+\gamma' c)^2\right] \qquad (7\text{-}11)$$

According to Néel's idea, there is a restoring force resisting domain wall motion due, presumably, to the magnetocrystalline anisotropy. This leads to a force -Cx on the wall and a free energy contribution

$$+\frac{Cx^2}{2} \qquad (7\text{-}12)$$

where C is the force constant of the restoring force which acts on the domain walls. Adding (7-11) and (7-12) and minimizing the total energy, we have

$$x = -\frac{1}{2C}(\chi_{\perp} - \chi_{\parallel})H^2\left[(\alpha a+\beta b+\gamma c)^2-(\alpha' a+\beta' b+\gamma' c)^2\right] \qquad (7\text{-}13)$$

Substituting this x into the total energy increase per unit area, we have

$$\Delta F_T = -\frac{1}{8C}(\chi_{\perp} - \chi_{\parallel})^2H^4\left[(\alpha a+\beta b+\gamma c)^2-(\alpha' a+\beta' b+\gamma' c)^2\right]^2 \qquad (7\text{-}14)$$

As can be seen this change in the total energy is quartic in a, b, and c. Hirakawa et al. considered that the crystal consists of two kinds of domains in each of which the direction cosines of the spin axis relative to cubic axes are 0,1,0 and 1,0,0, Fig.(7-2). The torque equation around the [001]-axis of such a crystal, when movements of domain walls are taken into account, can immediately be obtained by substituting these numerical values of the direction cosines into equation (7-14)

$$T = -\frac{1}{4C}(\chi_{\perp} - \chi_{\parallel})^2H^4\sin 4\theta \qquad (7\text{-}15)$$

This equation is given in terms of torque per unit area of domain wall. In order to compare it with the actual case, the right hand side of (7-15) should be multiplied by a constant A of positive sign, related to the total area of the domain walls. Thus the torque expression can be written as:

$$T = -\frac{A}{4C}(\chi_{\perp} - \chi_{\parallel})^2H^4\sin 4\theta \qquad (7\text{-}16)$$

Hirakawa et al. (1961) reported that this equation for the 4θ-term was qualitatively consistent with the observed torque of $KNiF_3$ in sign (for temperatures $<$ 200K). Also

when they applied an increasing external stress along one of the cubic axes, they observed that the amplitude of the 2θ-term grew large and the 4θ-term diminished completely. They suggested that the specimen becomes nearly a single domain crystal upon applying the stress.

7.2 Further remarks on Domain Wall Movements

Here we study the simple case of $\underline{H}$ parallel to [001], therefore in equation (7-11), a=b=0, c=1. Consider a displacement x of the wall between a d_z domain and d_x or d_y domains, which corresponds to a rotation of the spins from the ($\alpha=\beta=0$, $\gamma=1$) to the (α', β', $\gamma'=\cos\phi$) direction. Then the variation of free energy per unit area can be written as:

$$\Delta F = -\frac{1}{2}x(\chi_{\perp} - \chi_{||})H^2\sin^2\phi \qquad (7\text{-}17)$$

The spectroscopic experiments of Petit et al.(1975) and the direct observations of domain wall movements in $KNiF_3$ and $KCoF_3$ in the present work (Chapter 8) seem to show that not only is there a restoring force -Cx resisting domain wall motion (presumably due to the magnetocrystalline anisotropy), but there is also a viscous drag on the wall due to a coercive force $B\sin^2\phi$. The free energy contribution due to this coercive force per unit wall area is then

$$xB\sin^2\phi \qquad (7\text{-}18)$$

Then the total variation of free energy will be

$$\Delta F = -\frac{1}{2}x(\chi_{\perp} - \chi_{||})H^2\sin^2\phi + \frac{Cx^2}{2} + xB\sin^2\phi \qquad (7\text{-}19)$$

Stability will occur, if we minimize ΔF with respect to

x and ϕ , that is

$$\frac{\partial \Delta_F}{\partial \phi} = 0 \longrightarrow \phi = \frac{\pi}{2} + n \qquad (7\text{-}20)$$

and,

$$\frac{\partial \Delta_F}{\partial x} = 0 \longrightarrow -\frac{1}{2}(\chi_\perp - \chi_{||})H^2 + Cx + B = 0 \qquad (7\text{-}21)$$

i.e. $$H = \left[\frac{2(Cx+B)}{\chi_\perp - \chi_{||}}\right]^{\frac{1}{2}} \qquad (7\text{-}22)$$

Movement only occurs when $x>0$, therefore if $H<(\frac{2B}{\chi_\perp - \chi_{||}})^{\frac{1}{2}}$ no movement will occur. We can define a threshold field given by

$$H_{th} = (\frac{2B}{\chi_\perp - \chi_{||}})^{\frac{1}{2}} \qquad (7\text{-}23)$$

and substituting the value of B from (7-23) into (7-22) we obtain

$$x = (\frac{H^2 - H_{th}^2}{2C})(\chi_\perp - \chi_{||}) , \qquad (7\text{-}24)$$

At the critical field, H_{cr}, x=L= the domain spacing, and therefore the equation (7-24) can be written as:

$$H_{cr}^2 - H_{th}^2 = (\frac{2CL}{\chi_\perp - \chi_{||}}) , \qquad (7\text{-}25)$$

Using equations (7-24) and (7-25) we find the wall displacement x is given by

$$x = L(\frac{H^2 - H_{th}^2}{H_{cr}^2 - H_{th}^2}) \qquad (7\text{-}26)$$

If we assume that no domain wall movement occurs and that at a certain critical field H_f spin flop takes place, then according to equation (1-28) H_f is given by

$$H_f = \left(\frac{2K}{\chi_\perp - \chi_{||}}\right)^{\frac{1}{2}} \qquad (7\text{-}27)$$

In the case of domain wall movement, equation (7-25) was obtained. For an ideally perfect crystal ($H_{th} = 0$) this equation is formally the same as (7-27) if we replace K by CL, but it is important to note that the mechanisms involved in each differ markedly. CL, which must be somehow related to the magnetocrystalline anisotropy, can be called the effective anisotropy. However the actual relation between the restoring force and anisotropy is not clear.

Application of external stress along one of the cubic axes can also cause domain wall movements in cubic antiferromagnets. Using stress linear dichroism, Pisarev et al.(1972) and Ferré et al.(1976) have investigated the magnetic origin and evidence for domain wall movements in $KNiF_3$, $KCoF_3$ and $RbCoF_3$ under external stresses. They have suggested that stress applied along one of the $\langle 100 \rangle$ directions changes the magnetoelastic energy of the crystal and that re-orientation of spins takes place when the anisotropy and magnetoelastic energies are of the same order of magnitude. In this case the total change of free energy due to the displacement x of the wall can be obtained by adding the general expressions of magnetoelastic energy to the restoring energy,

$$F = -\frac{3}{2}\lambda_{100}\sigma x + \frac{Cx^2}{2} \qquad (7\text{-}28)$$

where σ is the magnitude of stress applied along the cube edge. Minimizing this total change of free energy with

respect to x we obtain:

$$x = \frac{3}{2C}\lambda_{100}\sigma \qquad (7\text{-}29)$$

The size of the d_z domains increases at the expense of the d_x or d_y domains and therefore the wall moves linearly with stress. Eventually, at the critical stress only d_z domains remain and x reaches the value L of domain spacing, and equation (7-29) can be written as:

$$\sigma_{cr} = \frac{2\,CL}{3\lambda_{100}}\,, \qquad (7\text{-}30)$$

Ferré et al.(1976) noticed that their two sets of spectroscopic results for the application of magnetic field and stress were consistent. By using expressions (7-30) and (7-25) and neglecting H_{th} for an ideally perfect crystal the following relation can be obtained:

$$H_{cr} = \left(\frac{3\lambda_{100}\sigma_{cr}}{\chi_{\perp} - \chi_{\parallel}}\right)^{\frac{1}{2}} \qquad (7\text{-}31)$$

Using the value of critical stress from their experiments on $KNiF_3$, and assuming $\lambda_{100} \leqslant 10^{-5}$ (Nouet 1973), from equation (7-31) they obtained $H_{cr} < 10$KOe.Considering the fact that they had not taken the threshold field H_{th} into account, and that the two sets of stress and field experiments were performed on different samples, they found that the two sets of experimental results were consistent.

CHAPTER EIGHT

EXPERIMENTAL OBSERVATIONS OF DOMAIN WALL MOVEMENTS

8.1 The Apparatus

As we saw in Chapter Five, the availability of synchrotron radiation enabled low temperature topographic experiments to be performed in magnetic fields up to 14 KOe. In these experiments the applied field was increased in small steps in order to follow the movements of the walls. In order to avoid health hazards the beam area must be searched and interlocked prior to each exposure. This procedure takes a few minutes, whereas the actual exposure times are typically 10 seconds for a beam current of 15mA, at 5 Gev. The step by step experiments usually comprised 20 successive exposures in different fields. It was a laborious and time consuming job to search and interlock the beam area for each topographic exposure. By mounting six nuclear emulsion plates on a motor driven wheel inside a lead lined light tight box, Fig.(8-1), the plates could be changed remotely without entering the beam area. Thus the experimental time was reduced significantly. The current through the magnet was changed from outside the beam area, thus for each exposure the magnetic field could be controlled remotely. Topographs were taken in sequence as the field was raised in steps of about 0.5 KOe.

8.2 Domain Wall Movement in $KNiF_3$

The magnetic field studies were performed on a highly

Fig.(8-1) Remote control camera for sequential synchrotron topography. Six nuclear emulsion plates, F, are mounted on a motor driven wheel. These can be rotated by operating the relay box, R, so that each plate appears sequentially behind the X-ray window W. The lead plate L prevents the beam fogging the plates.

perfect $KNiF_3$ crystal, Fig.(4-3). It was found that on cooling through T_N the domain pattern could be influenced by fields as low as 0.1 KOe. This is consistent with the fact that near T_N the spins easily orient themselves perpendicular to a small magnetic field. For a field applied along [010], walls between domains with spins parallel to [001] and [100] predominate. The susceptibility is larger when the spins are perpendicular rather than parallel to the field and hence the total energy of the system is minimized. Petit et al. (1975) also noticed this effect in their indirect domain wall studies in $KNiF_3$.

The first sequence of topographs was taken in steps of increasing magnetic field up to 13 KOe at 100K using the glass cryostat with cold finger. The residual field of the electromagnet for a gap of 2.5 cm was 0.2 KOe. The crystal was cooled in the absence of a magnetic field and then the cryostat was mounted on the electromagnet. The field direction was horizontal and parallel to [010]. As seen in Fig.(8-2a), the domain configuration comprised of three sets of walls running in [010] and $[0\bar{1}1]$ directions. Fig.(8-2) shows that as the field is increased, a significant domain wall motion takes place. The [010] walls are between domains already perpendicular to the field. As expected, they do not move. The $\langle 011 \rangle$ oriented walls do not move until a threshold field H_{th} is passed. Thereafter they move continuously as the field is increased. At a critical field H_{cr} these walls disappear completely from the crystal. In this experiment the threshold field was found to be 1 ± 0.2 KOe and the critical field 4 ± 0.5 KOe.

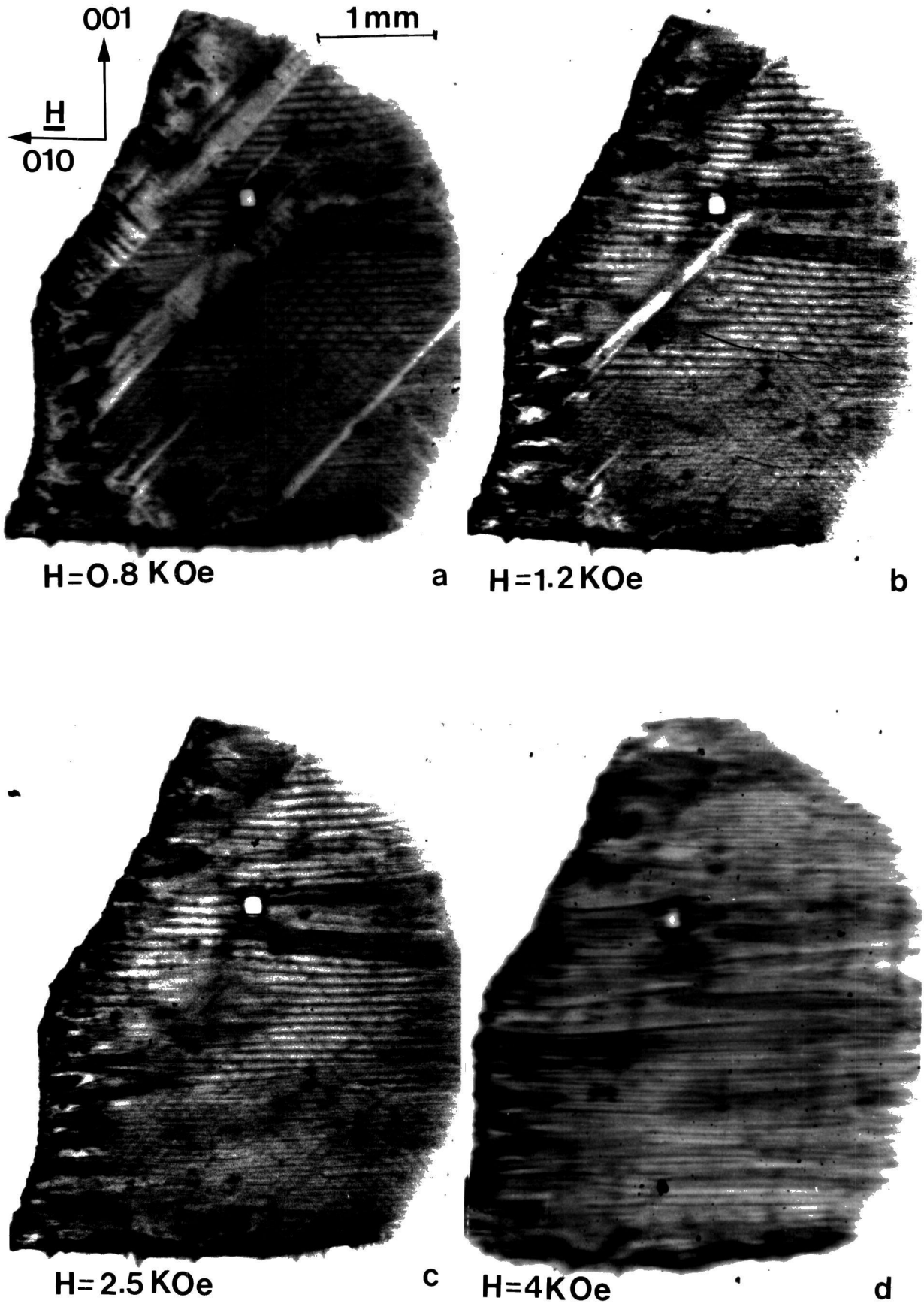
001
1mm
H
010
H=0.8 KOe
a
H=1.2 KOe
b
H=2.5 KOe
c
H=4KOe
d

Fig.(8-2) Synchrotron topographs of antiferromagnetic domains in $KNiF_3$ at 100K in increasing field steps applied parallel to [010]. Diffraction from (001) planes with a Bragg angle of 5^{o}. 4 Gev, 15 mA, 10 seconds exposure on Ilford L4, 25 μm emulsion. As the field is increased the $\langle 011 \rangle$ oriented walls gradually move and in H = 4 KOe all of them disappear. No movement of [010] oriented walls.

Fig.(8-3) shows another series of topographs taken at 4.2K in increasing field steps. In this series of micrographs we can follow the movement of the two sets of $\langle 011 \rangle$ oriented walls. The data for this run show that the threshold and critical fields were 2.2±0.2 KOe and 4.5±0.5 KOe respectively. When all the $\langle 011 \rangle$ oriented walls moved as shown in Fig.(8-3e), while the crystal was still at 4.2K, the current through the magnet was decreased to zero (H=0.1 KOe for a gap of 5 cm between the pole pieces of the electromagnet). Then in this condition another topograph was taken, Fig.(8-3f). As seen, again the $\langle 011 \rangle$ walls were nucleated only in the region X, and the domain pattern is not exactly the same as in Fig.(8-3a). Here one may suggest that the domain wall movement up to a certain distance is a reversible mechanism. While the specimen was still at 4.2K, the crystal was rotated through 45° in the vertical plane. The field direction was then parallel to $[011]$. In this condition, topographs were taken sequentially as the field was increased, Fig.(8-4). Now the field can exert a force on the $[010]$ oriented walls and cause their movements. As expected the $[011]$ oriented walls which are parallel to the field direction remain immobile.

Equation (7-10) predicts that for the $[011]$ oriented magnetic field, the magnitude of the effective field exerting force on $[010]$ oriented walls should be $(2)^{\frac{1}{2}}$ times its magnitude in the case of a $[010]$ oriented field. Therefore we can write

$$H_{cr\,[011]} = 1.4 H_{cr\,[010]} \qquad 8\text{-}1$$

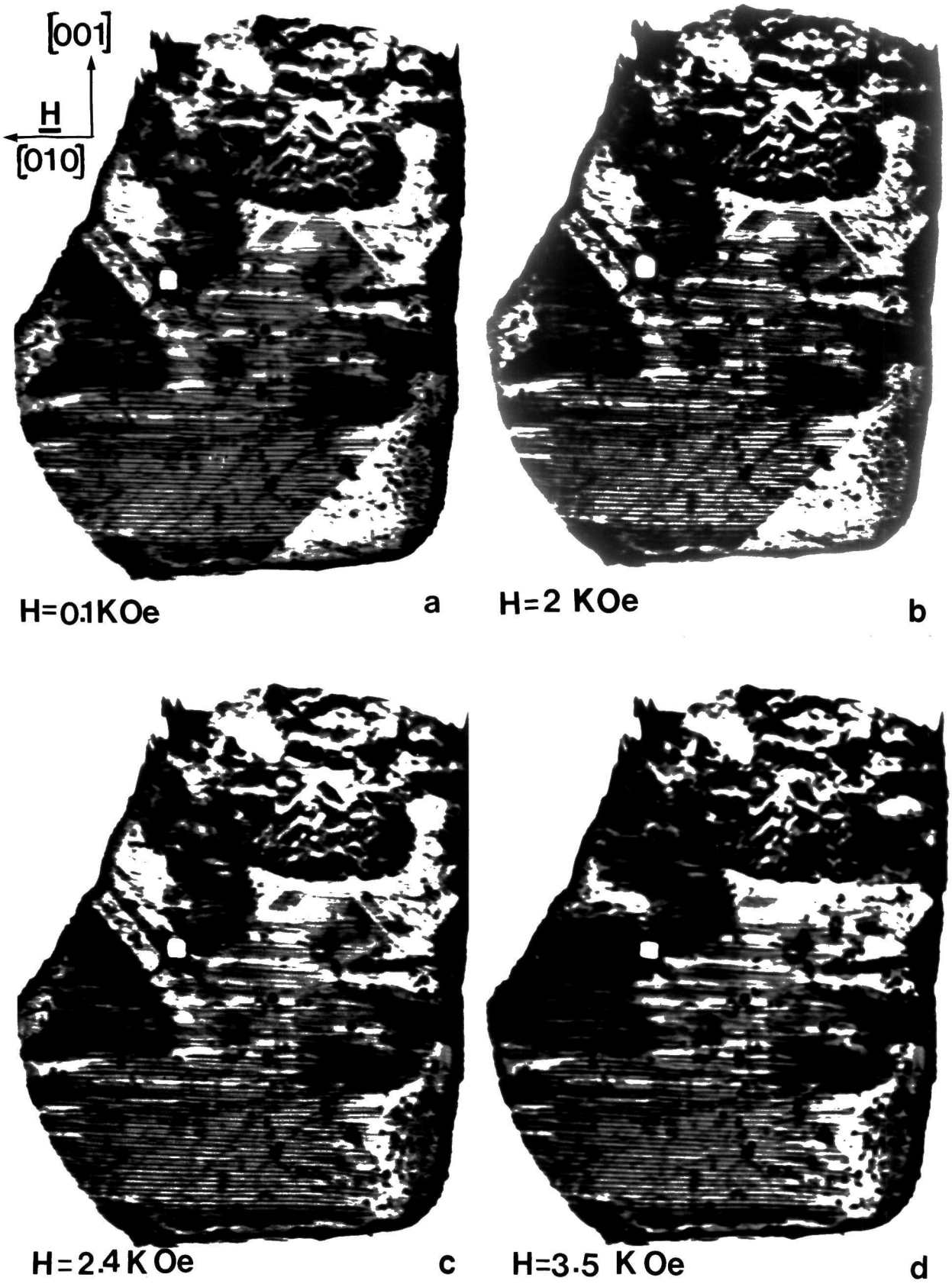
[001]
H
[010]
H=0.1KOe
a
H=2 KOe
b
H=2.4 K Oe
c
H=3.5 K Oe
d

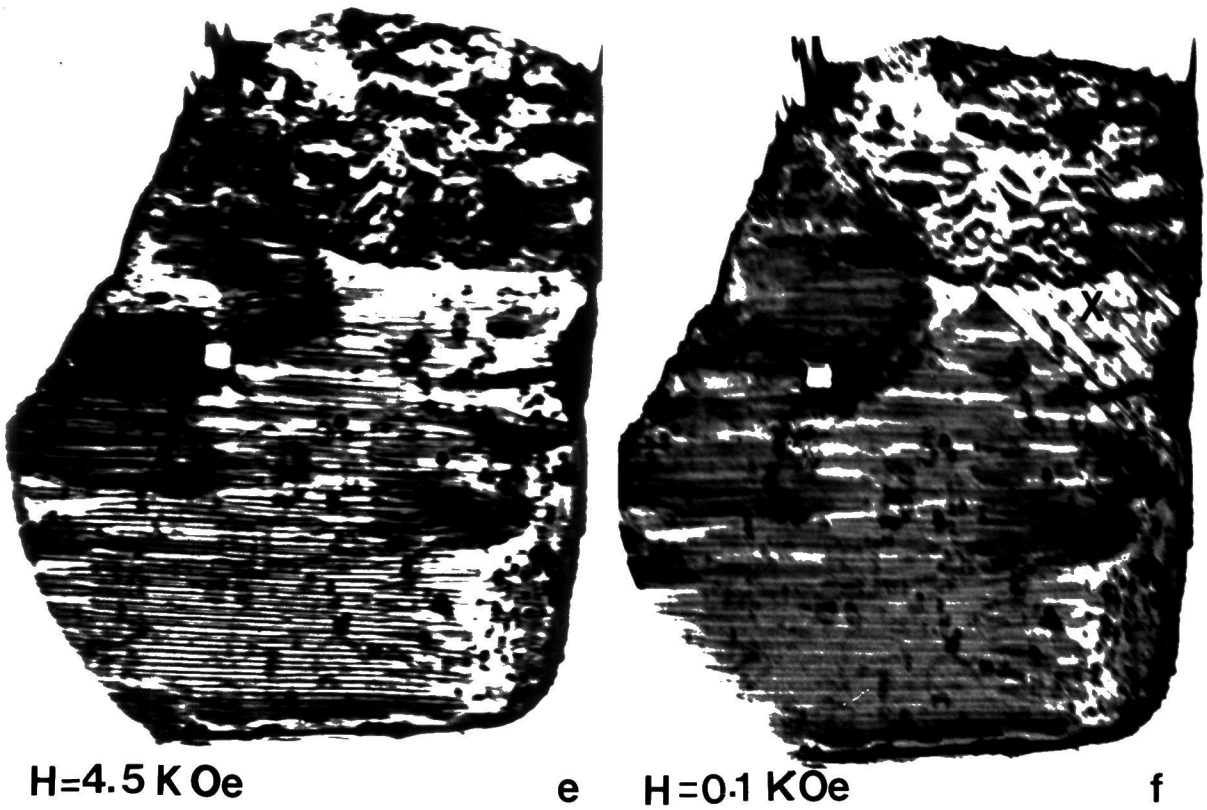

Fig.(8-3) Synchrotron topographs of the same crystal of $KNiF_3$ at 4.2K in increasing steps of field applied parallel to [010]. Diffraction from (001) planes with a Bragg angle of 8°. 4 Gev, 10 mA, 20 seconds exposure. Movement of the $\langle 011 \rangle$ oriented walls can be observed.

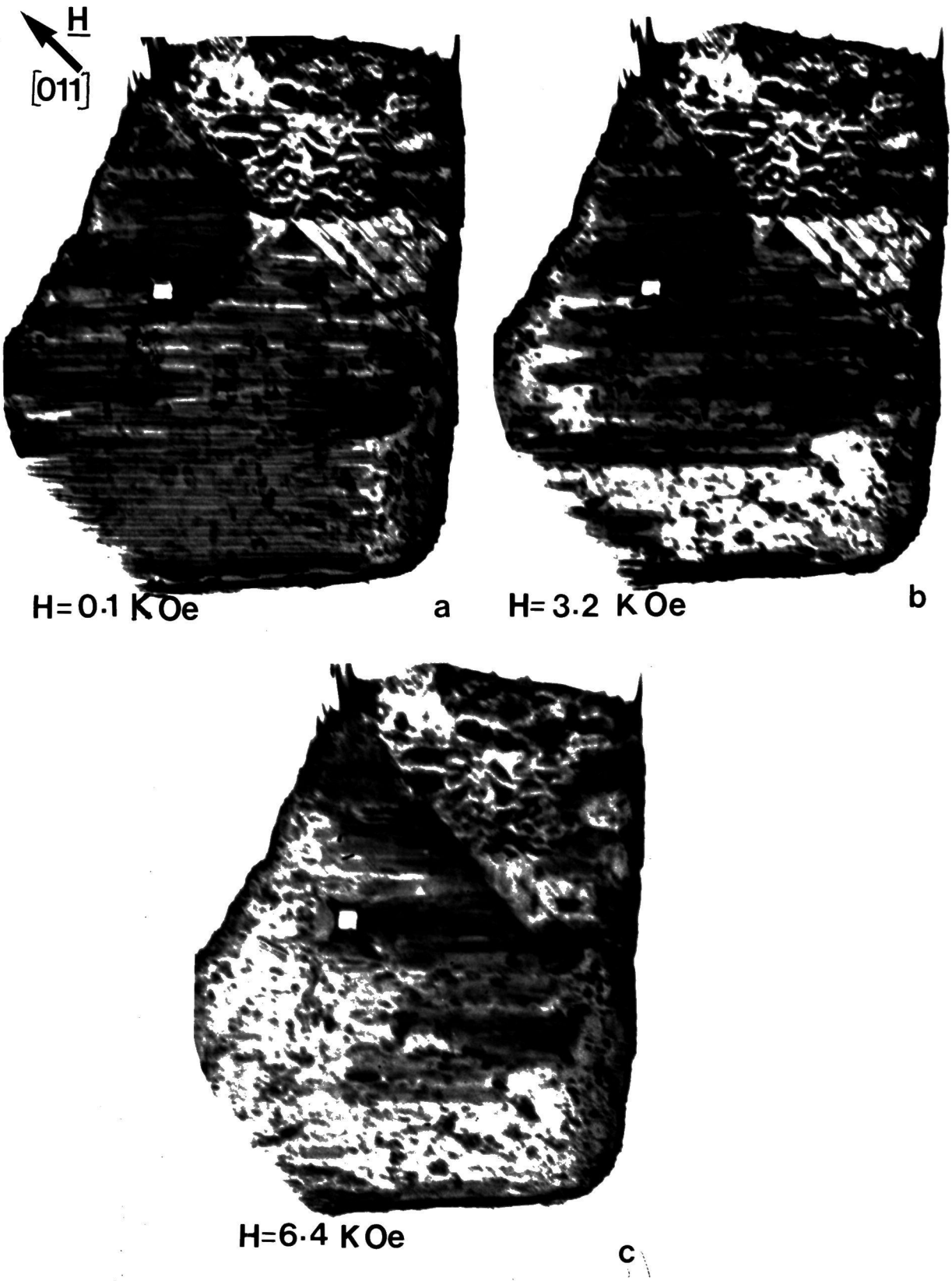

Fig.(8-4) Synchrotron topographs of the same crystal of $KNiF_3$ at 4.2K when the crystal was rotated 45° in the vertical plane. Now the magnetic field was applied parallel to [011]. As the field increased the [010] oriented walls started to move.

and

$$H_{th}[011] = 1.4 H_{th}[010] \qquad 8\text{-}2$$

Fig.(8-4) shows that the [010] oriented walls started to move at $H_{th}=3.3\pm0.2$ KOe. Because of the relatively wide tail of the Meric cryostat (5 cm), only the maximum field of 6.4 KOe at the specimen could be achieved. However Fig.(8-4c) shows that all the [010] oriented walls in the lower part of the specimen have moved in this field and the critical field could be estimated to be 6.5 ± 0.5 KOe. This experiment provides further direct verification of Néel's theory. The values of H_{cr} and H_{th} in the [011] and [010] oriented field experiments are in agreement with the predicted results, equations (8-1) and (8-2). Table (8-1) shows the values of H_{cr} and H_{th} obtained in different cooling runs.

8.3 Domain Wall Movements in $KCoF_3$

Domain wall movements in $KCoF_3$ were followed in fields up to 14 KOe at 77K. A $KCoF_3$ crystal, Fig.(4-8), was mounted very carefully with only a very small amount of varnish at one corner. As seen in Fig.(8-5) the domain configuration consists of only one domain wall.

The single domain wall configuration is an interesting case for domain wall motion studies. In this case one is able to follow the movement and the position of the wall in an increasing field over a large distance. Fig.(8-5) shows a series of topographs of the $KCoF_3$ crystal taken in steps of fields up to 14 KOe. The field direction is parallel

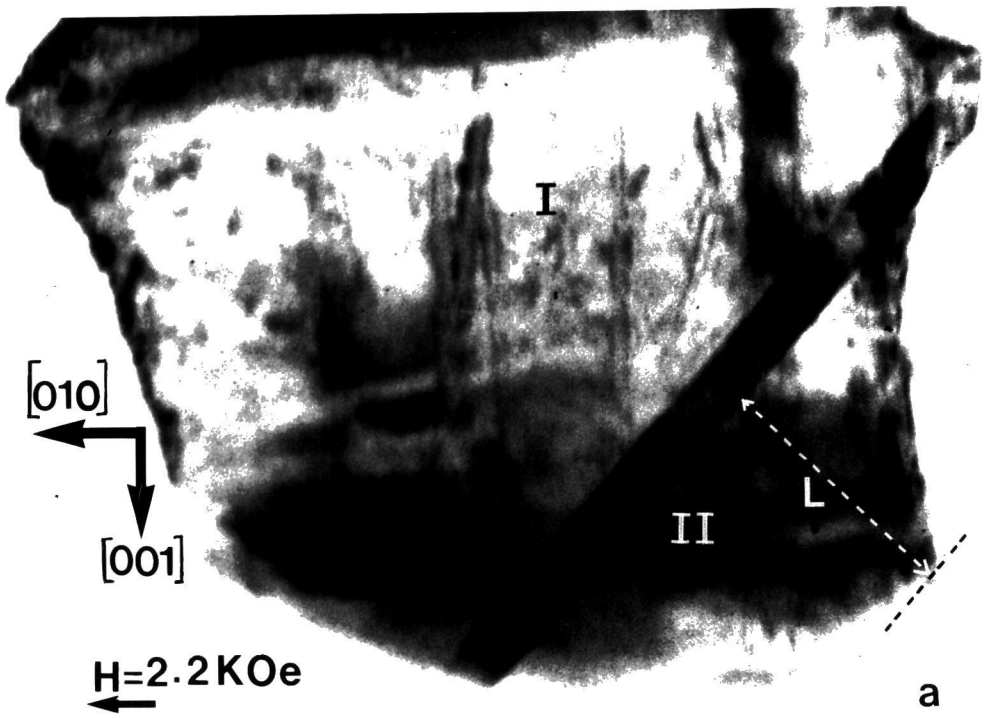

a

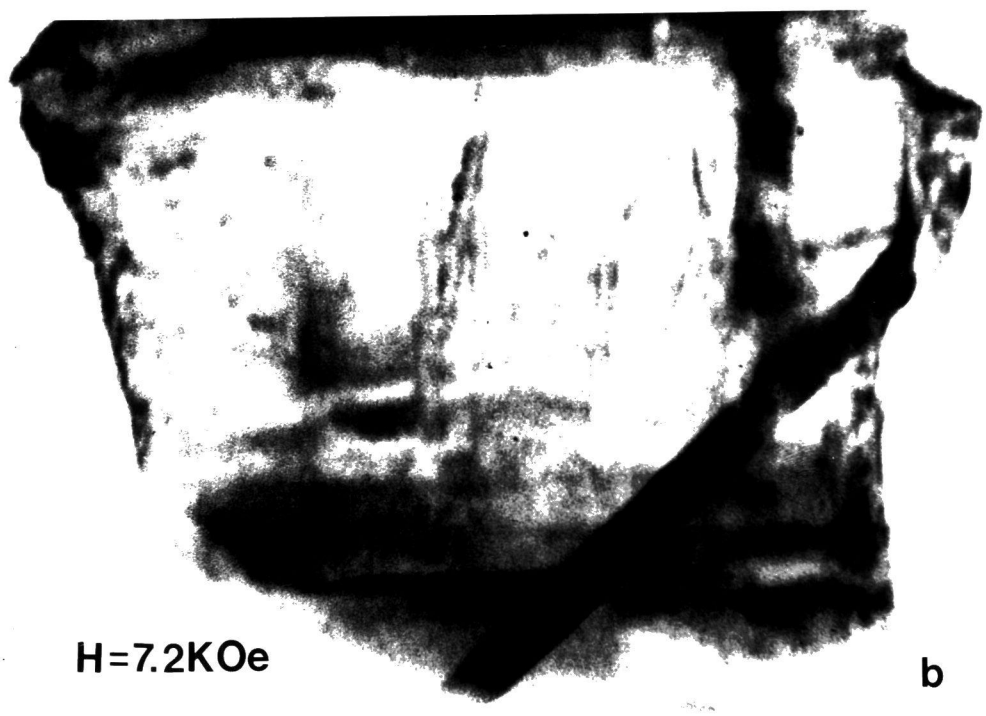

b

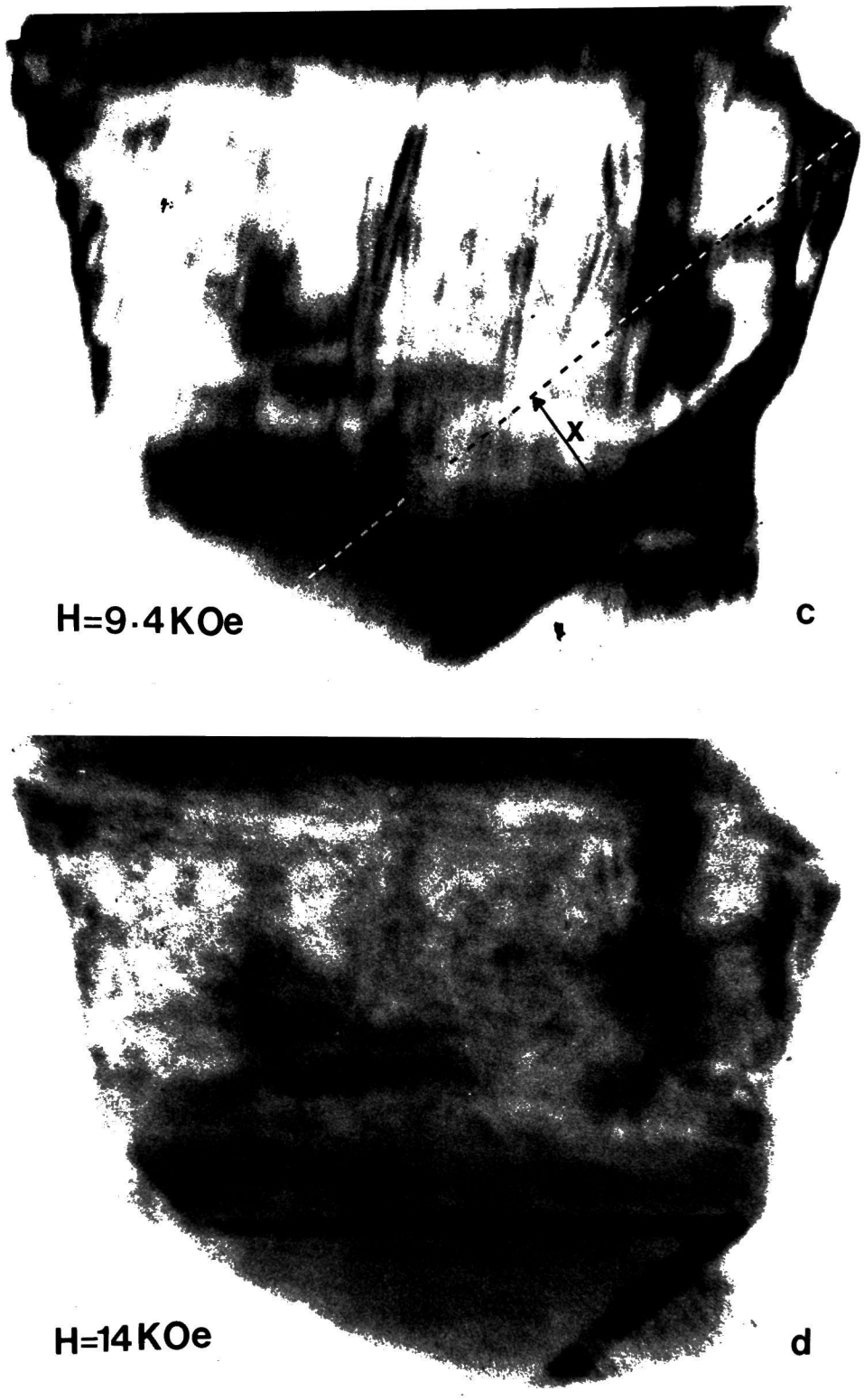

Fig.(8-5) Movement of an antiferromagnetic domain wall in $KCoF_3$ in different fields up to 14 KOe at 77K. Synchrotron topographs, (010) reflecting planes, 5^{o} Bragg angle, 4 Gev, 5mA, 7 minutes exposure on Ilford L4, 25μm Nuclear emulsion.

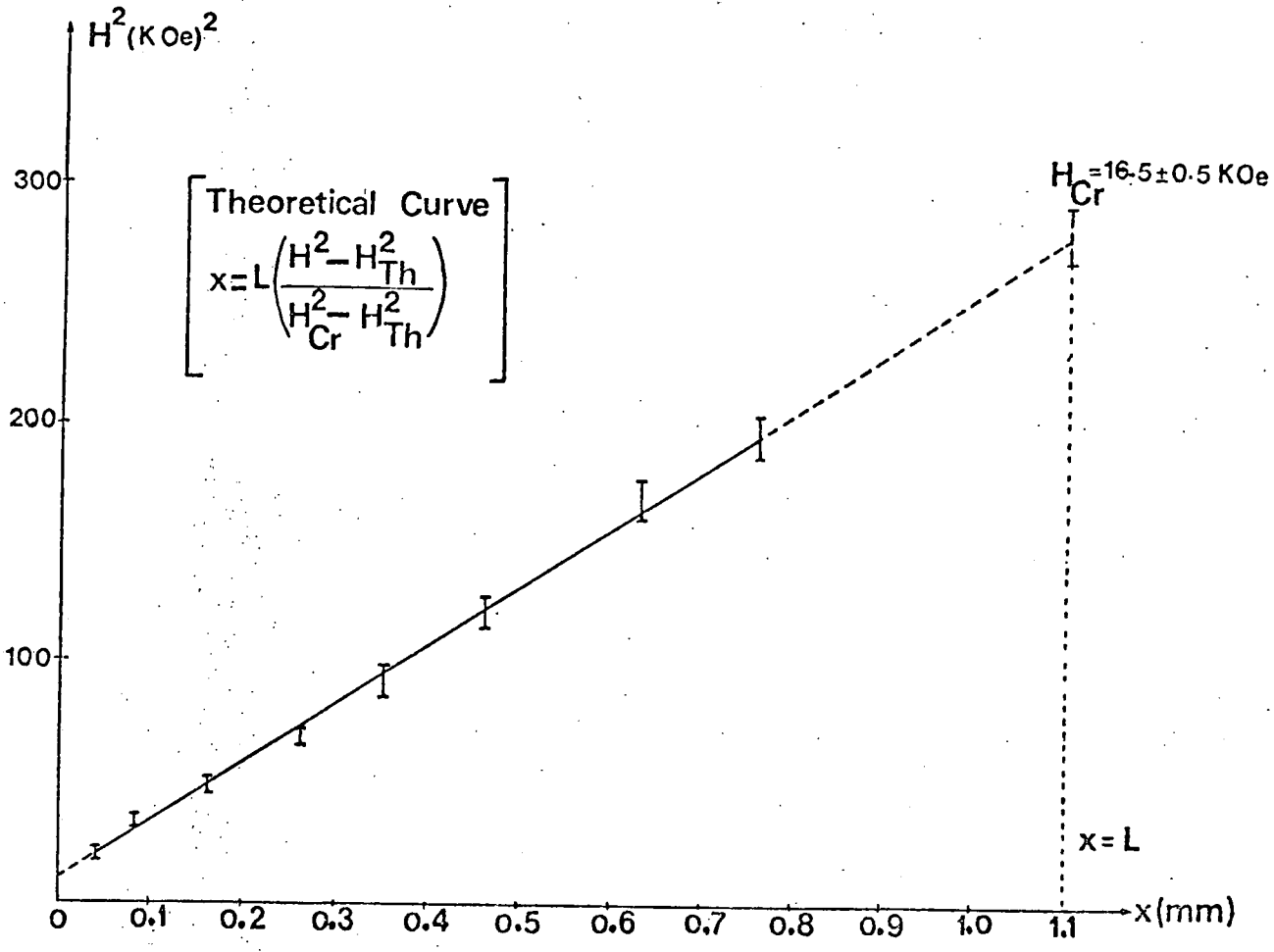

Fig.(8-6) Domain wall position in a $KCoF_3$ crystal as a function of H^2. The displacement of the wall shown in Fig.(8-5) was measured in a sequence of topographs taken in increasing field steps.

to [010]. The wall movement is clearly visible. This experiment shows that as the field increases, the volume of the domain I increases at the expense of the domain II, and eventually at the critical field, the whole specimen becomes single domain with spins perpendicular to the field direction. In Fig.(8-5d) the wall has nearly disappeared from the crystal. This topograph was taken at the maximum available field.

Using Néel's theory, the displacement of the wall is given by equation (7-25), $x=L(H^2-H_{th}^2)/(H_{cr}^2-H_{th}^2)$. The position of the wall was measured in all topographs which were taken in different fields. Fig.(8-6) shows the plot of the domain wall displacement versus H^2. This plot shows very good agreement with the theoretical prediction. The critical field and the threshold field are estimated by extrapolation. At the critical field the wall disappears, that is, the displacement x equals the initial distance (L) of the wall from the corner of the crystal. Domain movement studies on the same crystal with a multi-domain configuration revealed that, within the experimental error, the magnitudes of the critical field and the threshold field were independent of the domain configuration. The field magnitudes were approximately the same as in the case of the one domain wall configuration, Table (8-2).

8.4 The Reversibility of the Domain Wall Movements in $KCoF_3$

In order to investigate the reversibility of the domain walls, a series of topographic experiments were performed in such a way that the field was alternately raised and

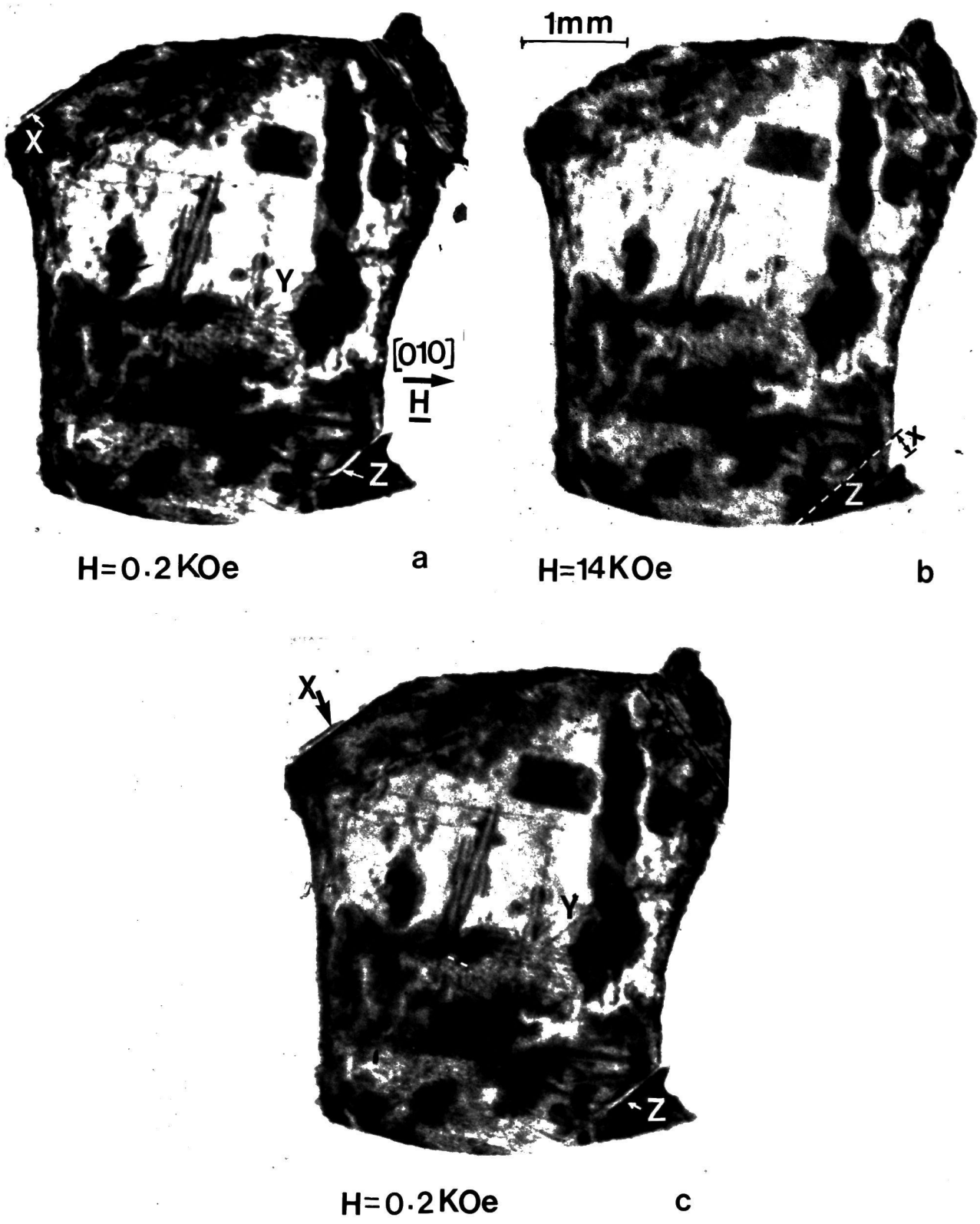

Fig.(8-7) Reversible movements of domain walls in a crystal of $KCoF_3$ at 77K. Synchrotron topographs, (010) reflecting planes, 7° Bragg angle, 4 Gev, 10mA, 7 minutes exposure.

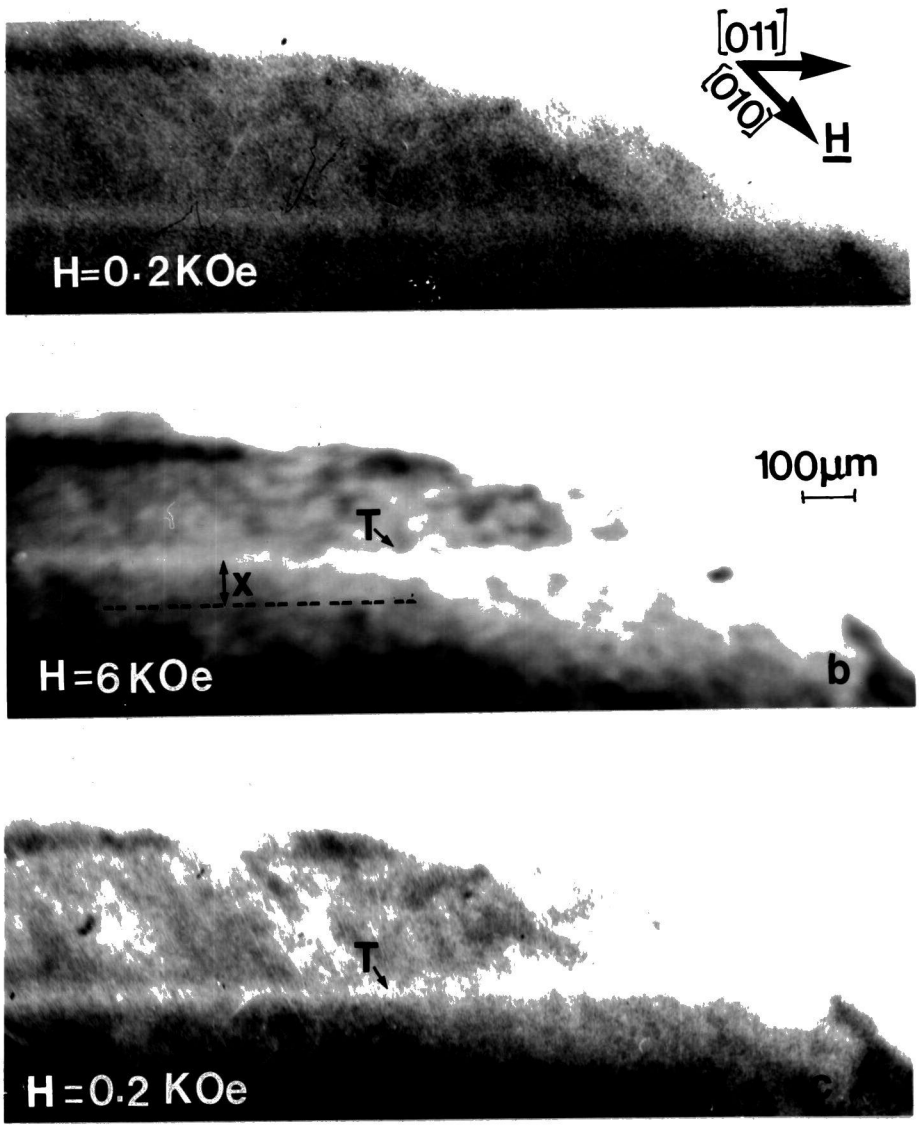

Fig.(8-8) Reversible movement of a domain wall in an enlarged part of the same $KCoF_3$ crystal at 77K. Synchrotron topographs, (010) reflecting planes, 7^{o} Bragg angle, 4 Gev, 10mA, 7 minutes exposure.

switched off. Fig.(8-7a) was taken in H=0.2 KOe, and Fig.(8-7b) was taken after the field was increased to H=14 KOe. As seen the walls X and Y disappear, and the wall Z moves towards the corner of the crystal. Now the current through the magnet was switched off and another topograph was taken, Fig.(8-7c). Again the walls X and Y appear, and the wall Z moves back to its original position. Fig.(8-8) shows the enlargement of one part of the crystal in which the domain wall motion has been studied. By applying a field of H=6 KOe the wall T moves towards the edge of the crystal, and again on removing the field the wall returns to its original position. As soon as the magnetic field is switched off, the restoring force -Cx which resists the wall movement pushes the wall to its original position. The reversibility of the wall movement demonstrate that a long range restoring force is indeed operating.

8.5 Susceptibility Measurements on Single Crystal of $KNiF_3$

The powder susceptibility measurement of $KNiF_3$ by Hirakawa et al. (1960) is the only existing data, Fig.(1-4). They obtained a peak susceptibility of 1.32×10^{-5} emu/g. In the paramagnetic region the susceptibility results obeyed the Curie-Weiss law above 400K with θ=840K and p=4.39 (p is the effective Bohr magneton number). They thought that the observed θ and p were unusually large compared with T_{max}=275K and $p=2\sqrt{S(S+1)}=2.82$ for free spin value of Ni^{2+}. In order to interpret this they tentatively subtracted a temperature independent susceptibility $\chi_c=3.5 \times 10^{-6}$ emu/g from the observed paramagnetic susceptibilities and obtained the

corrected values of θ and p as 300K and 2.80, respectively. They suggested that χ_c could be due to the Van Vleck paramagnetism plus a small part of diamagnetism due to the constituent nonmagnetic ion cores.

In the case of $KNiF_3$, having S=1, spin-wave theory predicts a 13% reduction in $\chi_\perp(0)$, de Jongh and Miedema (1974). One may put $\chi_p(0)=\frac{2}{3}\chi_\perp(0)+\chi_{vv}$ and calculate the experimental $\chi_\perp(0)$ from the measured $\chi_p(0)=9\times10^{-6}$emu/g, Fig.(1-4), and the temperature independent Van Vleck term $\chi_{vv}=2.4\times10^{-6}$ as determined by Lines (1967). The results $\chi_\perp(0)=9.9\times10^{-6}$emu/g may be compared with the value for $\chi_\perp(0)=11.1\times10^{-6}$emu/g calculated with g=2.25 and J/k=44K. The apparent reduction is approximately 15%, in reasonable agreement with expectation, considering the uncertainties involved.

Several as-grown single crystals of $KNiF_3$ with cubic shape of about 3mm on edge were selected for susceptibility measurements. These measurements were kindly performed by Dr. D. Reed at Leeds University. The field was applied along a [100] direction which is one of the antiferromagnetic axes of the crystal. The measurements show that in the region of 6-10 KOe the susceptibility starts to rise gradually. The powder susceptibility measurements of Hirakawa et al. did not show any field dependence. The field dependence in the present work is due to the domain effects existing in the unstrained single crystal. The mechanism responsible for this gradual change in the susceptibility is the domain wall motion. The susceptibility in domains oriented parallel to the field is negligible and the ob-

served macroscopic susceptibility arises solely from the fraction of domains oriented perpendicular to the field. As the field is increased the spins parallel to the field direction will rotate via domain wall motion to the perpendicular direction and the macroscopic susceptibility gradually increases. Above the critical field the domains with spins perpendicular to the field direction are favoured. Accordingly, for fields exceeding this value, measurements in any direction will yield the perpendicular susceptibility, since with the field parallel to the easy axis the moments will have swung to the perpendicular orientation. This is the classic behaviour of a model Heisenberg system. The mechanism differs markedly from the catastrophic spin flop in uniaxial antiferromagnets. In the case of catastrophic spin flop, in a finite interval of field near H_f, the antiferromagnetic vector $\underline{I}=\underline{M}_A-\underline{M}_B$ turns from the direction of the easy axis (Antiferromagnetic state) to that perpendicular to it. Since the spins tilt slightly towards the field direction, a net magnetization $\underline{M}=\underline{M}_A+M_B$ will result. Therefore at a critical field H_f a sudden increase in magnetization occurs. On the contrary, the measurements of magnetization in $KNiF_3$ reveal that in an increasing field a gradual change in the magnetization takes place, and the slope of the magnetization curve changes in the region of 6 KOe, Fig.(8-9). In other words a sublattice magnetization perpendicular to $\underline{H}$, is achieved with a field around 6 KOe. Both direct observations of domain wall motion and the susceptibility measurements in the present work confirm that there is no doubt that spin flop in cubic

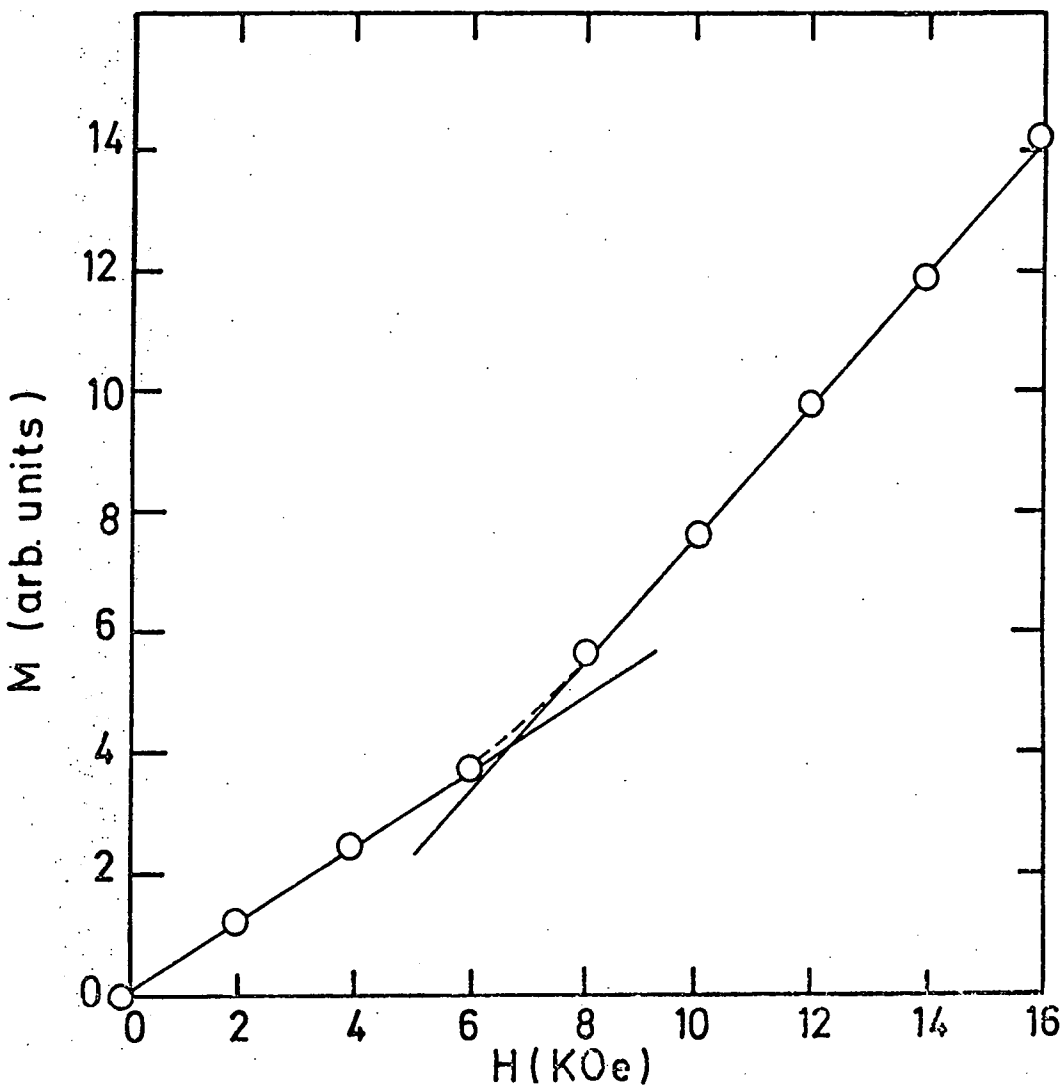

Fig.(8-9) Field dependence of the field induced magnetization in $KNiF_3$ single crystal at 60K. (Susceptibility is given by the slope of the graph).

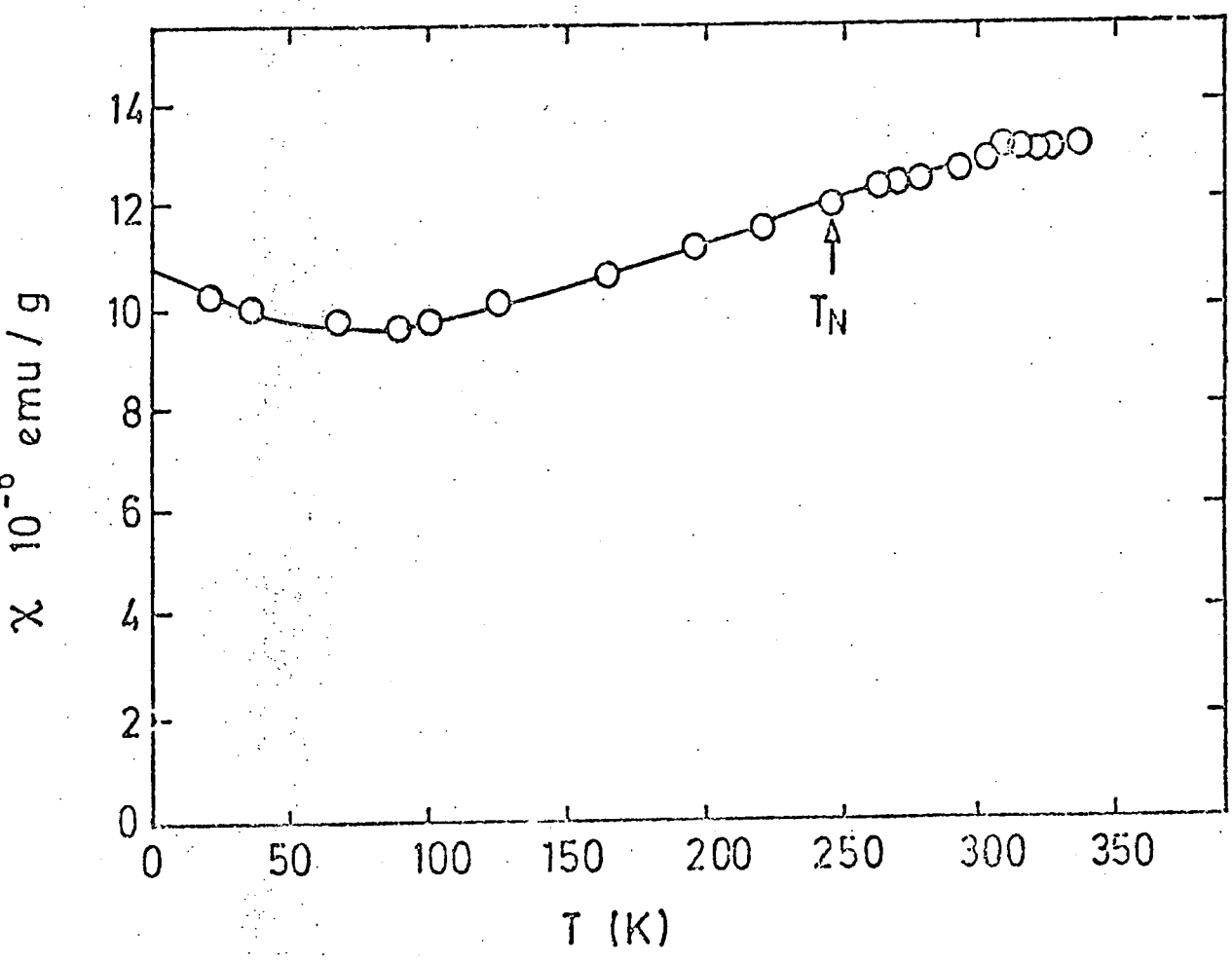

Fig.(8-10) The preliminary susceptibility data from a single crystal of $KNiF_3$ as a function of temperature at 16 KOe.

antiferromagnets occurs via domain wall motion.

Crystals used for susceptibility measurements were about 3mm thick, and due to the high X-ray absorption, X-ray topographic assessment was not possible. Although the crystals will be of comparable perfection to those illustrated in Chapter Four, they will contain more defects due to the larger volume of material. Domain walls could easily be pinned by the imperfections and hence compared with the direct observations of domain wall movements in highly perfect thin slices, higher critical fields are expected.

Preliminary susceptibility measurements (Fig.8-10) as a function of temperature in fields of 16 KOe yield an extrapolated value of $\chi_{\perp}(0)=10.7\times10^{-6}$emu/g. This is in good agreement with Lines (1967) theoretical value of $\chi_{\perp}(0)=11.1\times10^{-6}$emu/g.

8.6 Effective Anisotropy of $KNiF_3$ and $KCoF_3$ crystals

Equation (7-25) which relates CL to the critical and threshold fields was derived on the basis of Néel's ideas and can be written as:

$$CL = \frac{1}{2}(H_{cr}^2 - H_{th}^2)(\chi_{\perp} - \chi_{||}) \qquad (8\text{-}3)$$

H_{cr} and H_{th} were measured in the experiments on domain wall motion in different cooling runs, and their values for $KNiF_3$ and $KCoF_3$ are shown in Table (8-1) and (8-2) respectively.

At low temperatures $\chi_{||}$ is very small compared with $\chi_{\perp}$. Thus $\chi_{||}$ can be neglected at low temperatures. The value

of $\chi_\perp$ for $KNiF_3$ can be obtained from the susceptibility measurements in the present work, Fig.(8-10). Unfortunately there is only a powder susceptibility measurement available for $KCoF_3$, Fig.(1-5). For a simple Heisenberg antiferromagnet at T=0, $\chi_{||}=0$ and also $\chi_\perp=\chi_p(T=T_N)$. Although the actual value of $\chi_\perp$ at low temperatures will be less than that predicted by this simple model, it is a reasonable approximation to assume $\chi_\perp-\chi_{||}=\chi_\perp=\chi_p(T=T_N)$.

Substituting the appropriate values of susceptibilities, H_{th} and H_{cr} into equation (8-3), values of CL for $KNiF_3$ and $KCoF_3$ can be obtained. Table (8-1) shows the values of CL for $KNiF_3$ resulting from domain wall motion studies in a number of cooling runs. All these experiments were performed on one highly perfect crystal slice.

TABLE (8-1)

Cooling runs	Field direction	T(K)	H_{th}(KOe)	H_{cr}(KOe)	CL(erg/cm^3)
A, Fig.(8-2)	[010]	100	1 ± 0.2	4 ± 0.5	$(3.1\pm0.9)10^2$
B, Fig.(8-3)	[010]	4.2	2.2 ± 0.2	4.5 ± 0.5	$(3.2\pm1.1)10^2$
B, Fig.(8-4)	[011]	4.2	3.2 ± 0.5	6.5 ± 0.5	$(3.4\pm1)10^2$
C, not shown	[011]	100	4 ± 0.5	7 ± 0.5	$(3.5\pm1.2)10^2$
D, not shown	[010]	100	1.5 ± 0.2	4 ± 0.5	$(2.9\pm1)10^2$
E, not shown	[010]	4.2	1.2 ± 0.2	2.8 ± 0.2	$(1.3\pm0.3)10^2$

The values of H_{th}, H_{cr} and CL (the effective anisotropy) for a $KNiF_3$ crystal.

Note that the relation (8-3) for CL was obtained for the case of the [010] oriented fields. For the [011] oriented field experiments, according to relations (8-1) and (8-2) the effective magnitudes of the critical and threshold fields have been used for the calculation of CL.

As the topographic experiments were performed in increasing steps of fields, one could not measure the accurate values for H_{cr} and H_{th}. However, by careful inspection of a series of micrographs the range of fields in which domain wall movement started (H_{th}) and the range in which domain walls disappeared, (H_{cr}) were measured, Tables (8-1) and (8-2). Using a fluorescent screen and an image intensifier a direct X-ray topographic image may be obtained which can be viewed via a closed circuit television system, Lang and Reifsnider (1969). Using a fluorescent screen and a very sensitive TV camera, (but no image intensifier) direct viewing was attempted in order to see the dynamical wall motion and hence enable more accurate measurements of H_{cr} and H_{th} to be made. Unfortunately, due to the poor resolution and high noise level obtained, dynamic topographic observations were not successful.

Domain configurations in successive coolings were not reproducible. As seen in Table (8-1) the values of CL for different domain configurations were more or less the same, except in experiment E, where there is a marked difference. In experiment E only half of the crystal was imaged on the photographic emulsion, it can not be determined whether or not all the domain walls had disappeared from the whole

crystal in the measured critical field. Indirect spectroscopic studies of Petit et al. (1975) also showed that the critical field depends on the crystal shape and its thickness and varies from 8 to 22 KOe for their samples (0.2 to 14 mm).

The mechanism involved in the spectroscopic studies of Petit et al. and Ferre' et al. is the same as in the present work, i.e. domain wall motion. However they reported higher values for H_{cr}, and gave a value of $10^3 erg/cm^3$ for CL which is higher than the values obtained by direct measurements, Table (8-1). In order to follow the domain wall motion and measure the correct values of H_{cr} and H_{th} in $KNiF_3$, very highly perfect crystals are needed. Topographic observations of domain wall movements in the crystals containing imperfections such as strong growth bands revealed that the walls could easily be pinned by the imperfections. The quality of the crystals used by Petit et al. have been assessed by X-ray topography (Baruchel, private communication) and are of much lower perfection than our crystals. The imperfections in their crystals will pin the domain walls and hence higher values for the critical field are expected.

The values of H_{cr}, H_{th}, and CL for $KCoF_3$ in different cooling runs are shown in Table (8-2).

TABLE (8-2)

Cooling runs	Field direction	T(K)	H_{th}(KOe)	H_{cr}(KOe)	CL(erg/cm^3)
A, Fig.(8-5)	[010]	77	3 ± 0.2	16.5 ± 0.5	$(2.9\pm0.2)10^4$
B, not shown	[010]	77	5 ± 0.5	16 ± 0.5	$(2.5\pm0.2)10^4$

The values of H_{th}, H_{cr} and CL for a $KCoF_3$ crystal.

Moch and Dugautier (1973) observed a one magnon line centred at 4.5 cm^{-1} or 45 KOe in the Raman spectra of $KNiF_3$. They suggested that at this field spin flop occurs, and deduced the anisotropy value of $K \simeq 10^5 erg/cm^3$. Indirect spectroscopic experiments of Pisarev et al.(1972, 1974) and Ferré et al.(1973) showed that spin flop occurs via domain wall motion at a critical field of 7 KOe. After such a transition they did not observe any other change in the shape of the magnetic circular dichroism spectra of $KNiF_3$ up to 48 KOe. Therefore the mechanism involved in the experiment of Moch and Dugautier differs from the domain wall motion.

8.7 Discussion

$KNiF_3$ and $RbMnF_3$ are most certainly the best approximations of the nearest neighbour only Heisenberg model known at present. Below 82K $RbMnF_3$ becomes antiferromagnetic with spins alternating along cubic edges. From X-ray studies Teaney et al.(1966) concluded that departures from cubic symmetry larger than a few parts in 10^5 were not present. Windsor and Stevenson (1966) found no detectable next nearest-neighbour interactions, and determined the nearest neighbour exchange as $J/k = -3.4 \pm 0.3$K. The anisotropy of $RbMnF_3$ has been measured and is a minute $H_A/H_E \simeq 5 \times 10^{-6}$! Due to the small value of the anisotropy above 3 KOe the susceptibility was found to be isotropic, De Jongh and Miedema (1974). For fields higher than this value the spins originally parallel to the field direction will have rotated to the perpendicular orientation, and susceptibility measurements in any direction will produce the perpendicular susceptibility. This behaviour is similar to the present susceptibility measurements of $KNiF_3$.

Classical X-ray studies of $KNiF_3$ below T_N revealed no distortion from the cubic perovskite structure, Fig.(1-6). However from the contrast of domain walls on X-ray topographs it was concluded that there is a small tetragonal distortion $10^{-5} \lesssim \frac{c-a}{a} \lesssim 10^{-4}$. As a consequence of such high cubic symmetry of the magnetic lattice, the contribution of magnetic dipole-dipole interactions to the anisotropy in $KNiF_3$ is expected to be negligible. The evidence of low anisotropy in $RbMnF_3$ supports this point.

Unlike $KNiF_3$, the unit cell of $KCoF_3$ crystal undergoes a considerable distortion ($\frac{c-a}{a} \simeq 3.5 \times 10^{-3}$ at 4.2K), Fig.(1-7). Due to this departure from the cubic symmetry the dipole-dipole interactions contribute to the anisotropy energy of the $KCoF_3$ system. The orbital angular momentum of the Co^{+2} ion is not quenched by the octahedrally co-ordinated crystal field, Buyers et al.(1971), and this gives rise to the possibility of anisotropic magnetic interactions between the ions. Therefore the value of the anisotropy energy in $KCoF_3$ is expected to be higher than in $KNiF_3$.

The values of CL for $KNiF_3$ and $KCoF_3$ were deduced from the data of domain wall studies. Tables (8-1) and (8-2) show that the value of CL in $KCoF_3$ is two orders of magnitude higher than in $KNiF_3$. Although the relation between CL and the magnetocrystalline anisotropy is not clear, a higher value of magnetocrystalline anisotropy is expected for $KCoF_3$ compared to $KNiF_3$.

The stress induced linear dichroism experiments of Ferré et al. (1976) suggest the spin flop in $RbMnF_3$ occurs

via domain wall motion. In $RbMnF_3$ the antiferromagnetic resonance and susceptibility data (Teaney and Freiser, 1962) and the spectroscopic data are consistent. However, for $KNiF_3$ the antiferromagnetic resonance data (Curatella et al., 1976) and one magnon Raman data (Moch and Dugautier, 1973) are not consistent with the spectroscopic data of Ferré et al.(1976) and Petit et al.(1975), and the present experiments on domain wall motion and susceptibility. This discrepancy for $KNiF_3$ remains a puzzle.

SUGGESTIONS FOR FURTHER EXPERIMENTS

The availability of synchrotron radiation and the relaxation of the geometrical limitations on X-ray topography enables many new experiments to be performed. For example, experiments involving the application of an external stress to crystals at liquid nitrogen temperatures becomes hardly more difficult to perform than the equivalent experiment at room temperature. The whole straining jig can be immersed in liquid nitrogen in an expanded polystyrene trough, then by applying stress, direct observation of domain wall motion in $KNiF_3$ and $KCoF_3$ could be performed. This kind of experiment is strongly recommended.

The magnetostrictive distortion of $KCoF_3$ is known accurately. Therefore by measuring the critical stress and using the present critical field data on $KCoF_3$, one can test the theory which relates σ_{cr}, H_{cr} and λ_{100}, (equation 7-31). Furthermore attempts could be made to measure the critical stress in $KNiF_3$ by direct topographic studies. Relating the critical stress to the present data on critical field, one can estimate the magnetostriction constant for $KNiF_3$. High precision measurements of the magnetostrictive distortion of $KNiF_3$ by double crystal diffractometer should also be performed and compared with the estimate obtained from domain studies.

Similar domain wall motion studies on highly perfect $RbMnF_3$ crystals, (another good Heisenberg system) should be performed. This kind of experiment can determine the

value of the effective anisotropy CL. Then by comparing the value of CL with the reported value of the magneto-crystalline anisotropy in $RbMnF_3$, a clue origin of CL in cubic antiferromagnets might be obtained.

Theoretically, attempts should be made to investigate the origin of the restoring force resisting domain wall motion. Also more theoretical work on the configuration of the spins inside an antiferromagnetic domain wall could provide better understanding of the energy and thickness of the wall.

APPENDIX

The structure factor F(hkl) is defined by

$$F(hkl)=\sum_j f_j \exp 2\pi i(hu_j+kv_j+lw_j) \qquad \text{A-1}$$

u,v,w being the fractional coordinates of the centre of the atom whose scattering factor is f times that of a single classical electron, the summation being taken over all the atoms in the unit cell.

KMF_3 crystals are of the perovskite structure, Fig.(1-3). Each divalent metal M^{2+} is surrounded octahedrally by six F^- ions at face-centres, while at each cube corner there is a K^+ ion. Taking one of the atoms M as origin, in each unit cell the co-ordinates of K, F and M are:

M: 000

F: $00\frac{1}{2}$, $\frac{1}{2}00$, $0\frac{1}{2}0$

K: $\frac{1}{2}\frac{1}{2}\frac{1}{2}$

Using the equivalent point coordinates for each kind of atom, the relation A-1 can be written as:

$$F(hkl)=f_M+f_K\exp[-i\pi(h+k+l)]+f_F[\exp(-i\pi h)+\exp(-i\pi k)+\exp(-i\pi l)] \qquad \text{A-2}$$

The scattering powers f_M, f_K and f_F were obtained from the International Tables for X-ray crystallography (1962)

The X-ray extinction distance ξ_g is related to the structure factor F_g

$$\xi_g = \frac{V_c \cos\theta_B}{C r_e \lambda (F_g F_{\bar{g}})^{\frac{1}{2}}} \qquad \text{A-3}$$

where V_c is the volume of the unit cell, r_e the classical electron radius. C=1 or $\cos 2\theta_B$ for σ and π polarizations respectively.

The values of F(hkl) and ξ_g for different reflections were calculated for $KNiF_3$ and $KCoF_3$ and are shown in Tables A-1 and A-2. Here the temperature dependence of the structure factor is not included.

TABLE A-1

Reflection	F	$MoK\alpha_1, \lambda = 0.7107 Å$		$A_gK\alpha_1, \lambda = 0.5608 Å$	
		θ_B^o	ξ (μm)	θ_B^o	ξ (μm)
100	17.6	5.07	58	4	73.2
200	51	10.18	20.3	8.03	25.5
300	3.3	15.37	322	12.1	399.5
400	29.4	20.69	37.8	15.64	45.7
110	29.7	7.2	34.6	5.67	43.5
220	40.3	14.27	26.2	11.4	32.6
111	11	8.8	93.2	6.95	117

Structure factors and extinction distances of $KNiF_3$ crystal for different reflections.

TABLE A-2

Reflection	F	$MoK\alpha_1, \lambda=0.7107\text{Å}$		$AgK\alpha_1, \lambda=0.5608\text{Å}$	
		θ_B^o	$\xi(\mu m)$	θ_B^o	$\xi(\mu m)$
100	15.7	5.01	67.5	3.95	85.95
200	48.5	10.06	22.1	7.92	27.8
300	2	15.2	550	11.9	685
400	29	20.5	39.6	16	48.3
110	28.9	7.2	37.4	5.67	46.5
220	39.4	14.3	27.8	11.24	34.7

Structure factors and extinction distances of $KCoF_3$ crystal for different reflections.

REFERENCES

(1) Aldred, P.J.E. and Hart, M. Proc.Roy.Soc. (1973) A332, 223.

(2) Anderson, P.W. Phys.Rev. (1950) 79, 350.

(3) Ando, M. and Hosoya, S. Phys.Rev.Lett. (1972) 29,281.

(4) Armstrong, R.W. and Wu, C.Cm. In Microstructural Analysis, Tools and Techniques (ed. McCall and Muller), (Plenum), (1975), P.169.

(5) Austermann, S.B. and Newkirk, J.B. Adv. X-ray Analysis (Plenum), (1967) 10, 134.

(6) Authier, A. Bull.Soc. France Minér. Crist. (1961) 84, 51.

(7) Authier, A. Adv. in X-ray Analysis, (Plenum), (1967) 9, P.9.

(8) Authier, A. "Modern Diffraction and Imaging Techniques in Materials Science" ed. S. Amelinckx et al. (N. Holland), (1970) P.481.

(9) Balchin, A.A. and Whitehouse, C.R. Phys.Education (1974) 9, 53.

(10) Barrett,C.S. Trans. AIME (1945) 161, 15.

(11) Batterman, B.W. and Cole, H. Rev.Mod.Phys.(1964) 36,681.

(12) Baruchel, J. Private Communication (1973).

(13) Berg, W.F. Naturwissenschaften (1931) 19, 391.

(14) Bitter, F., Phys.Rev. (1937) 54, 79.

(15) Bizette, H., Squire, C. and Tsai, B. Comptes Rendus (1938) 207, 449.

(16) Bond, W.L. and Andrus, J., Amer. Mineralogist (1952) 37, 622.

(17) Bonse, U., Z.Phys. (1965) 184, 71.

(18) Bonse, U., Hart, M. and Newkirk, J.B., Adv. X-ray Analysis (Plenum), 1967) 10, 1.

(19) Bonse, U. and Kappler, E., Z. Naturforsch. (1958) 13a, 348.

(20) Bordas, J., Glazer, A.M. and Hauser, H. Phil.Mag. (1975) 32, 471.

(21) Breed, D.J., Gilijamse, K. and Miedema, A.R. Physica (1969) 45, 205.

(22) Buyers, W.J.L., Holden, T.M., Svensson, E.C., Cowley, R.A. and Hutchings, M.T., J.Phys. (1971) C4, 2139.

(23) Chinn, S.R., Zeiger, H.J. and O'Connor, J.R., Phys. Rev.B. (1971) 3, 1709.

(24) Curatella, S., Causa, M.T., and Misetich, A., J.Magnetism and Magnetic Materials (1976) 1, 317.

(25) De Jongh, L.J. and Miedema, A.R., Advances in Phys. (1974) 23, 1-260.

(26) De Jongh, L.J., and Block, R. Physica (1975) 79B, 568.

(27) Dirac, P.A.M., Proc.Roy.Soc. (London), (1929) A123, 714.

(28) Epelboin, Y., Zarka, A. and Klapper, H., J. Crystal Growth (1973) 20, 103.

(29) Ewald, P.P., Ann.Phys. (1916) 49, 38, 117.

(30) Ewald, P.P., Ann.Phys. (1917) 54, 519.

(31) Ferré, J., Briat, B., Petit, R.H., Pisarev, R.V., and Nouet, J., J.de Phys.(1976) 37, 503.

(32) Ferré, J., Briat, B., Pisarev, R.V. and Nouet, J., Proc.Int.Conf.Magn.(Moscow 1973), (1974) 2, 117.

(33) Fisher, M.E., Physica (1962) 28, 919.

(34) Fishman, Yu.M. and Lutsau, V.G., Phys.Stat.Sol.(a) (1970) 3, 828.

(35) Foner, S. and Hou, S.L., J.Appl.Phys., (1962) 33, 1289.

(36) Freiser, M.J., Seiden, P.E. and Teaney, D.T., Phys. Rev.Lett. (1963) 10, 293.

(37) Garrard, B.J., Wanklyn, B.M. and Smith, S.H., J.Crystal Growth, (1974) 22, 169.

(38) Garrard, B.J., Smith, S.H., Wanklyn, B.M. and Garton, G., J.Crystal Growth, (1975) 29, 301.

(39) Guinier, A. and Tennevin, J., Acta Cryst.(1949) 2, 133.

(40) Hart, M., J.Appl.Cryst. (1975) 8, 436.

(41) Hirakawa, K., Hirakawa, K., and Hashimoto, T., J.Phys.Soc.Jap.(1960) 15, 2063.

(42) Hirakawa, K., Hashimoto,T. and Hirakawa,K., J.Phys. Soc.Jap. (1961) 16, 1934.

(43) Holden, T.M., Buyers, W.J.L., Svensson, E.C., Cowley, R.A., Hutchings, M.T., Hukin, D. and Stevenson, R.W.H., J.Phys.(1971) C.4, 2127.

(44) Hosoya, S. and Ando, M.Phys.Rev.Lett.(1971) 26, 321.

(45) Isherwood, B.J. and Wallace, C.A., Phys.in Technology, (1974) 5, 244.

(46) Jacobs, I.S., J.Appl.Phys. (1961) 32, 61S.

(47) Julliard, J., and Nouet, J., Rev.de Phys.Appl.(1975) 10, 325.

(48) Kato, N., Acta.Cryst.(1961) 14, 526, 627.

(49) Kato, N., Acta.Cryst.(1969) A25, 119.

(50) Kato, N., and Lang, A.R., Acta.Cryst.(1959) 12, 787.

(51) King, A.R., and Paquette, D., Phys.Rev.Lett. (1973) 30, 662.

(52) Kittel, C. "Introduction to Solid State Physics", (1971).

(53) Klapper, H., J.Crystal Growth (1972) 15, 281.

(54) Klapper, H., Phys.Stat.Sol.(a), (1972) 14, 99.

(55) Klapper, H., Phys.Stat.Sol.(a), (1972) 14, 443.

(56) Klapper, H., Z. Naturforschung (1973) 28a, 614.

(57) Klapper, H., and Küppers, H., Acta.Cryst.(1973) A29,495.

(58) Klapper, H., and Küppers, H., Acta.Cryst.(1974) A30,302.

(59) Kohler, W.C., Wilkinson, M.K., Cable, J.W., Wollan,E.O. J.de Phys.Radium (1959) 20, 180.

(60) Kramers, H., Physica (1934) 1, 182.

(61) Kranjc, K., J.Appl.Cryst. (1969) 2, 262.

(62) Lang, A.R., J.Appl.Phys. (1958) 29, 597.

(63) Lang, A.R., Acta.Cryst. (1959) 12, 249.

(64) Lang, A.R., Brit.J.Appl.Phys. (1963) 14, 904.

(65) Lang, A.R., "Modern Diffraction and Imaging Techniques in Materials Science", ed. S. Amelinckx et al. (N.Holland, 1970) P. 407.

(66) Lang, A.R. and Reifsnider, K., Appl.Phys.Lett.(1969) 15, 258.

(67) Laue, M.v.,Ergeb.der exact Naturwiss (1931) 10,133.

(68) Lines, M.E., Phys.Rev. (1967) 164, 736.

(69) Mathiot, A., Petroff, J.F., and Barnard, Y. Phys. Stat.Sol.(a), (1973) 20, K1.

(70) Mathiot, A., Petroff, J.F., A.I.P. Conf.Proc.(1975) 13, 757.

(71) Merz, K.M., J.Appl.Phys. (1960) 31, 147.

(72) Moch, P. and Dugautier, C.Proc.Int.Conf.Magn.(Moscow, 1973), (1974) 1, 185.

(73) Morrish, A.H., "The Physical Principles of Magnetism". (1965) P.481.

(74) Nagamiya, T., Prog. Theor.Phys. (1951) 6, 342.

(75) Nagamiya, T., Proc.R.A. Welch Foundation Conference on Chem.Res.(Houston, Texas, 1958) p.109.

(76) Nagamiya, T., Yosida, K., and Kubo, R. Adv. in Phys., (1955) 4, 1.

(77) Nakahigashi, K., Fukuoka, N., and Shimomora, Y., J.Phys.Soc.Jap.(1975) 38, 1634.

(78) Néel, L., Ann.de Phys.(1932), 17, 64.

(79) Néel, L., Ann.de Phys.(1936), 5, 232.

(80) Néel, L., Comptes Rendus (1936) 203, 304.

(81) Néel, L., Proc. of the Kyoto Conf. on Theoretical Physics, 1953 (Science Council of Japan, Tokyo 1954) P.701.

(82) Nouet, J., Ph.D. Thesis, Paris (1973).

(83) Nouet, J., Zarembovitch, A., Pisarev, R.V., Ferré, J., and Lecomte, M., Appl.Phys.Lett.(1972) 21, 161.

(84) Okazaki, A., Suemune, Y., Fuchikemi, T., J.Phys.Soc. Jap.(1959) 14, 1823.

(85) Okazaki, A. and Suemune, Y., J.Phys.Soc.Jap.(1961) 16, 671.

(86) Okazaki, A. and Kawaminami, M. Jap.J.Appl.Phys.(1973) 12, 783.

(87) Parkes, K.G., Ph.D. Thesis (Sheffield University, 1971).

(88) Parpia, D.Y., Phil.Mag.(1976) 33, 713.

(89) Petit, R.H., Ferré, J., and Nouet, J., J.de Phys.(1975) 36, 431.

(90) Petroff, J.F. and Mathiot, A., Mater.Res.Bull.(1974) 9, 319.

(91) Pisarev, R.V., Ferré, J., Duran, J. and Badoz, J., Solid State Communications (1972) 11, 913.

(92) Pisarev, R.V., Ferré, J., Petit, R.H., Krichevtsov, B.B., and Syrnikov, P.P., J.Phys.(1974) C.7, 4143.

(93) Polcarova, M., Trans.IEEE Magnetic MAG(1969) 5, 536.

(94) Polcarova, M., Z. Naturforschung (1973) 28a, 639.

(95) Polcarova, M., and Gemperlova, J., Phys.Stat.Sol. (1969) 32, 769.

(96) Polcarova, M. and Kaczer, J., Phys.Stat.Sol. (1967) 21, 635.

(97) Polcarova, M. and Lang, A.R., Appl.Phys.Lett.(1962), 1, 13.

(98) Polcarova, M., and Lang, A.R., Bull.Soc. Franc.Minér. Crist.(1968) 91, 645.

(99) Poole, J.H., Daresbury Laboratory Preprint, (1975), DL/SRF/TM1.

(100) Poulis, N.J., Van Den Handel, J., Ubbink, J., Poulis, J.A. and Gorter, C.J., Phys.Rev.(1951) 82, 552.

(101) Roth, W.L., J.Appl.Phys.(1960) 31, 2000.

(102) Rousseau, M., Nouet, J., and Zarembowitch, A., J.Phys.Chem.Solid (1974) 35, 921.

(103) Rushbrook, G.S., and Wood, P.J., Mol.Phys.(1958) 1, 275.

(104) Rushbrook, G.S., and Wood, P.J., Mol.Phys.(1963) 6, 409.

(105) Safa, M., Midgley, D., and Tanner, B.K., Phys.Stat. Sol.(a), (1975) 28, K89.

(106) Safa, M. and Tanner, B.K., Proc.Internat.Conf. Magnetism, (Amsterdam 1976), Physica (1977) 86-88B, 1347.

(107) Safa, M., Tanner, B.K., Klapper, H. and Wanklyn, B.M. Phil.Mag. In Press.

(108) Safa, M., Tanner, B.K., Garrard, B.J., and Wanklyn, B.M., J. Crystal Growth, In Press.

(109) Saito, S., Nakahigashi, K. and Shimomura, Y., J. Phys.Soc.Jap.(1966) 21, 850.

(110) Scatturin, V., Corliss, L., Elliot, N., and Hastings, J., Acta.Cryst.(1961) 14, 19.

(111) Schlenker, M., Baruchel, J., and Nouet, J.,Proc. Internat.Conf.Magnetism, Moscow (1974) P.368.

(112) Schulz, L.G., J.Metals (1954) 6, 1082.

(113) Shull, C.G., Strauser, W.A., and Wollan, E.O., Phys. Rev. (1951) 83, 333.

(114) Sintani, K., Tomono, Y., Tsuchida, A., and Siratori, K., J.Phys.Soc.Jap.(1968) 25, 99.

(115) Slack, G.A., J.Appl.Phys. (1960) 31, 1571.

(116) Sykes, M.F., and Fisher, M.E., Phil.Mag.(1962) 7,1731.

(117) Tanner, B.K., "X-ray Diffraction Topography", (Pergamon Press, 1976).

(118) Tanner, B.K., Safa, M., Midgley, D. and Bordas, J., J.Magnetism and Magnetic Materials (1976) 1, 337.

(119) Tanner, B.K., Safa, M., Midgley, D., J.Appl.Cryst., In Press.

(120) Tanner, B.K., Midgley, D., Safa, M., J.Appl.Cryst., In Press.

(121) Teaney, D.T. and Marvin, J.F., Phys.Rev.Lett.(1962) 1, 212.

(121) Teaney, D.T., Moruzzi, V.L., Argyle, B.E., J.Appl. Phys., (1966) 37, 1122.

(122) Tuomi, T., Naukkarinen, K. and Rabe, P., Phys.Stat. Sol.(a), (1974) 25, 93.

(123) Uchida, E., Kondoh, H., Nakazumi, Y., Nagamiya, T., J.Phys.Soc.Jap.(1960) 15, 466.

(124) Van Vleck, J.H., Phys.Rev. (1937) 52, 1178.

(125) Van Vleck, J.H., J.Chem.Phys. (1941) 9, 85.

(126) Wanklyn, B.M., J.Crystal Growth (1969) 5, 279.

(127) Wanklyn, B.M., J.Mat.Science (1975) 10, 1487.

(128) Wilkinson, M.K., Cable, J.W., Wollan, E.O., and Kohler, W.C., Phys.Rev. (1959) 113,497.

(129) Windsor, C.G., and Stevenson, R.W.H., Proc.Phys.Soc. London, (1966) 87, 501.

(130) Yamada, T., J.Phys.Soc.Jap.(1963) 18, 520.

(131) Yamada, T., J.Phys.Soc.Jap.(1966) 21, 650.

(132) Yamada, T., Saito, S., and Shimomura, Y., J.Phys. Soc.Jap. (1966) 21, 672.

(133) Yosida, K., Prog.Theor.Phys. (1951) 6, 691.